

Modelling the Electromagnetic Properties of Conductive Nonwoven Fabrics

Andrew Nicholas Austin
Doctor of Philosophy
University of York
Electronics
February 2017

To my family for their constant support and encouragement.

To my warm hearted friends for their comity.

To perseverance and hard work.

Abstract

This thesis presents micro-structure models of wet-laid conductive nonwoven fabrics allowing the sheet conductance and shielding effectiveness to be simulated and compared to experimental measurement. Conductive nonwoven fabrics are used within the aerospace and defence industries to provide lightweight, functional electromagnetic enhancement to composite structures. They are materials borne from stochastic processes with anisotropic distributions of fibre and parameters that vary from point to point on the local scale.

Monte Carlo models of the material's micro-structure have been constructed by writing a series of algorithms which pseudo-randomly generate the material's structure by incorporating key physical parameters such as the density, areal concentration and fibre angle distribution. To define the last of these parameters, a completely new optical method has been developed making use of the Hough Transform. These models have predicted the anisotropic sheet conductance to within 1-2% of experimental values, with an estimated inter-fibre contact resistance of $R_j = 8.6k\Omega$, and a measured geometry factor of $\Phi_x = 0.727$, $\Phi_y = 0.273$. Analytic models of the material are derived from first principles enabling the rapid calculation of the sheet conductance, whilst also providing an understanding between the key parametric relationships. The analytic model, Monte Carlo model and experimental measurements are compared and give good correspondence.

The micro-structure models are finally applied to a full wave electromagnetic simulation technique and shown to produce close correlation to polarisation specific measurements of the shielding effectiveness. High frequency (up to 200GHz) simulations of lightweight nonwoven structures suggest an eventual fall in the shielding effectiveness, attributed to the material's sub-wavelength apertures.

Contents

Abstract	5
Contents	7
List of figures	11
List of tables	17
Acknowledgements	19
Declaration	21
1 Introduction	23
1.1 Overview and Industrial Context	24
1.2 Motivation and Scope	26
1.3 Original Contributions	27
1.4 Outline of the Thesis	28
2 Shielding Theory and Modelling Techniques	31
2.1 Overview	32
2.2 Electromagnetic Wave Theory	33
2.2.1 Propagation in Free Space	33
2.2.2 Near and Far Fields	35
2.2.3 Propagation in Media	36
2.3 Shielding Effectiveness Theory	38
2.3.1 Schelkunoff's Shielding Theory	38
2.3.2 Kaden's Shielding of Enclosures	44
2.4 Reflection and Transmission of EM Waves	48
2.4.1 Single Interface (normal incidence)	48
2.4.2 Single Interface (oblique incidence)	50

Contents

2.4.3	Multiple Interface (normal incidence)	55
2.4.4	Multiple Interface (oblique incidence)	57
2.4.5	Wave Diffraction Through Apertures	58
2.4.6	Polarizability: Sub-wavelength aperture theory	60
2.4.7	Transfer Impedance	62
2.5	Aperture Modelling Techniques	66
2.5.1	Analytic Models of Apertures (Perforated Brass Sheet) . .	66
2.5.2	TLM models of Apertures (Perforated Brass Sheet)	69
2.5.3	Comparison of Aperture Models	74
2.6	Summary	75
3	Nonwoven Materials	77
3.1	Overview	78
3.2	Wet-laid Nonwoven Fabrics	78
3.2.1	Background	78
3.2.2	The Manufacturing Process	80
3.3	The Physical Properties of Nonwovens	82
3.3.1	Constituent Properties	82
3.3.2	The Micro-Structure of Nonwoven Sheets	84
3.3.3	Fibre Angle Orientation	84
3.3.4	Apertures	85
3.3.5	Density	87
3.4	Conduction Mechanisms	90
3.4.1	Percolation Theory of Conductor Networks	90
3.4.2	Recent Work	92
3.4.3	Inter-fibre Contact Resistance	93
3.5	Summary	94
4	Experimental Measurements of Nonwoven fabrics	95
4.1	Overview	96
4.2	Quasi-static Electrical Measurements	96
4.2.1	Sheet Conductance Experiments	96
4.2.2	Results	100
4.3	Radio Frequency Measurements	103
4.3.1	Shielding Effectiveness Experiments	103
4.3.2	Setup and Equipment	105
4.3.3	Absorber Box Calibration	107

4.3.4	Error and Variability	108
4.3.5	Shielding Effectiveness Results	109
4.4	Summary	110
5	Modelling Methodology of Nonwoven Fabrics	111
5.1	Overview	112
5.2	Fibre Angle Distribution: Methodology	113
5.2.1	The Hough Transform	114
5.2.2	Image Processing	117
5.2.3	Generation of the Probability Density Function	118
5.2.4	Calculation of the Geometry Factor Φ	120
5.2.5	Geometry Factor Error Analysis	121
5.3	Development of Numerical Models	124
5.3.1	Monte Carlo Modelling	124
5.3.2	Micro-structure Generation	125
5.3.3	Meshing of 3D CAD geometries	127
5.3.4	Equivalent Resistor Networks	128
5.3.5	TLM Modelling of the Shielding Effectiveness	131
5.4	Analytic Formulation of the Sheet Conductance	134
5.4.1	Overall Conductance of a 2D mesh	134
5.4.2	Conductance of a 2D mesh neglecting contact resistance	134
5.4.3	Conductance of a 2D mesh with contact resistance	137
5.4.4	Conductance of a 3D mesh with contact resistance	138
5.5	Summary	141
6	Results and Analysis	143
6.1	Overview	144
6.2	Percolation Threshold Models	145
6.3	Sheet Conductance Models	147
6.3.1	Idealised 2D Case	147
6.3.2	Idealised 3D Case	152
6.3.3	Real Material Models	156
6.4	Shielding Effectiveness Models	160
6.5	Summary	168
7	Conclusions	169
7.1	Summary	170
7.2	Further Work	172

Contents

Appendix A	177
A.1 Maxwell's equations	178
A.2 Resistance Model: Nonwoven Fabric Codes	181
A.3 Planar Metal Shielding (Schelkunoff) Codes	183
A.4 Absorber Box Data Codes	185
A.5 Fibre Angle Distribution Codes	187
A.6 Geometry Factor Codes	190
Nomenclature	191
References	195

List of figures

1.1	The evolution of the composites industry through history and its importance today. Reproduced with permission [3].	25
2.1	An electromagnetic wave propagating in free space [4]	34
2.2	The change in wave impedance as a function of distance based on [5]	35
2.3	The shielding effectiveness of an enclosure	38
2.4	Various thickness of copper and corresponding shielding effectiveness as predicted by the Schelkunoff model	40
2.5	The shielding effectiveness of various materials with 0.01 mm thickness, as predicted by the Schelkunoff model	40
2.6	The skin depth of different materials	42
2.7	The frequency dependency of the relative magnetic permeability for magnetic metals [13]	43
2.8	A typical example of simple shielding enclosure	44
2.9	PC enclosure with necessary cooling apertures, cable holes, window and access door.	46
2.10	An enclosure containing a single large aperture, reproduced with permission from[16]	46
2.11	A slotted enclosure's electric shielding effectiveness and first order resonance occurring at 700 MHz [16].	47
2.12	An electromagnetic wave interaction with a single interface	48
2.13	Oblique wave incidence, perpendicular E-field polarization	50
2.14	Oblique wave incidence, parallel E-field polarization	53
2.15	Reflection and Transmission coefficients used at each material interface	55
2.16	Oblique wave incidence, upon multiple interface	57
2.17	A schematic representing penetration effects of electric and magnetic fields when an aperture is present	59

List of figures

2.18	The field diffracted by a small aperture within a conducting screen is equivalent to the superposition of the normal electric and tangential magnetic fields from a radiating dipole [25]	60
2.19	Coupling mechanisms in cable braids [26]	62
2.20	A wire mesh geometry with wire diameter 'd' and spacing 'a' . . .	64
2.21	Examples of copper wire meshes with a filament diameter 100um at different spacing 'a'	65
2.22	A 0.3mm perforated brass reference sample	66
2.23	An analytic polarizability model of the brass reference plate . . .	68
2.24	The Symmetrical Condensed Node (SCN), derived by Johns is used to propagate field components through a 3D problem space	69
2.25	An array of Symmetrical Condensed Nodes	70
2.26	The time evolution of a 2D TLM model [34]	70
2.27	A 5x5x0.3mm CST model of a the perforated brass sheet shown in 2.22	72
2.28	Energy Propagation through the perforated brass sheet at 3 different time steps: 71, 156, 300.	73
2.29	The time response of port 2, showing the gaussian excitation with a -45dB stopping criterion, demonstrating most of the energy has left the mesh	73
2.30	Analytic, numeric and measured shielding effectiveness values of the perforated plate	74
3.1	Images of carbon fibre nonwoven fabrics	79
3.2	Schematic overview of the nonwoven fabric manufacturing process	80
3.3	Nonwoven fabric (bottom left) entering the oven section, painted blue	81
3.4	An SEM image demonstrating the micro-structural features of carbon fibre based nonwoven fabrics (x250 magnification)	84
3.5	A comparison of two fibre angle orientations possible by changing processing parameters	85
3.6	The average aperture size of carbon nonwoven fabrics versus areal weight using mercury intrusion porosimetry analysis (conducted on an Autopore IV 9500 instrument)	86
3.7	The relationship between carbon nonwoven fabric thickness, density and areal weight	88
3.8	The measured thickness of real nonwoven sheets and a fitted thickness function	89

List of figures

3.9	The onset of the electric percolation threshold is marked by the sharp increase in conductivity of a given system with areal concentration.	90
3.10	Classifications of fibres, clusters and giant clusters which governs percolation dynamics in stick networks	91
3.11	A pictorial representation of percolating and non-percolating stick networks	92
4.1	The Vermason contact block and multi-meter	97
4.2	The Ecopia probe which utilises sprung loaded gold electrodes . .	98
4.3	The Delcom PC873 Eddy Current instrument used to deduce the sheet conductance in a contactless manner	98
4.4	The change in sheet conductance of carbon nonwovens versus areal weight, using four different measurement methods	101
4.5	Strong correlation of sheet conductance between two contactless techniques - SE fit and the Eddy current method	101
4.6	The variability of sheet conductance at different positions across various areal weight carbon nonwoven fabrics	102
4.7	The Absorber Box - a planar material shielding effectiveness measurement system	103
4.8	The configuration of the Absorber Box system	104
4.9	The Agilent Technologies Japan E5071B network analyser	105
4.10	Different views of the Absorber Box system	106
4.11	A photograph of the perforated brass plate sample used to calibrate the Absorber Box	107
4.12	The shielding effectiveness of the perforated brass plate using a variety of measurement and modelling methods, reproduced with permission [67]	108
4.13	The average shielding effectiveness of carbon fibre nonwoven fabrics, plotted with one standard deviation (shaded region)	109
5.1	The modelling framework	112
5.2	Key processes in calculating fibre angle distribution and polarization dependent sheet resistance	113
5.3	The basic fundamentals of the Hough transform function, reproduced with permission [69]	114
5.4	The Hough transform of a nonwoven fabric	115

List of figures

5.5	The image processing and detection of fibres using the Hough transform (each image represents an area of $3.61mm^2$)	116
5.6	Images of the nonwoven micro-structure were captured using a Brunel SP60 light microscope.	117
5.7	PDF's determined from measurements of the fibre angle distribution using the Hough transform method over 50 images (approximately 10,000 fibres)	119
5.8	The impact of Hough threshold H_t on the Geometry Factor Φ . .	122
5.9	Images showing identified fibres at two different Hough threshold values in $10g/m^2$ materials	122
5.10	The impact of histogram bin widths on the Geometry Factor Φ .	123
5.11	The key programming steps used to generate the numerical models	124
5.12	The co-ordinate system used to generate the nonwoven fabric geometry - the sample lies in the XY plane, thickness along the Z plane. X is along the 0° orientation and Y along the 90° orientation	126
5.13	A plan view of the holistic stochastic fibre model, directly generated by the written algorithms. Four samples (red) are shown here. 50 samples were used to generate the data in the later results	126
5.14	The meshed CAD output of the Monte Carlo generated nonwoven fabric structure	127
5.15	An equivalent circuit model of the fibre network	128
5.16	A CAD image portraying the fibres and contact points between fibres	129
5.17	The meshed CAD geometries of simple test cases used to validated the numerical model	130
5.18	Different resolutions of the mesh and its effect on the fibre's thickness	132
5.19	The convergence of finer mesh sizes when modelling a $4g/m^2$ fabric	133
5.20	A conducting fibre path in a material of square dimensions l_s . . .	135
5.21	Comparing the number of contacts per fibre predicted by Heitz for a uniform 2D sheet with 2D MCM sheets with a Gaussian angular PDF and an empirical estimate	138
5.22	Comparing the number of contacts per fibre predicted by Heitz for a uniform 2D sheet with 3D MCM sheets, and an empirical estimate	139
6.1	Relationship between the dimensionless areal concentration and areal weight, particular for 12mm fibres of density $1820 Kg/m^3$.	144
6.2	The percolation probability of a 3D MCM with uniform fibre angle distribution at various thickness	145

List of figures

6.3	The effect of thickness on the percolation threshold	146
6.4	The sheet conductance for a 2D nonwoven fabric with superconducting contacts and a uniform fibre angle distribution.	148
6.5	The mean number of contacts per fibre in a 2D model of the nonwoven fabric.	149
6.6	The sheet conductance for a 2D Uniform fibre angle distribution and $1M\Omega$ contacts	150
6.7	The PDF of a Gaussian fibre angle distribution for $-90 \leq \phi \leq 90$ and $\sigma = 30$	151
6.8	The sheet conductance of a 2D anisotropic sheet ($\Phi_x = 0.8, \Phi_y = 0.2$) with superconducting contacts	151
6.9	The levelling of the mean number of contact points per fibre from $\tilde{n}_A > 150$ in 3D models compared to the Heitz 2D model which remains linear	152
6.10	The sheet conductance for a 3D Uniform fibre angle distribution and superconducting contacts	153
6.11	The levelling off of the sheet conductance for the uniform 3D model with a contact resistance of $1M\Omega$	153
6.12	The sheet conductance behaviour of a 3D case with an anisotropic fibre angle distribution and superconducting contacts	154
6.13	The mean number of contacts per fibre for the 3D case with an anisotropic fibre angle distribution	155
6.14	The measured PDF for the fibre angle distribution of 4 and 10 g/m^2 materials	156
6.15	The measured and modelled sheet conductance of real nonwoven fabrics, assuming zero contact resistance	157
6.16	The measured and modelled sheet conductance of real nonwoven fabrics, with an estimated contact resistance of $8.6k\Omega$	157
6.17	The predicted number of contacts per fibre for a real nonwoven fabric	158
6.18	Visual confirmation of the typical number of fibre contacts per fibre in a $25g/m^2$ carbon fabric	159
6.19	The CAD and mesh geometries of a $4g/m^2$ carbon nonwoven . . .	160
6.20	The CAD and mesh geometries of an $18g/m^2$ carbon nonwoven .	161
6.21	Transmitted and reflected waveforms	162
6.22	Energy for the stopping criterion, set at -80dB	163
6.23	The simulated shielding effectiveness of 10 sampled regions (for each areal weight) of carbon nonwoven fabric	164

List of figures

6.24	The magnetic field strength above and below a $4g/m^2$ nonwoven, illuminated by a 5 GHz plane wave	165
6.25	The mean shielding effectiveness of TLM simulations, plotted with one standard deviation and comparison to mean absorber measurements	166
6.26	The simulated high frequency shielding effectiveness of a $10g/m^2$ carbon nonwoven fabric (up to 200 GHz)	167
7.1	Mapping of the contact points locations from the MCM model for an areal dimensionless concentration $\tilde{n}_A = 59$	173
7.2	CAD geometry of a $50g/m^2$ carbon nonwoven fabric (truncated X-Y plane)	174
7.3	A conceptual drawing showing a jig allowing for the measurement of fibre contact resistance versus angle and pressure	175

List of tables

2.1	Electromagnetic parameters of different materials, thickness $d = 0.01mm$, Relative Permeability $\mu_r = 1$ and relative permittivity $\epsilon_0 = 1$	41
3.1	Carbon fibre properties [38]	82
3.2	Liquid binder properties [39]	82
3.3	The deduced masses of carbon fibre and polyester binder in various areal weight nonwoven fabrics	83
4.1	Equipment details	106
5.1	The coefficients of the double Gaussian PDF	118
5.2	Calculated Geometry Factor values of the nonwoven veil using two methods	121

Acknowledgements

The greatest of thanks to my supervisors Dr. John Dawson and Prof. Andy Marvin for their support, guidance and knowledge throughout the duration of the project and Dr. Ian Flintoft for his insights, experience and some much used programming functions. My gratitude to my colleagues Dr Mike Jeschke and Dr Mandy Clement for their advocacy and advice. I would also like to thank my parents Mark and Christine, my brother Matthew, and my partner Natalya for their love and support.

This research was made possible due to the financial and moral support of Technical Fibre Products Ltd - an advanced nonwoven fabric manufacturer who employ a proprietary wet-laid process to manufacture nonwoven fabrics for an array of applications including; electromagnetic shielding, fracture toughness, ground plane, fire protection and cryogenic insulation to name a few. Technical Fibre Products are a subsidiary of James Cropper PLC, a 6-generation, family owned advanced material business. Collectively, they describe themselves as:

'creating some of the world's most distinctive and technically advanced paper products, using materials from cotton and wood to carbon fibre. We support industries from packaging to aerospace with products that are at the cutting edge of performance' [1]

Declaration

I declare that this thesis is a presentation of original work and I am the sole author. This work has not previously been presented for an award at this, or any other, University. All sources are acknowledged as References. In addition to this thesis, I have published the following papers as part of the research conducted towards my PhD.

1. A. N. Austin, J. F. Dawson, I. D. Flintoft and A. C. Marvin "Analysis of the shielding properties of metalized nonwoven materials", International Symposium on Electromagnetic Compatibility (EMC EUROPE), Brugge, 526-531, September 2013.
2. A. N. Austin, J. F. Dawson, I. D. Flintoft and A. C. Marvin "Modelling the micro-structure of non-uniform conductive non-woven fabrics: Determination of sheet resistance", International Symposium on Electromagnetic Compatibility, Dresden, 1-6, August 2015.
3. J. F. Dawson, I. D. Flintoft, A. N. Austin, A. C. Marvin, "Shielding Effectiveness of Non-woven Carbon Fibre Sheets: Modelling the Micro-structure", European Space Agency (ESA), Valencia, 1-5, May 2016.
4. Dawson, J. F.; Austin, A. N.; Flintoft, I. D. Marvin, A. C. , "Shielding Effectiveness and Sheet Conductance of Nonwoven Carbon-fibre Sheets", IEEE Transactions on Electromagnetic Compatibility, vol. 59, no. 1, 84-92, February 2017.

Chapter 1

Introduction

Introduction

1.1 Overview and Industrial Context

Electromagnetic interference (EMI) is an extremely diverse discipline, spanning a multitude of applications and markets due to the proliferation of the electronics industry. Without the appropriate use of shielding technology, electromagnetic interference can cause any electric device to malfunction or fail completely. Due to the many different systems that require shielding and the fast rate of development within the electronics industry, the EMI market is expected to grow to £4 billion by 2019 [2].

There is growing demand in the aerospace, automotive and defence industries for lightweight composite structures that save fuel, improve mechanical performance and possess similar electromagnetic properties to their metal predecessors, so that electronic systems remain shielded from unwanted EMI. Today's composite structures, primarily constructed from glass fibre, often fall short in this respect because they lack the requisite levels of electric conductivity and magnetic permeability. In order to restore this functionality to the composite, a range of traditional shielding materials are available which includes but is not limited to; wire meshes, metal foils, films, and conductive paints. Each of these solutions has been studied in detail by the Electromagnetic Compatibility (EMC) community over the past 25 years and their behaviour is well understood. Depending on the primary, secondary and tertiary performance requirements (such as degree of shielding effectiveness, importance of weight reduction and process compatibility) engineers have to choose the most effective material solutions for minimal cost.

A recent addition to these shielding materials is conductive nonwoven fabrics which are intrinsically porous, infusible, web-like structures, consisting of arrays of short chopped, conductive fibre. Conductive nonwoven fabrics are of interest because they provide efficient ways to improve conductivity and control electromagnetic effects within composite structures for minimal weight and thickness gain. The relative importance of composite materials is shown in figure 1.1.

This project involves understanding the interactions between conductive nonwoven fabrics and electromagnetic fields such that their shielding and electric behaviour can be better predicted and optimised.

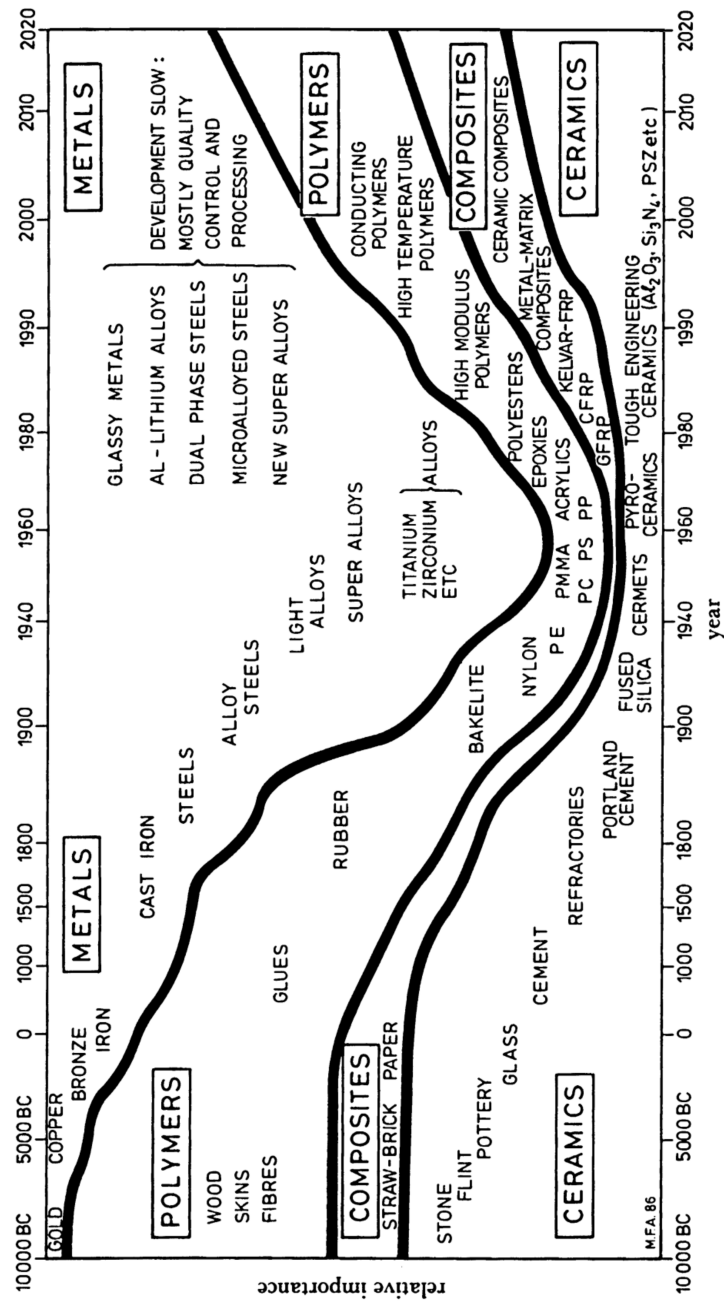


Fig. 1.1 The evolution of the composites industry through history and its importance today. Reproduced with permission [3].

Introduction

1.2 Motivation and Scope

'God is in the detail' - Ludwig Mies van der Rohe

The ability to predict, optimise, and demonstrate the electromagnetic performance of nonwoven fabrics throughout a range of applications is a powerful engineering proposition, which enables a systems level approach to be considered ¹. By first understanding a given application's requirements, the correct material parameters can be selected and simulated in order to check if the desired performance targets will be met. Subsequent parametric analysis and simulation can then be used to improve the product configuration and optimise performance. This significantly increases the chances of developing a successful solution and ensures that any time spent preparing physical samples is done so using the most suitable materials from the outset. Computational modelling is thus a sophisticated product development method which provides a better understanding of the underlying physics and avoids the uncertainty and lost time associated with simple trial and error approaches. Once computational models of the nonwoven micro-structure have been sufficiently validated in one domain, they have the potential to be transferred to a broad range of multi-disciplinary problems including; electromagnetic, thermal, mechanical, chemical, and fluid.

The scope of this research includes:

- Measurement of the electromagnetic properties by considering both the radio frequency shielding effectiveness (1-8.5 GHz) and the quasi-static sheet conductance.
- Consideration of classical electromagnetic models in predicting nonwoven fabric behaviour by applying semi-empirical techniques and conducting suitable parametric analysis. This also includes using existing models of homogeneous sheets and periodic structures that are defined in the literature review.
- Production of micro-structural nonwoven fabric models using Monte Carlo approaches - using knowledge of the physical properties of the material including; the sheet properties, fibre morphology, fibre orientation, fibre quantity, and bulk properties. The nonwoven's micro-structure is a compli-

¹Systems level approaches are frequently used in science and engineering to understand complex scenarios by considering both modular and holistic views, allowing a system's total performance to be understood at many different levels.

1.3 Original Contributions

cated and challenging structure to model accurately and the foundation of this study.

- Development of numerical models which can be used to simulate the quasi-static and radio frequency electromagnetic performance.
- Formulation of an analytic basis to describe the nonwoven fabric's quasi-static electromagnetic behaviour which can be compared to the experimental and numerical sheet conductance values previously generated.

The hypothesis of this work states that:

Accurate electromagnetic simulations of nonwoven fabrics are possible through the generation of three-dimensional micro-structural models, using semi-empiric, numeric and analytic means.

1.3 Original Contributions

This project presents the following original contributions to the field of electromagnetic modelling of wet-laid nonwoven fabrics:

1. Validated micro-structural models of conductive nonwoven fabrics leading to:
 - Fully meshed 3D CAD geometries
 - Equivalent circuit models allowing the prediction of the quasi-static sheet conductance
 - Full-wave radio frequency electromagnetic models of the shielding effectiveness
2. A new measurement technique used to determine the fibre angle distribution in 3D anisotropic materials
3. A full 3D analytic formulation of the material's sheet conductance, allowing for the efficient calculation and relation of the key physical parameters.

Introduction

1.4 Outline of the Thesis

Chapter 2 introduces the key electromagnetic wave theory, including free space propagation, near and far field effects and the impact of lossy and conductive media on the propagation constant. The fundamental shielding theory is presented followed by a detailed discussion of the transmission and reflection mechanics that occur at different material boundaries. More complicated aperture containing materials are finally considered, treated using polarisability theory and the impact of apertures on the shielding effectiveness of planar materials is demonstrated.

Chapter 3 introduces nonwoven fabrics, their manufacture, constituent properties, and key physical properties such as; thickness, fibre angle distribution, density, average pore size and micro-structure. The percolation theory of conductive networks is also introduced as well the main electrical conduction mechanisms in the structure.

Chapter 4 contains an overview of the key experimental measurements used to quantify the electrical properties of nonwoven fabrics using a range of quasi-static and radio frequency techniques. The polarization specific sheet conductance and planar shielding effectiveness are quantified and then compared to each other using curve fitting and extrapolation techniques.

Chapter 5 focuses on the development of analytic and numerical models used to simulate the nonwoven fabric's conductive behaviour. A novel method to quantify the fibre angle distribution is established, followed by the development of a Monte Carlo based micro-structural model. Information about the geometry of the model is then used to construct a corresponding circuit model in order to simulate the sheet conductance. Finally 2D and 3D analytic formulations of the material's sheet conductance are presented which relate key physical parameters to the sheet conductance.

Chapter 6 discusses the results from the analytic and numerical models explained in Chapter 5 and compares them to the experimental measurements in Chapter 4. Additional results are extracted from the numerical model and discussed, such as the mean number of contacts per fibre; the mean inter-fibre contact resistance and the percolation threshold.

1.4 Outline of the Thesis

Chapter 7 draws conclusions from the previous Chapters to bring this work to a close. A validation of the hypothesis, discussion of key achievements and future work is also included.

Chapter 2

Shielding Theory and Modelling Techniques

2.1 Overview

This chapter introduces the key theory required to understand the nature of electromagnetic field interactions with physical media. It begins with a discussion of the fundamental electromagnetic theory, starting with electromagnetic wave propagation in free space, near to far field relationships and the effects of lossy and conductive media on the propagation constant. For the planar material shielding effectiveness the influence of thickness and conductivity are then explored, followed by a short discussion of the shielding effectiveness of three dimensional structures in which the size and shape of the shielding enclosure play an important role. The wave mechanics by which electromagnetic fields reflect and transmit through a material's boundary is considered in detail. Having established the behaviour in classical homogeneous shields, a polarizability theory for simple aperture containing shields is presented and used to model a simple structure at the end of the chapter.

2.2 Electromagnetic Wave Theory

The term shielding effectiveness can be defined as the ability of a material to obstruct the transmission of electromagnetic fields into a given region. A shield may be of a planar or a three dimensional form (such as an enclosure), both of which are discussed later in this section. Prior to this the fundamental electromagnetic wave theory is introduced.

The debate as to whether light is a particle, a wave or both still exists to this day. These ideas first began between Christian Huygens who developed the first comprehensive wave theory of light (1690) and Isaac Newton whose corpuscular theory required the existence of light particles. In 1873, James Clerk Maxwell explained light as the propagation of electromagnetic waves, which Heinrich Hertz's experiments later appeared to verify. Wave theory was the most widely accepted theory of light, until 1905 when Albert Einstein used photons to describe the photoelectric effect (no wave theory equivalent was possible). In the 20th century, the pilot wave model was developed by Louis de Broglie and David Bohm, which proposed that systems exhibit both properties simultaneously - that is light as a particle whose path is guided by an underlying pilot wave. Today scientists accept the existence of light particles (photons) along with the wave-particle paradox.

The energies associated with the visible region of the spectrum are much higher than that of microwaves, $3.61e^{-19}$ versus $6.62e^{-25}$ J respectively, as determined using the Planck relation $E = \frac{hc}{\lambda}$. Because of the lower energies associated with microwaves, there is less statistical information available compared to the high energy, visible range and beyond cases. Therefore a wave theory approach makes more sense and is used for the remainder of this thesis.

2.2.1 Propagation in Free Space

An electromagnetic wave travelling in free space has two components; an electric field and a magnetic field. Both of these components are at right angles to each other and the direction of propagation (specified by the Poynting vector $\mathbf{E} \times \mathbf{H}$). The physical relationship between the electric and magnetic components of the wave is shown in figure 2.1.

Shielding Theory and Modelling Techniques

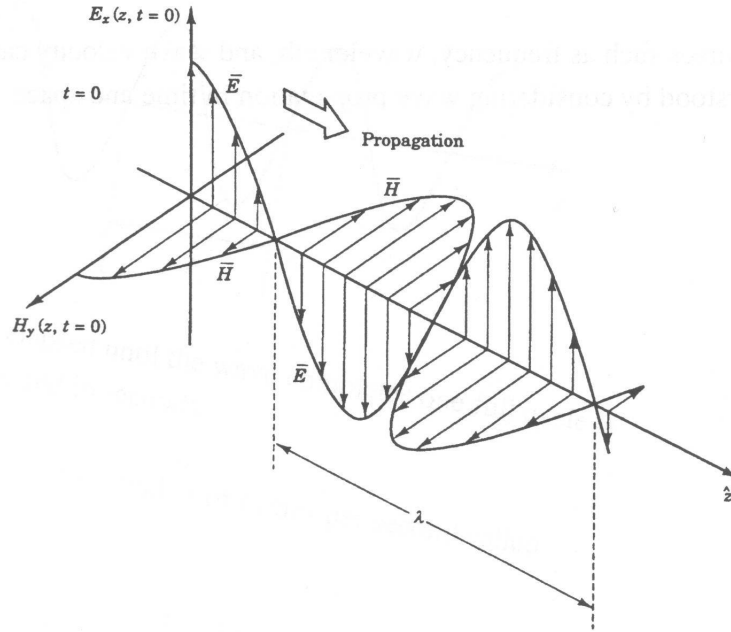


Fig. 2.1 An electromagnetic wave propagating in free space [4]

The components of an electromagnetic field polarized in the x direction can be described using the following exponential functions:

$$E_x^i = \hat{a}_x E_0 e^{-j\beta z} \quad (2.1a)$$

$$H_y^i = \hat{a}_y H_0 e^{-j\beta z} \quad (2.1b)$$

Where E_0, H_0 is the amplitude of the electric and magnetic field components and β is the number of wavelengths per 2π units of distance:

$$\beta = \frac{2\pi}{\lambda} \quad (2.2)$$

The wave impedance of free space, η_0 , can also be defined:

$$\eta_0 = \frac{E}{H} = \sqrt{\frac{\mu_0}{\epsilon_0}} = 376.73\Omega \quad (2.3)$$

2.2 Electromagnetic Wave Theory

2.2.2 Near and Far Fields

Different wave characteristics are seen to dominate depending on the distance from an electromagnetic source. These regions can be defined as the near field, the transition region and the far field shown in figure 2.2, which also shows how the wave impedance changes with normalised distance from the antenna for both electric and magnetic dominating field modes.

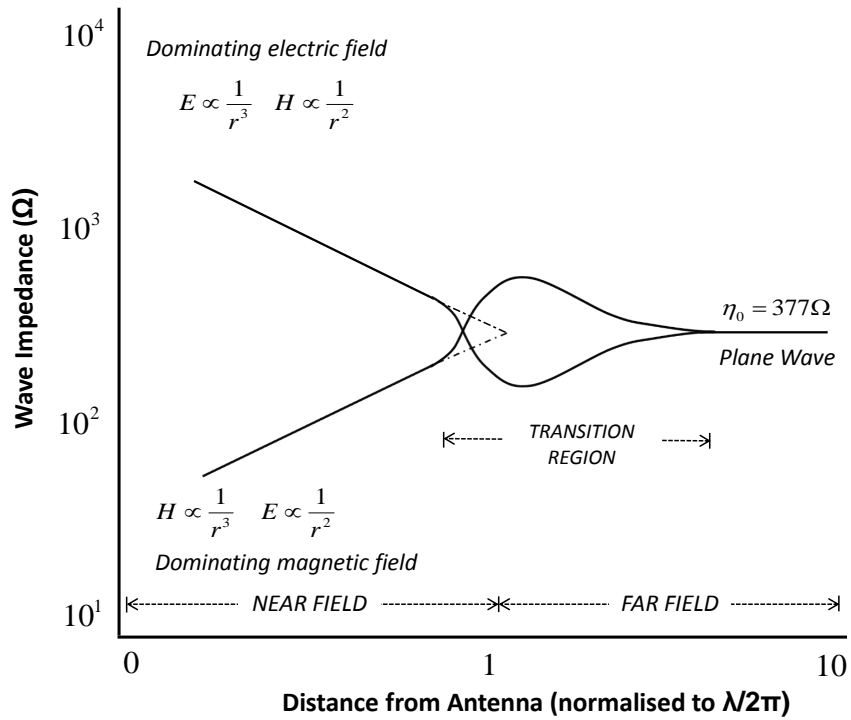


Fig. 2.2 The change in wave impedance as a function of distance based on [5]

The near field: is split into reactive and radiating regions. Within this near field zone all polarization types can exist (i.e. vertical, horizontal and circular). Extremely close to the source (the reactive nearfield zone) the relationship between E and H is very complex to predict and either component may dominate. To calculate the power density at this point, separate measurements of E and H are required, as well as additional phase relationship measurements between the two. The remaining radiative zone contains no reactive components; however the relationship between E and H remains complex. When $D > \lambda$, the radiative zone

Shielding Theory and Modelling Techniques

begins at a distance r_1 [6]:

$$r_1 \geq 0.62 \sqrt{\left(\frac{D^3}{\lambda}\right)} \quad (2.4)$$

The far field: As the wave propagates further from the source, the impedance E/H becomes a constant value of 377 ohms and the wave front can be defined as planar and far field. The wave can be characterised by a single polarization type vertical, horizontal or circular. This far field point (known as the Rayleigh range) occurs from a distance r_2 :

$$r_2 \geq \frac{2D^2}{\lambda} \quad (2.5)$$

from the signal source, where D represents the largest radiating dimension of the antenna. The far field distance is sometimes also expressed independently of antenna size using $\frac{\lambda}{2\pi}$ [7]. Beyond this far field transition point the wave's impedance remains at 377 ohms and does not change unless the wave interacts with a boundary of different impedance.

2.2.3 Propagation in Media

Now that we have described electromagnetic wave propagation in free space, it is important to establish propagation phenomena within lossy and conductive media (such as those used in shielding applications).

Within lossy media a description of the propagation requires not only phase information β but also attenuation information α . Both of these parameters can be used to define the propagation constant γ :

$$\gamma = \alpha + j\beta \quad (2.6a)$$

$$\gamma = \sqrt{j\omega\mu(\sigma + j\omega\epsilon)} \quad (2.6b)$$

The propagation constant describes how the amplitude and phase of an electromagnetic wave evolves as it advances through a medium.

2.2 Electromagnetic Wave Theory

The real part of the propagation constant (α) describes how the waves amplitude deteriorates with distance in a given medium. This parameter is zero when the propagation media is lossless (perfect vacuum) i.e the amplitude of the wave doesn't fall. The attenuation constant α :

$$\alpha = \omega\sqrt{\mu\epsilon} \left\{ \frac{1}{2} \left[\sqrt{1 + \left(\frac{\sigma}{\omega\epsilon} \right)^2} - 1 \right] \right\}^{1/2} \quad (2.7)$$

The attenuation constant $\alpha = 1/\delta$, where δ is the skin depth.

The imaginary part of the propagation constant β , describes how the phase of the wave changes with distance. β is often treated equally to the wave number κ however this is dependent on the propagation medium. The Phase Constant β :

$$\beta = \omega\sqrt{\mu\epsilon} \left\{ \frac{1}{2} \left[\sqrt{1 + \left(\frac{\sigma}{\omega\epsilon} \right)^2} + 1 \right] \right\}^{1/2} \quad (2.8)$$

Within good conductors, where $\sigma \gg \omega\epsilon_0\epsilon_r$, and alpha and beta are equal yielding:

$$\alpha = \beta = \sqrt{\frac{\omega\mu\sigma}{2}} \quad (2.9)$$

Having considered the basic electromagnetic wave propagation we can now introduce the core shielding theory.

2.3 Shielding Effectiveness Theory

2.3.1 Schelkunoff's Shielding Theory

This section introduces the theory which is applicable to homogeneous planar media i.e. foils, films and bulk materials. Schelkunoff [8] was responsible for the development of the original sheet material model which was later worked on by Schulz [9] who added correction terms for shield discontinuities such as apertures. This section outlines the key results from Schelkunoff's work and is based on Balanis [6], and Kraus [10].

The shielding effectiveness of an enclosure is defined as the ratio of the magnitude of a field in the absence (E_0, H_0) and presence (E_S, H_S) of a shield (enclosure) shown in figure 2.3:

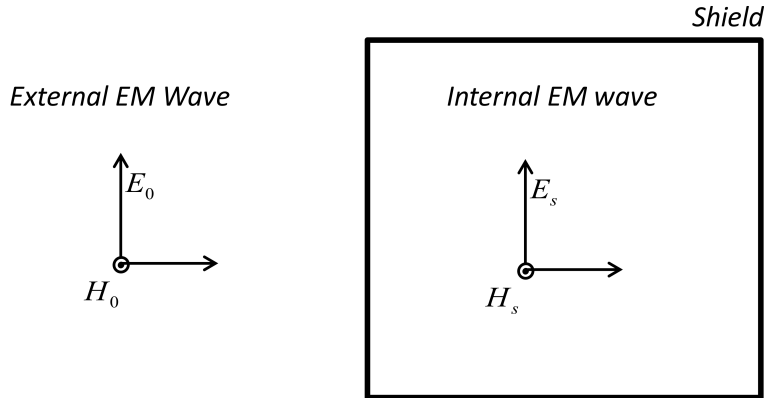


Fig. 2.3 The shielding effectiveness of an enclosure

$$S_E = 20 \log_{10} \left(\frac{E_0}{E_S} \right) \text{ (dB)} \quad (2.10a)$$

$$S_M = 20 \log_{10} \left(\frac{H_0}{H_S} \right) \text{ (dB)} \quad (2.10b)$$

In the case of a planar, single layer shield which is electrically thin ($d \ll \delta$) and conductive ($\sigma \gg \omega \epsilon_0 \epsilon_r$), the low frequency shielding effectiveness can be

2.3 Shielding Effectiveness Theory

approximated [11] using the sheet resistance (R_s) of the shield:

$$SE = 45.51 - 20 \log_{10} (R_s) \text{ (dB)} \quad (2.11)$$

However, in order to understand the frequency dependent nature of the shielding effectiveness and key mechanisms, a more careful inspection of the incident and transmitted fields is required, first proposed by Schelkunoff [8]. Assuming the shield is in the far field of the source:

$$SE = \frac{\vec{E}_i}{\vec{E}_\tau} = \frac{(\eta_0 + \eta)^2}{4\eta_0\eta} \left[1 - \left(\frac{\eta_0 - \eta}{\eta_0 + \eta} \right)^2 e^{-2d/\delta} e^{-j2\beta d} \right] e^{d/\delta} e^{j\beta d} e^{-j\beta_0 d} \quad (2.12)$$

where the intrinsic material impedance is $\eta = \sqrt{\frac{\mu}{\epsilon}}$ for lossless media and $\eta = \sqrt{\frac{j\omega\mu}{\sigma + j\omega\epsilon}}$ for lossy media.

This is derived in more detail in section 2.4. The decibel form of this expression can be defined as the sum of the reflection loss, absorption loss and multiple reflections [12]

$$SE_{dB} = R_{dB} + A_{dB} + M_{dB} \quad (2.13a)$$

$$SE_{dB} = \underbrace{20 \log_{10} \left| \frac{\eta_0}{4\eta} \right|}_{R_{dB}} + \underbrace{20 \log_{10} e^{d/\delta}}_{A_{dB}} + \underbrace{20 \log_{10} \left| 1 - \left(\frac{\eta_0 - \eta}{\eta_0 + \eta} \right)^2 e^{-2d/\delta} e^{-j2\beta d} \right|}_{M_{dB}} \quad (2.13b)$$

Results of Schelkunoff's shielding effectiveness expressions for different thicknesses of planar copper are shown in figure 2.4. The flat portion of the shielding response is influenced significantly by the material's sheet resistance. As the frequency increases, skin effect losses increase and when the skin depth becomes comparable to the material's thickness, the shielding effectiveness increases exponentially with frequency.

The shielding effectiveness of various materials is shown in figure 2.5, with a chosen thickness of 0.01mm (similar to nonwoven fabrics). The different material conductivities (listed in table 2.1) on the shielding effectiveness can be observed, which impacts both the sheet resistance and skin depth (the latter of which is discussed in more detail in the next section).

Shielding Theory and Modelling Techniques

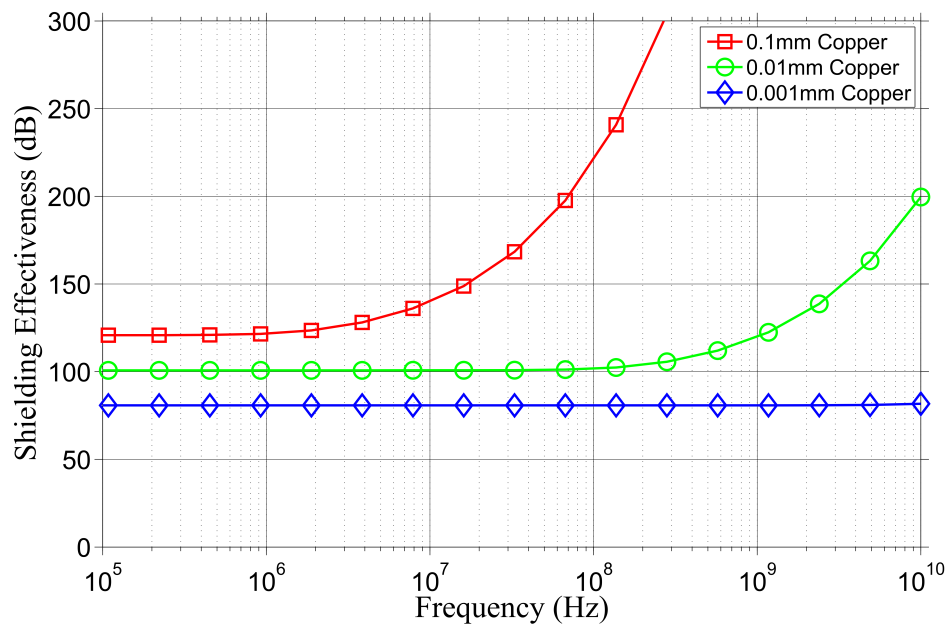


Fig. 2.4 Various thickness of copper and corresponding shielding effectiveness as predicted by the Schelkunoff model

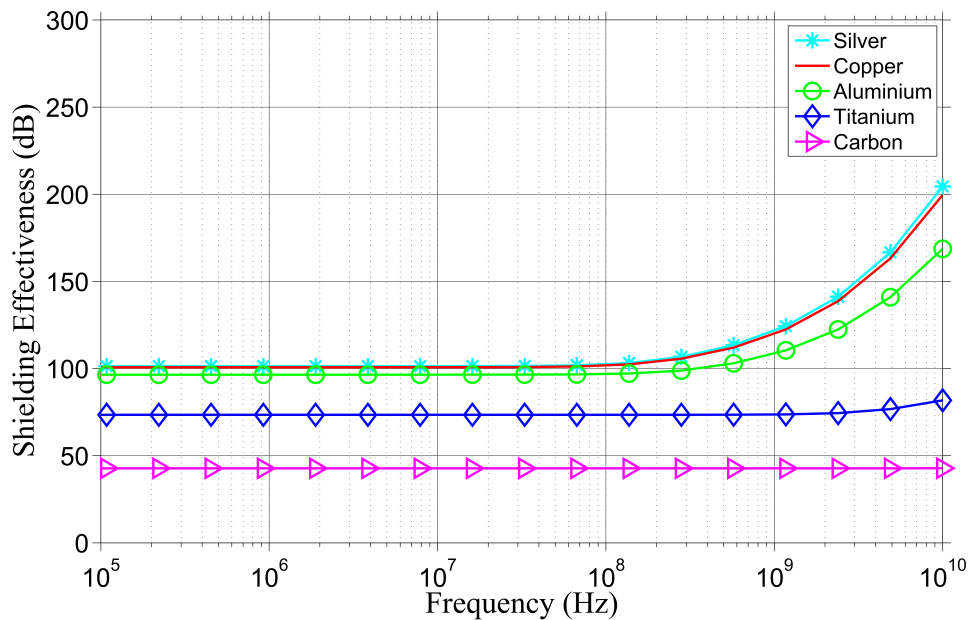


Fig. 2.5 The shielding effectiveness of various materials with 0.01 mm thickness, as predicted by the Schelkunoff model

2.3 Shielding Effectiveness Theory

Table 2.1 Electromagnetic parameters of different materials, thickness $d = 0.01mm$, Relative Permeability $\mu_r = 1$ and relative permittivity $\epsilon_0 = 1$.

Element	Conductivity σ (S/m)
Silver	6.21×10^7
Copper	5.80×10^7
Aluminium	3.54×10^7
Titanium	2.50×10^6
Carbon	7.25×10^4

Shielding Theory and Modelling Techniques

Skin effect

The skin effect is the tendency for alternating current (AC), generated from an incident electromagnetic wave, to flow near the outer surface of an electrical conductor - a consequence of the attenuation of the wave propagating into a lossy material. The skin depth of the material can be defined as the point at which the incident field is reduced by a factor of $1/e$ or 37% its value at the surface. The effect is dependent on the frequency, conductivity, and relative permeability of the metal. It is described in its most complete form as the inverse of the attenuation constant 2.8, however a more common form (approximate for good conductors) is:

$$\delta = \frac{1}{\sqrt{\pi f \mu_0 \mu_r \sigma}} \quad (2.14)$$

Where, σ = Conductivity S/m , μ_0 = Magnetic permeability of free space $4\pi \times 10^{-7}(H/m)$, μ_r = Relative magnetic permeability

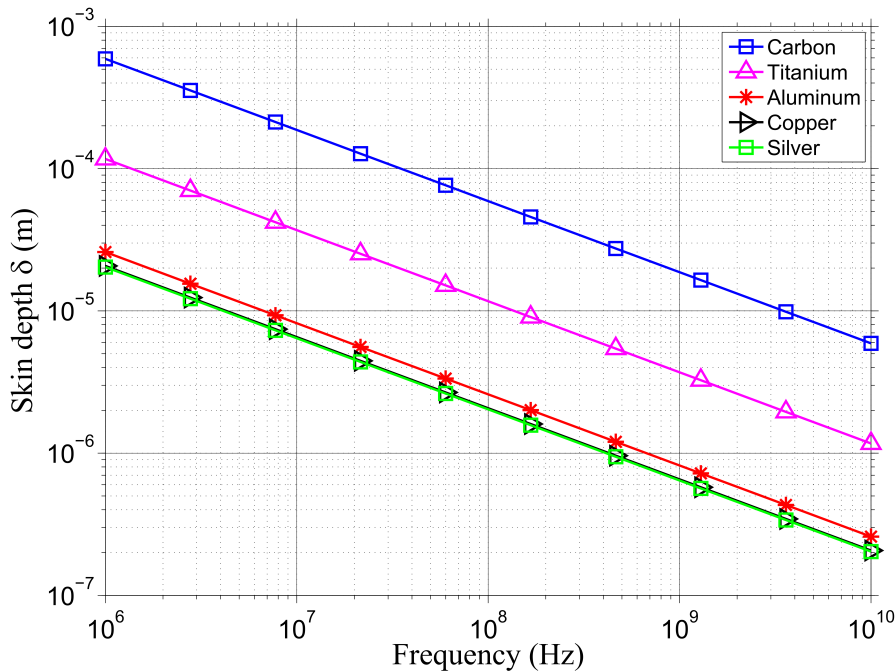


Fig. 2.6 The skin depth of different materials

Figure 2.6 shows the skin depth in various non-magnetic materials between 1 MHz and 10 GHz. Aluminium, copper and silver all have similar conductivity and therefore similar skin depths, whereas carbon has a lower conductivity resulting in a slightly deeper skin depth.

2.3 Shielding Effectiveness Theory

It is interesting to consider the definition of skin depth in relation to the nonwoven fabrics in this study. In the 1-8.5 GHz region, the skin depth in a homogeneous sheet of carbon is between 6 - 11 microns, which is greater than the diameter of a single carbon fibre (7 microns). Although carbon based nonwoven fabrics are usually at least a couple of fibres thick, they are not homogeneous materials and possess a changing local thickness with many sub-wavelength apertures (discussed in chapter 3). This makes it harder to define the skin depth in such materials and requires a treatment of electromagnetic wave interaction with apertures, discussed in section 2.4.5.

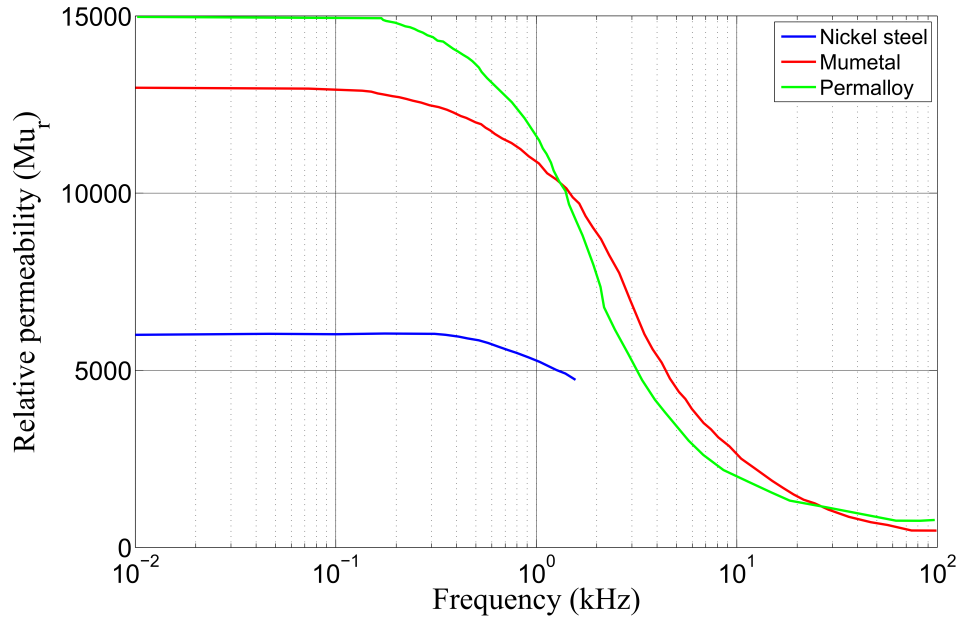


Fig. 2.7 The frequency dependency of the relative magnetic permeability for magnetic metals [13]

For ferromagnetic materials (such as iron, nickel and cobalt) the skin depth is much harder to predict due to the frequency (figure 2.7) and field strength dependence of the magnetic permeability term. Such materials' high permeability allows them to concentrate external magnetic field lines by more than 10 times their original density, reducing the skin depth value. However, the magnetic permeability for most magnetic materials falls to unity in the high kilohertz to megahertz range, nullifying the effect. Additionally, as the external magnetic field strength increases and the material becomes saturated, the peak magnetic permeability also falls significantly.

2.3.2 Kaden's Shielding of Enclosures

The shielding effectiveness of an enclosure (shown in figure 2.8) is dependent not only on the material properties but also the size and shape of the enclosure, its contents and the measurement position within the cavity. Additional effects must be considered, such as cavity resonance. Enclosures are used in practise (rather than flat materials) as they prevent field leakage around the edge of the shield, particularly in the case of magnetic fields.



Fig. 2.8 A typical example of simple shielding enclosure

A continuous, perfectly conducting spherical shell of material represents an ideal shielded enclosure which as a result of Gauss's law $\oint E \cdot dL \equiv 0$ prevents all static fields from penetrating. Such a material would possess an infinite shielding effectiveness. However, in reality materials have a finite conductivity and often compromised geometry due to the presence of slots, seams, holes, access doors and cables.

Analytic expressions for shielded enclosures

Analytic enclosure shielding expressions were first proposed by Kaden [14] in 1959, which provided solutions for idealised geometries (spheres, cylinder, parallel flat plates etc). The solutions assume that the geometries are simple (that is continuous with no apertures), non-resonant and the illuminating field is quasi-static.

Further assumptions ensure that the direction of the magnetic field is parallel to the principal geometric axis, and that the material shell is electrically linear.

2.3 Shielding Effectiveness Theory

For a continuous sphere, the electric and magnetic shielding effectiveness in the quasi-static case is:

$$SE_E = 20 \log_{10} \left| \frac{2\gamma \sinh \gamma d}{3\omega^2 \epsilon \mu R} \right| \quad (2.15a)$$

$$SE_M = 20 \log_{10} \left| \cosh \gamma d + \frac{1}{3} \left[\frac{\gamma R}{\mu} + \frac{2(\mu - 1)}{\gamma R} \right] \sinh \gamma d \right| \quad (2.15b)$$

Where: $\gamma = \sqrt{j\omega\mu\sigma}$ is the propagation constant of the material, R is the radius of the spherical enclosure and d is the material thickness. Even relatively poor conductors yield good electric field shielding at low frequencies, although this is not true for low frequency magnetic fields. For such cases high permeability materials are required. At low frequencies Kaden's expression (2.15) simplifies to:

$$SE_M = 20 \log_{10} \left(1 + \frac{2(\mu - 1)d}{3R} \right) \quad (2.16)$$

Therefore increasing the material thickness and magnetic permeability μ both improve the shielding performance. These formulae work well until the frequency increases to a point where the quasi-static approximation begins to break down. This approximately takes place when $f = \frac{c}{6R}$ and cavity resonance occurs [15].

Apertures and joints in enclosures

An enclosures design often compromises its shielding effectiveness as necessary features such as ventilation slots, apertures, seams and access panels are of importance to its operation. A good example of this is a Personal Computer case shown in figure 2.9.

Such features often present a contact resistance (particularly in composite structures) which can interrupt the induced current flow from an illuminating field. This effect is most severe when the slot/seam lies orthogonal to the polarization field.

The manifestation of this interruption of current flow, is that the slot radiates a field into the cavity of the box reducing the enclosure's shielding effectiveness. This radiation can produce a more dramatic drop in the shielding effectiveness due to cavity resonance. Cavity resonance occurs at frequencies which correspond



Fig. 2.9 PC enclosure with necessary cooling apertures, cable holes, window and access door.

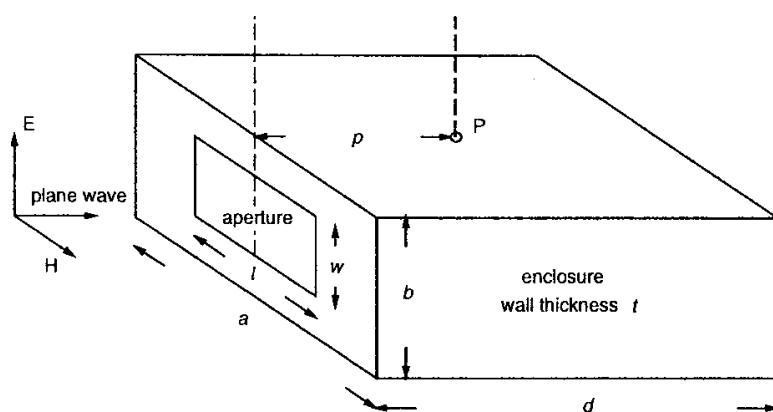


Fig. 2.10 An enclosure containing a single large aperture, reproduced with permission from [16]

2.3 Shielding Effectiveness Theory

to the electromagnetic field modes which satisfy boundary conditions of the walls of the cavity, given by:

$$f_{mnl} = \frac{1}{2\sqrt{\epsilon_r\mu_r}} \sqrt{\left(\frac{m}{a}\right)^2 + \left(\frac{n}{b}\right)^2 + \left(\frac{p}{c}\right)^2} \quad (2.17)$$

Where a, b, c are the box dimensions and m, n, p are integer mode numbers.

The resonant frequency of the cavity is dependent on the size of the box, the slot or hole size, the number of holes and the wavelength of the signal. An example of the first order resonance, in an enclosure is shown in 2.11. By reducing the size of an individual slot and replacing it with multiple slots, the amount of current interruption can be significantly reduced, minimising the slot radiation into the enclosure.

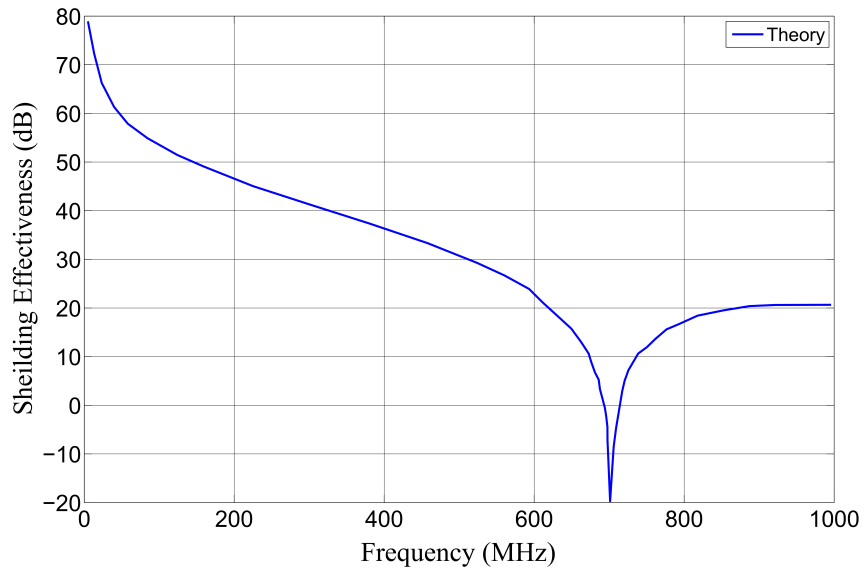


Fig. 2.11 A slotted enclosure's electric shielding effectiveness and first order resonance occurring at 700 MHz [16].

2.4 Reflection and Transmission of EM Waves

Having covered the fundamental electromagnetic and shielding theory, a more detailed discussion of electromagnetic wave propagation through different material boundaries is presented. This concentrates on infinite planar sheets and includes the effects of different material interface, field incidence angle and discontinuities in the shield (such as apertures).

2.4.1 Single Interface (normal incidence)

Initially, the transmission of a wave into a material that has only one interface is considered. A normally incident electromagnetic wave that is travelling in free space and polarized in the x direction can be described using:

$$E_x^i = \hat{a}_x E_0 e^{-j\beta_1 z} \quad (2.18a)$$

$$H_y^i = \hat{a}_y H_0 e^{-j\beta_1 z} \quad (2.18b)$$

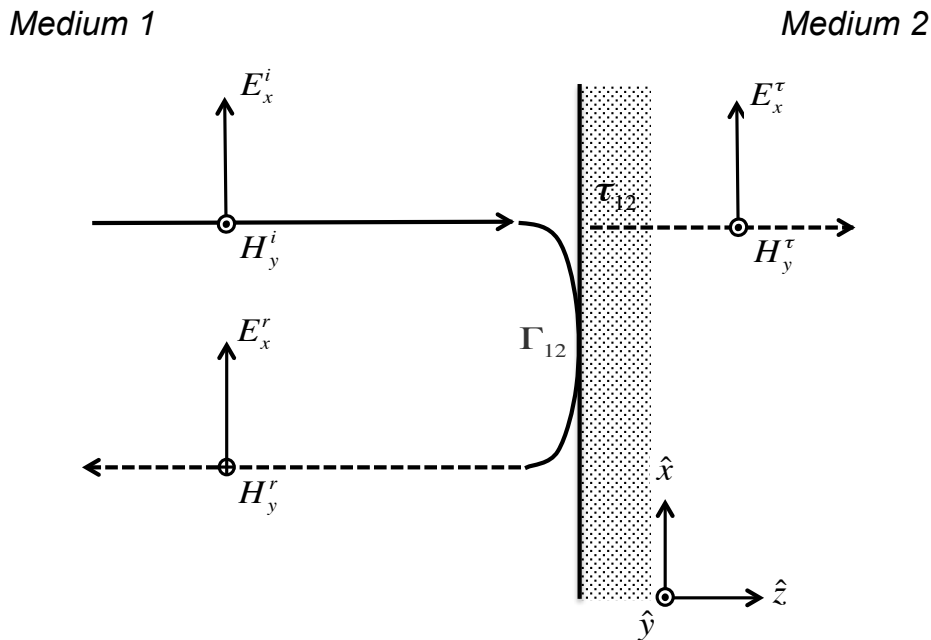


Fig. 2.12 An electromagnetic wave interaction with a single interface

2.4 Reflection and Transmission of EM Waves

As the incident wave approaches a conductive material interface, part of the signal is reflected. A reflection coefficient Γ can be defined as:

$$E_x^r = \hat{a}_x E_x^i \Gamma_{12} = \hat{a}_x E_0 e^{+j\beta_1 z} \left(\frac{\eta_2 - \eta_1}{\eta_2 + \eta_1} \right) \quad (2.19a)$$

$$H_y^r = \hat{a}_y H_y^i \Gamma_{12} = -\hat{a}_y H_0 e^{+j\beta_1 z} \left(\frac{\eta_2 - \eta_1}{\eta_2 + \eta_1} \right) \quad (2.19b)$$

Where the intrinsic impedance of the material in medium 2 is given by:

$$\eta_2 = \sqrt{\frac{j\omega\mu}{\sigma + j\omega\epsilon}} \quad (2.20)$$

The total field that exists in medium 1 is composed of incident and reflected electric and magnetic fields:

$$E_1 = E_x^i + E_x^r \quad (2.21a)$$

$$H_1 = H_y^i + H_y^r \quad (2.21b)$$

The remainder is transmitted into the lossy material, where an exponential decay in both electric and magnetic fields take place. The attenuation constant α is included in the term and an associated Transmission coefficient (T_{12}) is defined:

$$E_x^t = \hat{a}_x E_x^i e^{-\alpha z} T_{12} = \hat{a}_x e^{-\alpha_2 z} E_0 e^{-j\beta_2 z} \left(\frac{2\eta_2}{\eta_2 + \eta_1} \right) \quad (2.22a)$$

$$H_y^t = \hat{a}_y H_y^i e^{-\alpha z} T_{12} = \hat{a}_y e^{-\alpha_2 z} H_0 e^{-j\beta_2 z} \left(\frac{2\eta_2}{\eta_2 + \eta_1} \right) \quad (2.22b)$$

The total field in medium 2 is composed only of the transmitted E and H fields from medium 1:

$$E_2 = E_x^t \quad (2.23a)$$

$$H_2 = H_y^t \quad (2.23b)$$

2.4.2 Single Interface (oblique incidence)

Oblique incidence occurs when the approaching wave strikes a medium at an angle other than $\theta_i = 0$, resulting in a reflected component and transmitted component. For such incidence the polarization of the wave must be considered. Two main cases arise: when the E-field is perpendicular to the plane of incidence 2.13, and when the E field is parallel to the plane of incidence 2.14.

Reflection and Transmission for perpendicular polarization

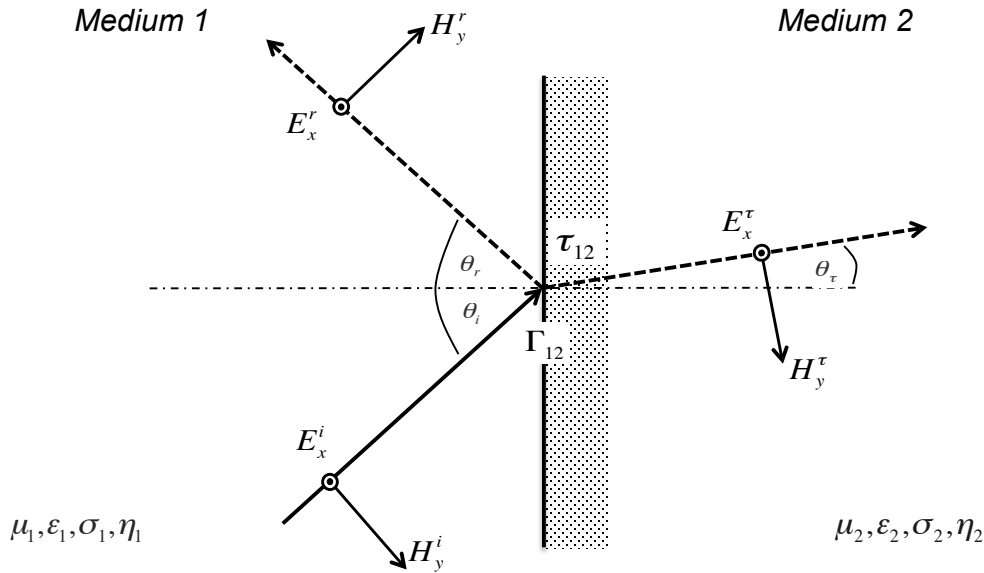


Fig. 2.13 Oblique wave incidence, perpendicular E-field polarization

As the only electric field component at the boundary can be parallel to the interface:

$$E_x^t = E_x^i + E_x^r \quad (2.24)$$

$$E_x^t = \tau_{12} E_x^i \quad (2.25a)$$

$$E_x^r = \Gamma_{12} + E_x^i \quad (2.25b)$$

2.4 Reflection and Transmission of EM Waves

Which when substituted into equation (2.24) becomes:

$$\tau_{12}E_x^i = (1 + \Gamma_{12})E_x^i \quad (2.26)$$

Which simplifies to

$$\tau_{12} = (1 + \Gamma_{12}) \quad (2.27)$$

For magnetic fields, consideration of both tangential and normal components at the interface is necessary. As the tangential magnetic fields either side of the boundary must be equal:

$$H_y^t \cos \theta_r = H_y^i \cos \theta_i - H_y^r \cos \theta_r \quad (2.28)$$

The normal component of the magnetic flux $B = \mu H$ must remain continuous across the boundary therefore:

$$\mu_2 H_y^t \sin \theta_r = \mu_1 H_y^i \sin \theta_i + \mu_1 H_y^r \sin \theta_r \quad (2.29)$$

As Snell's law of reflection requires $\theta_i = \theta_r$, equation (2.28) can be expressed as:

$$\mu_2 H_y^t \sin \theta_r = \mu_1 H_y^i \sin \theta_i (1 + \Gamma_{12}) \quad (2.30)$$

Dividing equation(2.24) by equation (2.30) we get:

$$\frac{E_x^t}{\mu_2 H_y^t \sin \theta_r} = \frac{E_x^i (1 + \Gamma_{12})}{\mu_1 H_y^i \sin \theta_i (1 + \Gamma_{12})} \quad (2.31)$$

The relation

$$\frac{E}{\mu H} = \frac{1}{\sqrt{\mu \epsilon}} \quad (2.32)$$

allows (2.31) to be expressed as:

$$\frac{\sin \theta_i}{\sin \theta_r} = \frac{\sqrt{\mu_2 \epsilon_2}}{\sqrt{\mu_1 \epsilon_1}} = \frac{n_2}{n_1} \quad (2.33)$$

Shielding Theory and Modelling Techniques

Where n is the refractive index of the material. Now that the angles of reflection and refraction are known, the reflection and transmission coefficients from the boundary can be defined:

Noting

$$H_y^r = \Gamma_{12} H_y^i \quad (2.34)$$

and

$$H_y^t \eta_2 = \tau_{12} H_y^i \eta_1 \quad (2.35)$$

$$\tau_{12} H_y^i \frac{\eta_1}{\eta_2} \cos \theta_\tau = (1 - \Gamma_{12}) H_y^i \cos \theta_i \quad (2.36)$$

Eliminating the magnetic fields:

$$\tau_{12} \frac{\eta_1}{\eta_2} \cos \theta_\tau = (1 - \Gamma_{12}) \cos \theta_i \quad (2.37)$$

Substituting equation (2.27) into (2.36):

$$(1 + \Gamma_{12}) \frac{\eta_1}{\eta_2} \cos \theta_\tau = (1 - \Gamma_{12}) \cos \theta_i \quad (2.38)$$

Re-arranging the expression becomes:

$$\Gamma_{12} = \frac{\eta_2 \cos \theta_i - \eta_1 \cos \theta_\tau}{\eta_2 \cos \theta_i + \eta_1 \cos \theta_\tau} \quad (2.39)$$

For normal incidence $\theta_i = 0$ this reduces to (2.19). The transmission coefficient is then deduced from (2.27) yielding:

$$\tau_{12} = 1 + \frac{\eta_2 \cos \theta_i - \eta_1 \cos \theta_\tau}{\eta_2 \cos \theta_i + \eta_1 \cos \theta_\tau} \quad (2.40)$$

2.4 Reflection and Transmission of EM Waves

Reflection and Transmission for parallel polarization

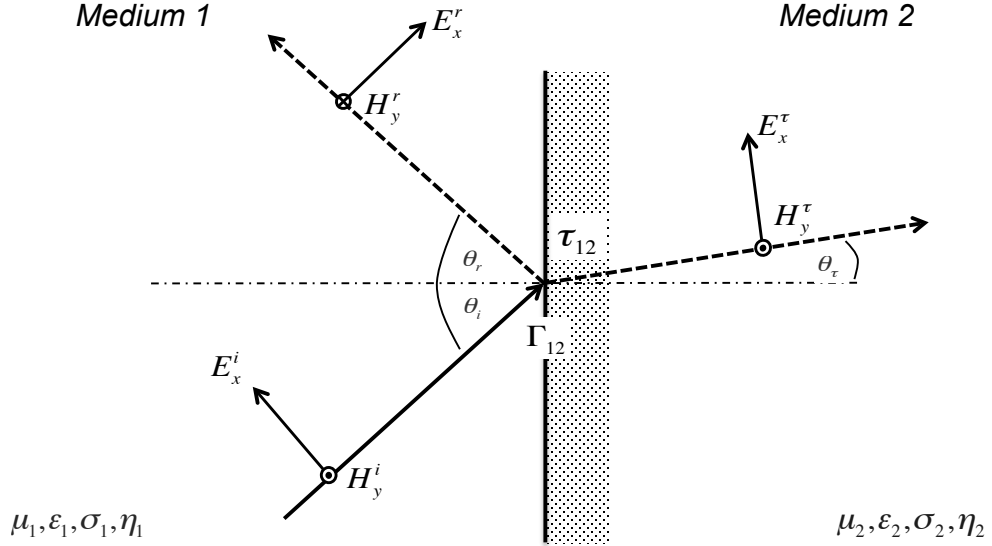


Fig. 2.14 Oblique wave incidence, parallel E-field polarization

Similar to the previous case, as the only magnetic fields at the boundary is parallel to the surface:

$$H_y^t = H_y^i - H_y^r \quad (2.41)$$

Applying equations (2.34) and (2.35) we can write:

$$H_y^t = \tau_{12} H_y^i \frac{\eta_1}{\eta_2} = H_y^i - \Gamma_{12} H_y^i \quad (2.42)$$

There are both tangential and normal components of the electric field. The tangential fields must be equal either side of the interface so:

$$E_x^t \cos \theta_t = E_x^i \cos \theta_i + E_x^r \cos \theta_r \quad (2.43)$$

and the normal electric flux density ($D = \epsilon E$) must be continuous so that

$$\epsilon_2 E_x^t \sin \theta_t = \epsilon_1 E_x^i \sin \theta_i - \epsilon_1 E_x^r \sin \theta_r \quad (2.44)$$

Shielding Theory and Modelling Techniques

Assuming Snell's law and applying equation (2.25) to (2.44)

$$\epsilon_2 E_x^t \sin \theta_\tau = \epsilon_1 E_x^i \sin \theta_i (1 + \Gamma_{12}) \quad (2.45)$$

Dividing by equation (2.42):

$$\epsilon_2 \frac{E_x^t}{H_y^t} \sin \theta_\tau = \epsilon_1 \frac{E_x^i}{H_y^i} \sin \theta_i \quad (2.46)$$

Noting that $\epsilon \frac{E}{H} = \sqrt{\mu\epsilon}$ and rearranging (2.45) we obtain:

$$\frac{\sin \theta_i}{\sin \theta_\tau} = \frac{\sqrt{\mu_2 \epsilon_2}}{\sqrt{\mu_1 \epsilon_1}} = \frac{n_2}{n_1} \quad (2.47)$$

Now the angles of reflection are known, the reflection and transmission coefficients can be solved. Taking equation (2.43) and expressing in terms of reflection and transmission coefficients:

$$\tau_{12} E_x^i \cos \theta_\tau = E_x^i \cos \theta_i (1 + \Gamma_{12}) \quad (2.48)$$

$$\tau_{12} = \frac{\cos \theta_i}{\cos \theta_\tau} (1 + \Gamma_{12}) \quad (2.49)$$

This reduces to $\tau_{12} = 1 + \Gamma_{12}$ for $\theta_i = 0$ (normal incidence). Now writing equation (2.42) as a transmission coefficient and substituting into (2.27) we get:

$$\frac{\eta_2}{\eta_1} (1 - \Gamma_{12}) = \frac{\cos \theta_i}{\cos \theta_\tau} (1 + \Gamma_{12}) \quad (2.50)$$

$$\Gamma_{12} = \frac{\eta_1 \cos \theta_\tau - \eta_2 \cos \theta_i}{\eta_2 \cos \theta_\tau + \eta_1 \cos \theta_i} \quad (2.51)$$

The transmission coefficient is then:

$$\tau_{12} = \frac{\cos \theta_i}{\cos \theta_\tau} \left(1 + \frac{\eta_2 \cos \theta_\tau - \eta_1 \cos \theta_i}{\eta_2 \cos \theta_\tau + \eta_1 \cos \theta_i} \right) \quad (2.52)$$

2.4 Reflection and Transmission of EM Waves

2.4.3 Multiple Interface (normal incidence)

We now consider a material which has two interfaces (as is commonly the case in many planar shielding foils). The electromagnetic wave now interacts with both the front and back interfaces of the material (shown in figure 2.15). To represent this, modifications to the previous expressions are necessary. The notation is adjusted here to properly account for the fields scattered from the second interface as well as the first.

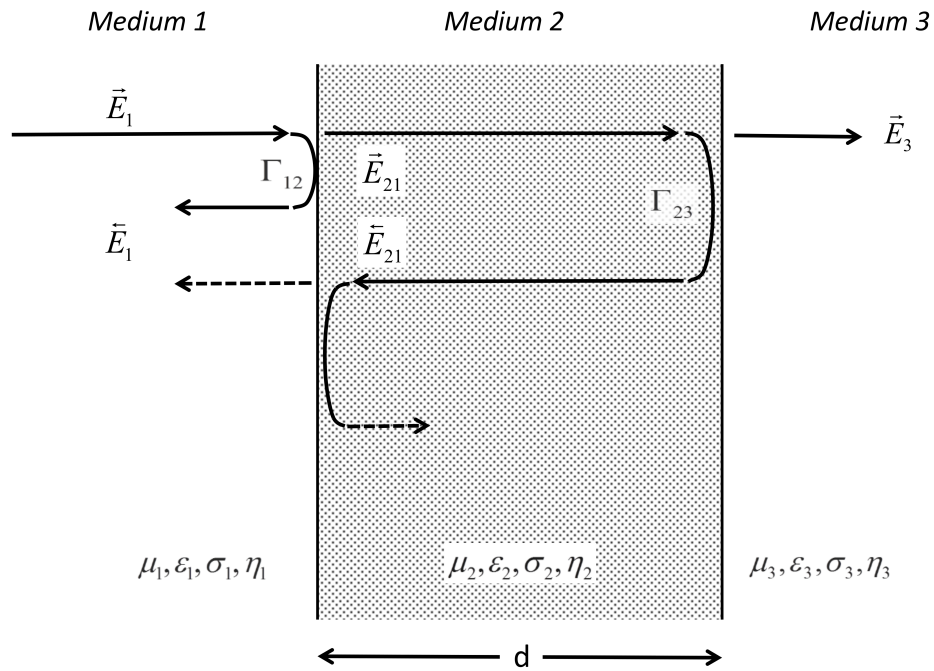


Fig. 2.15 Reflection and Transmission coefficients used at each material interface

The total field in medium 1 is now constructed from both the reflection coefficient of the first interface, plus the multiple reflections that occur within medium 2.

$$\overleftarrow{E}_1 = \vec{E}_1 \Gamma_{12} + \tau_{21} \overleftarrow{E}_{21} \quad (2.53)$$

Where \overleftarrow{E}_{21} is the backward travelling wave in medium 2, constructed from the sum of multiple reflections that occur between the two interface and defined by:

$$\overleftarrow{E}_{21} = \vec{E}_1 \tau_{12} \Gamma_{23} e^{-2\gamma_2 d_2} \left[1 + \Gamma_{21} \Gamma_{23} e^{-2\gamma_2 d_2} + \left(\Gamma_{21} \Gamma_{23} e^{-2\gamma_2 d_2} \right)^2 + \left(\Gamma_{21} \Gamma_{23} e^{-2\gamma_2 d_2} \right)^3 \dots \right] \quad (2.54)$$

Shielding Theory and Modelling Techniques

$$\vec{E}_{21}^{\leftarrow} = \vec{E}_1 \tau_{12} \Gamma_{23} e^{-2\gamma_2 d_2} \sum_{k=0}^{\infty} \left(\Gamma_{21} \Gamma_{23} e^{-2\gamma_2 d_2} \right)^k \quad (2.55)$$

Using the geometric series where $\alpha < |1|$:

$$\sum_{k=0}^{\infty} a^k = \frac{1}{1-a} \quad (2.56)$$

$$\vec{E}_{21}^{\leftarrow} = \frac{\vec{E}_1 \tau_{12} \Gamma_{23} e^{-2\gamma_2 d_2}}{1 - \Gamma_{21} \Gamma_{23} e^{-2\gamma_2 d_2}} \quad (2.57)$$

Noting that $\Gamma_{12} = -\Gamma_{21}$ and that $\tau_{12}\tau_{21} = 1 - \Gamma_{12}^2$ it can be shown equation (2.57) becomes:

$$\vec{E}_1^{\leftarrow} = \vec{E}_1 \left[\frac{\Gamma_{12} + \Gamma_{23} e^{-2\gamma_2 d_2}}{1 + \Gamma_{12} \Gamma_{23} e^{-2\gamma_2 d_2}} \right] \quad (2.58)$$

Expressing this as the reflection coefficient Γ_{13} , inclusive of the effects of materials 1 - 3:

$$\Gamma_{13} = \frac{\vec{E}_1^{\leftarrow}}{\vec{E}_1} = \frac{\Gamma_{12} + \Gamma_{23} e^{-2\gamma_2 d_2}}{1 + \Gamma_{12} \Gamma_{23} e^{-2\gamma_2 d_2}} \quad (2.59)$$

The total field in medium 3 is constructed from both the original transmitted signal plus the multiple reflections that occur within medium 2.

$$\vec{E}_{21} = \vec{E}_1 \tau_{12} \left[1 + \Gamma_{21} \Gamma_{23} e^{-2\gamma_2 d_2} + \left(\Gamma_{21} \Gamma_{23} e^{-2\gamma_2 d_2} \right)^2 + \left(\Gamma_{21} \Gamma_{23} e^{-2\gamma_2 d_2} \right)^3 \dots \right] \quad (2.60)$$

Using the same geometric series as in (2.56) it can be shown that:

$$\vec{E}_{21} = \frac{\vec{E}_1 \tau_{12}}{1 - \Gamma_{21} \Gamma_{23} e^{-2\gamma_2 d_2}} \quad (2.61)$$

and the field transmitted into medium 3 is:

$$\vec{E}_3 = \vec{E}_{32} \tau_{23} = \vec{E}_{21} e^{-\gamma_2 d_2} \tau_{23} \quad (2.62)$$

2.4 Reflection and Transmission of EM Waves

Combining these equations:

$$\vec{E}_3 = \frac{\vec{E}_1 \tau_{23} e^{-\gamma_2 d_2}}{1 - \Gamma_{21} \Gamma_{23} e^{-2\gamma_2 d_2}} \quad (2.63)$$

Finally we can express this as the transmission coefficient:

$$\tau_{13} = \frac{\vec{E}_3}{\vec{E}_1} = \frac{\tau_{12} \tau_{23} e^{-\gamma_2 d_2}}{1 - \Gamma_{21} \Gamma_{23} e^{-2\gamma_2 d_2}} \quad (2.64)$$

2.4.4 Multiple Interface (oblique incidence)

Applying the results from the previous sections the following reflection coefficients can be defined for multiple interface oblique incidence cases, shown in figure [?].

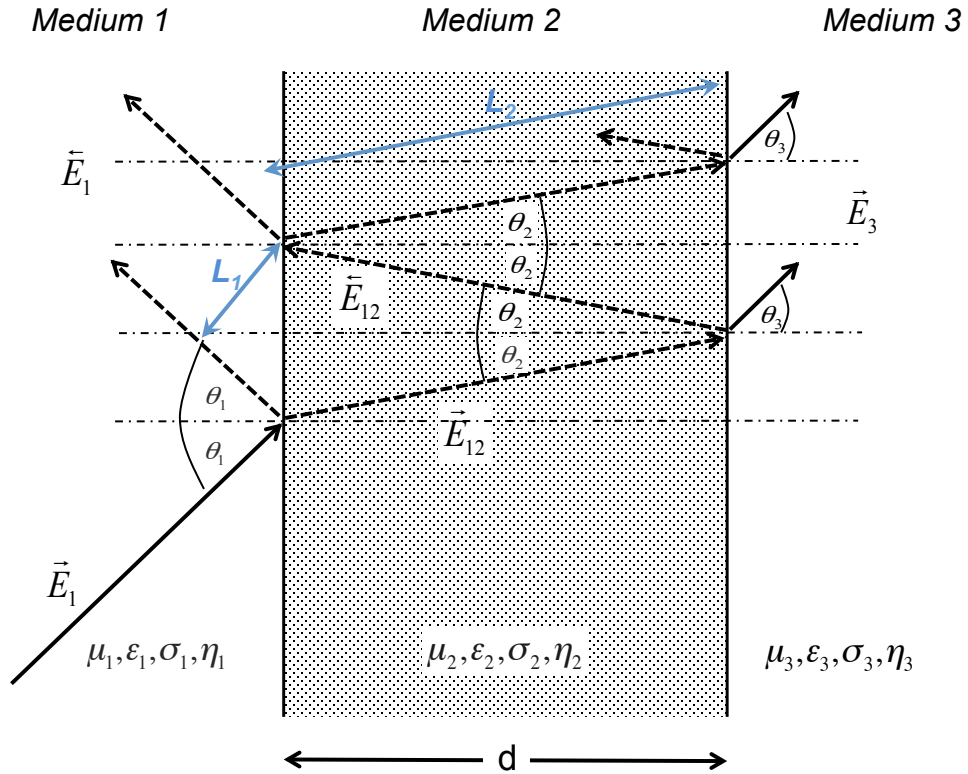


Fig. 2.16 Oblique wave incidence, upon multiple interface

Shielding Theory and Modelling Techniques

The path length in medium 2 is increased due to the angle of refraction. Therefore the propagation distance in (2.57) must be adjusted:

$$\vec{E}_1^{\leftarrow} = \Gamma_{12}\vec{E}_1 + \tau_{21}\frac{\vec{E}_1\tau_{12}\Gamma_{23}e^{\left(\frac{-2\gamma_2 d_2}{\cos\theta_2}\right)}}{1 - \Gamma_{21}\Gamma_{23}e^{\left(\frac{-2\gamma_2 d_2}{\cos\theta_2}\right)}} \quad (2.65)$$

$$\vec{E}_1^{\leftarrow} = \vec{E}_1 \left(\Gamma_{12} + \frac{\tau_{21}\tau_{12}\Gamma_{23}e^{-2\gamma_2 l_2}e^{j\beta_1 l_1}}{1 - \Gamma_{21}\Gamma_{23}e^{-2\gamma_2 l_2}e^{j\beta_1 l_1}} \right) \quad (2.66)$$

where the extra path length due to the oblique path through material 2 is

$$l_2 = \frac{d_2}{\cos\theta_2} \quad (2.67)$$

and the reduction in path length due to each reflection emanating from the wavefront between medium 1 and 2 earlier than the first wavefront is:

$$l_1 = 2d_2 \tan\theta_2 \sin\theta_1 \quad (2.68)$$

The reflection and transmission coefficients defined earlier can now be used to compute propagation at the interface.

2.4.5 Wave Diffraction Through Apertures

Structures which contain discontinuities such as apertures may allow the transfer of electromagnetic energy not only through diffusion, but also through direct aperture penetration (figure 2.17). In this section we will only consider simpler aperture structures such as perforated metal sheets or metal meshes, as this provides good insight before moving towards the complexity contained within nonwovens. Nonwoven materials may suffer from such penetration effects at high enough frequency, via the presence of normal electric and tangential magnetic fields. These fields manifest as a mutual capacitance or inductance which may reduce the materials shielding effectiveness, making a theory of diffraction through apertures necessary.

2.4 Reflection and Transmission of EM Waves

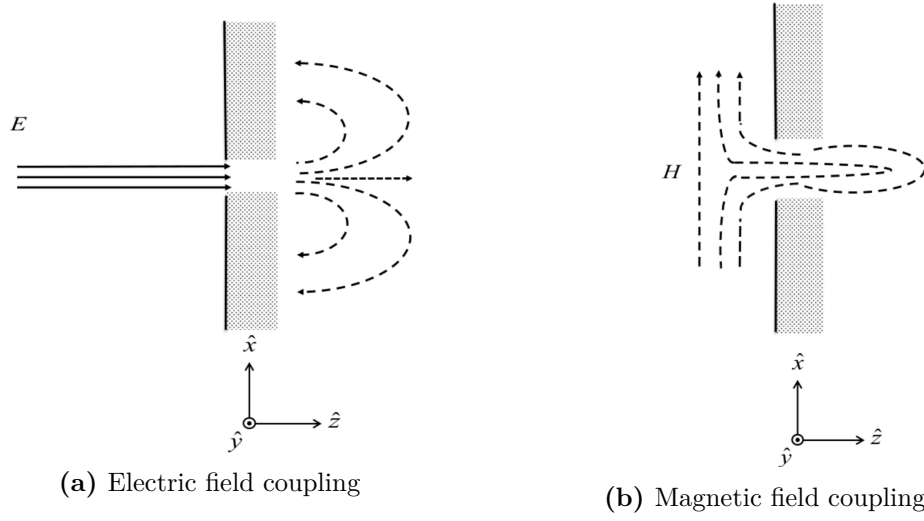


Fig. 2.17 A schematic representing penetration effects of electric and magnetic fields when an aperture is present

It could be argued that Thomas Young first began experimenting with the interactions of electromagnetic waves and apertures in 1803, with the famous double slit interferometer experiment. Augustin Fresnel built on Young's work and in 1817 proposed a radiation model from apertures as derived by Christiaan Huygens. Gustav Kirchhoff's integral theorem (1883) then allowed for the modelling of propagation through sub-wavelength apertures.

It wasn't until 1944 when Hans Bethe's theory of diffraction by small holes [17], enabled sub-wavelength apertures to be treated theoretically. Bethe's analytic formula was later revised (1954) by Bouwkamp [18] to include higher order terms which improve the accuracy of the expression over the $0.07 < \frac{a}{\lambda} < 0.15$ range, where 'a' is the diameter of the aperture. Experimental methods were successful in quantifying polarizability through non-elliptical apertures - an early example being Cohn's 1952 electrolytic tank method [19]. Later, numerical methods developed by De Meulenaere 1977 [20] as well as Okon 1981 [21] delivered polarizability results for rectangular, square, diamond and cross based apertures. Fabrikant [22] proposed an analytic solution for various shaped polygonal apertures, using an integral representation technique in 1987. In 2002, Garcia de Abajo [23] showed that Bethe's model was applicable for apertures $\leq 0.2\lambda$ using integral equation methods. For the nonwovens in this study (with pore sizes ~ 100 microns, figure 3.6). Bethe-Bouwkamp's method represents validity up to 1000 GHz. For example at 10 GHz ($\lambda = 3$ cm) the aperture size is $< 0.002\lambda$. When the pore size and

Shielding Theory and Modelling Techniques

wavelength are of equivalent sizes the behaviour cannot be addressed effectively by analytic means due to phenomena such as Fabry-Perot resonance [24].

2.4.6 Polarizability: Sub-wavelength aperture theory

The analytical treatment of electromagnetic waves through sub-wavelength apertures was first addressed by Bethe [17]. Bethe postulated that the resultant field could be reconstructed using fictitious equivalent electric and magnetic dipoles (shown in figure 2.18). The dipole is positioned in the same location as the original aperture but the screen is now assumed to be continuous and free of any hole (i.e. the dipole is placed on the screen boundary).

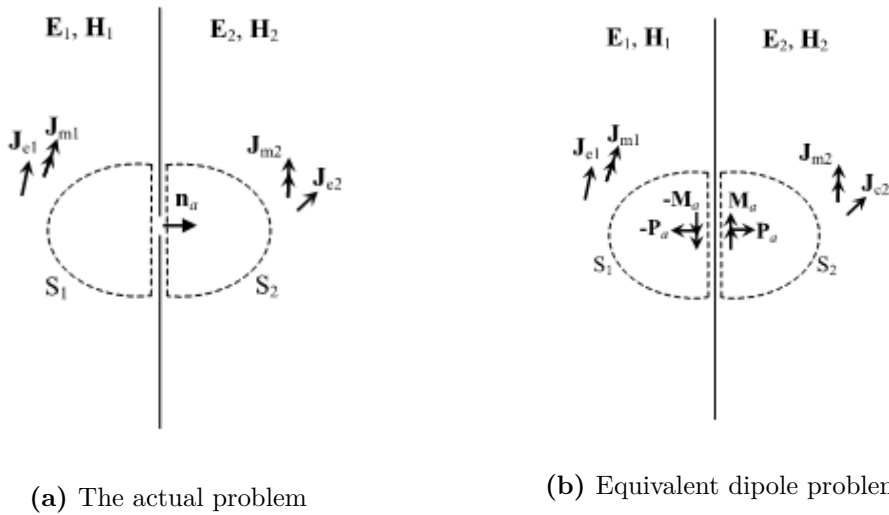


Fig. 2.18 The field diffracted by a small aperture within a conducting screen is equivalent to the superposition of the normal electric and tangential magnetic fields from a radiating dipole [25]

The field strength associated with these dipoles is a function of the vector normal electric field E_n and tangential magnetic field H_t at the aperture location (prior to the opening) and the size/shape of the aperture, parametrized as the Electric and Magnetic polarizability generated by the dipole moments (P) and (M) respectively. For holes of radius a :

$$P = -\frac{2}{3}a^3 E_n \quad (2.69a)$$

2.4 Reflection and Transmission of EM Waves

$$M = -\frac{4}{3\pi}a^3H_t \quad (2.69b)$$

Where:

P is perpendicular to the aperture (\hat{z}) such that $\hat{P} = p_z\hat{z}$.

M is parallel to the plane of the aperture $\hat{M} = m_x\hat{x} + m_y\hat{y}$.

E_n is the vector normal electric field.

H_t is the tangential magnetic field.

2.4.7 Transfer Impedance

Cables

The transfer impedance concept originated in the 1930's and was developed by Vance [26] as a means to calculate the shielding effectiveness of braided cables containing apertures. It is a relevant topic because it is one of the first examples of a conductive structure with apertures in which the conductors pass through the thickness of the structure. A short description of the concept in braided cables is given here before applying it towards planar aperture containing sheets.

The transfer impedance Z_T can be defined as the voltage induced on the inner portion of a cable braid, due to the current flowing on the outside:

$$Z_t = \frac{V}{I_s L} \quad (2.70)$$

Where V is the voltage of the inner conductor, I_s is the shield current and L is the coupled length. At low frequencies the transfer impedance is dominated by the shield's resistance R_0 , but as frequencies increase, a mutual inductance arises from porpoising effects in the aperture of the shield.

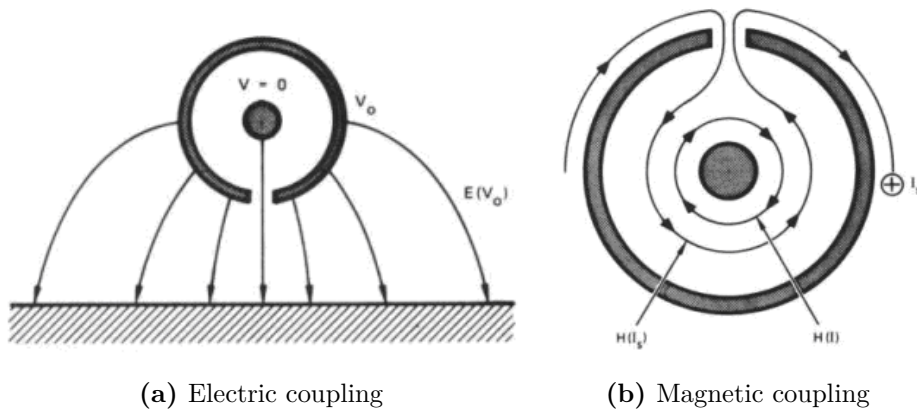


Fig. 2.19 Coupling mechanisms in cable braids [26]

The transfer impedance concept describes field penetration into a perforated shield via two main mechanisms:

1. Diffusion: through the metal itself

2.4 Reflection and Transmission of EM Waves

2. Magnetic coupling: through braid apertures, expressed as a mutual inductance (figure 2.19b)

$$M_{12} = v \frac{\mu m}{4\pi^2 a^2} \quad (2.71)$$

Where μ is the magnetic permeability of the internal insulation, m is the magnetic polarizability of the apertures and v is the number of apertures per unit length of the shield. These mechanisms can be related to the transfer impedance of the braided cable by:

$$Z_t = R_0 \frac{\gamma d}{\sinh(\gamma d)} + j\omega M_{12} \quad (2.72)$$

where R_0 = per unit length resistance of the braid, $\gamma = \frac{(1+j)}{\delta}$ = propagation constant inside the metal comprising the sheath, δ = skin depth of the braid, and d = cable wall thickness.

In addition to the transfer impedance arising from magnetic coupling, there is also a transfer admittance which arises from electric coupling through the braid apertures which is the susceptance per meter between the inner conductor and shield return path (figure 2.19a).

$$Y_t = \frac{1}{V_0} \frac{\partial I}{\partial Z} = j\omega C_{12} \quad (2.73)$$

Where V_0 is the voltage between the central conductor and external shield, $\frac{\partial I}{\partial Z}$ is the current per unit length flowing into the central conductor from the external shield. C_{12} is the mutual capacitance between the conductor and shield, also defined as:

$$C_{12} = v \frac{p C_1 C_2}{4\pi^2 a^2 \epsilon} \quad (2.74)$$

Where a is the shield radius, v is the number of apertures per unit length of shield, ϵ is the electric permittivity of the internal insulation and p is the electric polarizability of the apertures.

However in most of the literature reporting on cable braids, the transfer admittance is usually neglected as most problems assume an incident plane wave with no

Shielding Theory and Modelling Techniques

normal electric component, yielding the transfer impedance as the dominant parameter. This is also assumed to be the case for planar materials in this thesis.

Sheet Impedance

Building on the transfer impedance of cables, the sheet impedance of apertured planar structures, such as wire mesh can be introduced [27]. An example of a wire mesh structure is shown in figure 2.20.

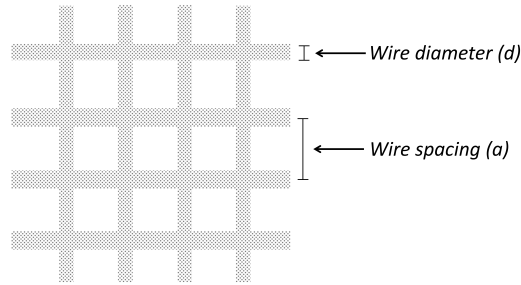


Fig. 2.20 A wire mesh geometry with wire diameter 'd' and spacing 'a'

Such a wire mesh, if planar in nature and electrically thin, can be characterised by a sheet impedance Z_s :

$$Z_s = R_s + j\omega M_s \quad (2.75a)$$

$$R_s = \frac{4a}{(\pi\sigma d^2)} \quad (2.75b)$$

$$M_s = \frac{\mu_0 a}{2\pi} \ln\left(\frac{1}{1 - e^{-\pi d/a}}\right) \quad (2.75c)$$

Where R_s is the sheet resistance, M_s is the sheet inductance, a wire spacing, d is the wire diameter and σ is the wire conductivity. By experimenting with different values of a , it is possible to calculate the impact on the shielding effectiveness. Figure 2.21 shows the decrease in shielding effectiveness as the frequency increases, due to the penetrating field from the openings in the wire. Larger openings allow lower frequencies to penetrate, reducing the shielding effectiveness.

2.4 Reflection and Transmission of EM Waves

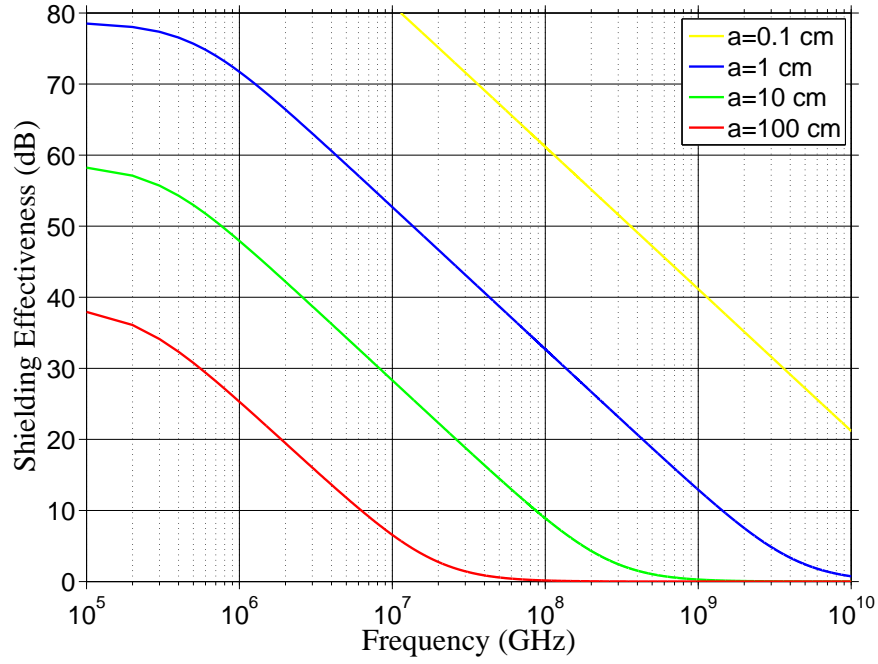


Fig. 2.21 Examples of copper wire meshes with a filament diameter 100μm at different spacing 'a'

In these models, a normally incident plane wave is assumed, allowing the surface impedance to be related to the shielding effectiveness [28] via:

$$SE = 20 \log \left(\left| 1 + \frac{\eta_0}{2Z_s} \right| \right) \quad (2.76)$$

where η_0 is the impedance of free space.

2.5 Aperture Modelling Techniques

A central problem to the modelling of nonwoven fabrics is their complex array of apertures, resembling different sizes and shapes of polygon. When faced with a challenging problem, it is wise to simplify it as far as possible and then add layers of complexity. Initially uniform and periodic apertures in homogeneous materials are introduced allowing the key physical principles and modelling techniques to be demonstrated. A means of modelling more complicated cases directly relating to nonwoven fabrics is reserved for the later chapters.

2.5.1 Analytic Models of Apertures (Perforated Brass Sheet)

In this section models of a real perforated brass sheet sample are introduced ¹ - which can be considered a simple periodic apertured structure. This sheet is shown in figure 2.22 and consists of a square array of circular apertures, 3mm in diameter and 10mm pitch, with a sheet thickness of 0.3mm.

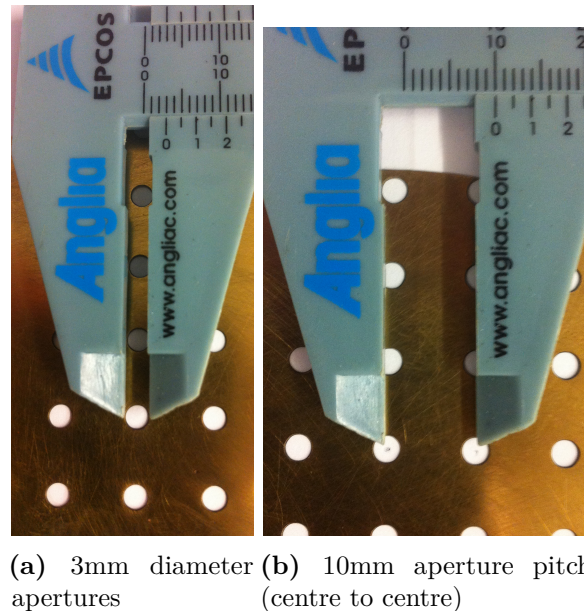


Fig. 2.22 A 0.3mm perforated brass reference sample

¹This material also happens to be used as a reference sample within a measurement method defined in section 4.3.1.

2.5 Aperture Modelling Techniques

Equation 2.77 is an analytic model of the perforated brass sheet which combines the transfer impedance and polarizability theories in order to calculate the shielding effectiveness of a circular aperture containing sheet [29].

$$\frac{1}{SE} = Z_t = R_s \left[\frac{\gamma d}{\sinh(\gamma d)} \right] + j\omega M \quad (2.77a)$$

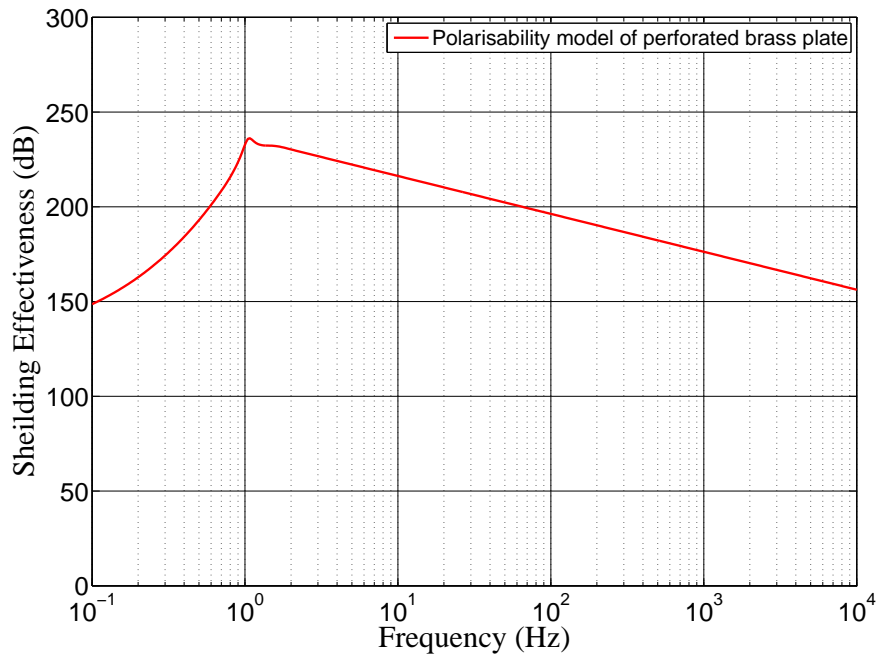
$$M = \frac{\mu_0 \alpha_m}{\Delta x \Delta y} e^{16d/a} \quad (2.77b)$$

$$\alpha_m = \frac{4a^3}{3} \quad (2.77c)$$

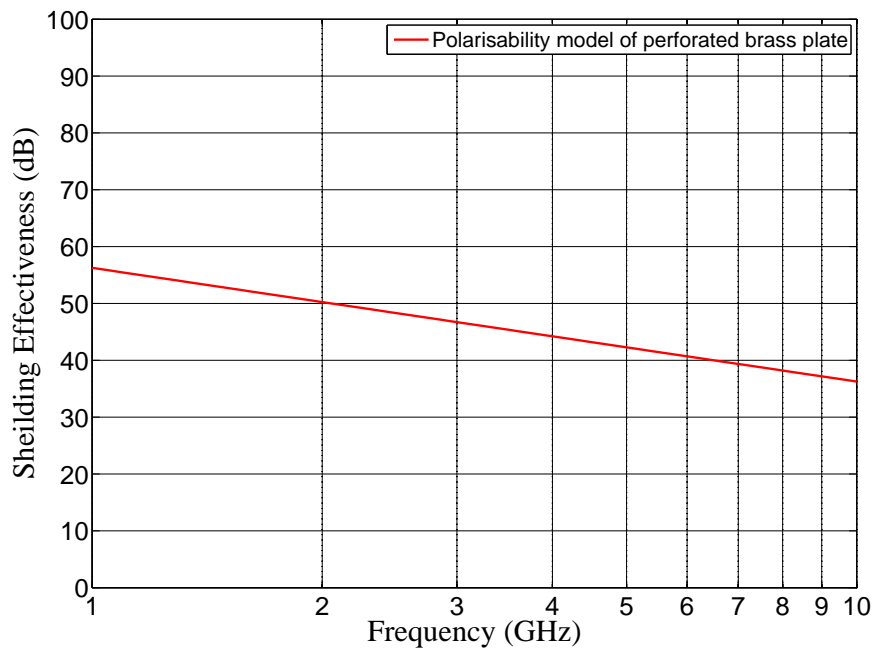
where: the propagation constant inside the perforated sheet is $\gamma = \frac{(1+j)}{\delta}$, δ is the skin depth of the sheet, α_m is the magnetic polarizability of a circular hole, $e^{16d/a}$ a correction term to account for the thickness of the aperture, a the hole radius, d the material thickness, and $\Delta x \Delta y$ the area over which the aperture model is applied.

Figure 2.23a shows the shielding effectiveness behaviour of the perforated brass sheet. The material's thickness and conductivity result in a skin effect dominated behaviour at low frequencies (increasing the shielding effectiveness initially) before the magnetic inductance ($j\omega M$ term) takes over. This effect results in a decreasing shielding effectiveness with frequency (20dB per decade). Figure 2.23b shows the high frequency behaviour of this analytic model which is compared to numeric and experimental results at the end of the chapter (figure 2.30).

Shielding Theory and Modelling Techniques



(a) Low frequency behaviour



(b) High frequency behaviour

Fig. 2.23 An analytic polarizability model of the brass reference plate

2.5 Aperture Modelling Techniques

2.5.2 TLM models of Apertures (Perforated Brass Sheet)

The Transmission Line Matrix (TLM) method is a robust computational electromagnetic modelling (CEM) method, classified as a volume-meshing technique suitable for the simulation of complex geometries [30], often too demanding to be represented by other methods.

The TLM modelling method was first developed by Johns [31] and relies upon the parallels that exist between electromagnetic waves and circuits, as well as the discretisation of Huygen's principle of wave propagation. This full-wave analysis is performed in the time domain (and also frequency domain), whereby the modelling space is discretised using a grid, consisting of nodes which are connected by virtual transmission lines. Such circuit-field equivalence had been expressed earlier by Kron [32], however Johns was the first to formulate a numerical procedure to solve 2D scattering problems. 3D scattering problems were later made possible due to the development of the symmetrical condensed node (SCN)[33]. A single SCN is made from a collection of 12 transmission lines: 6 for each possible direction and 2 for each possible field polarization, shown in figure 2.24.

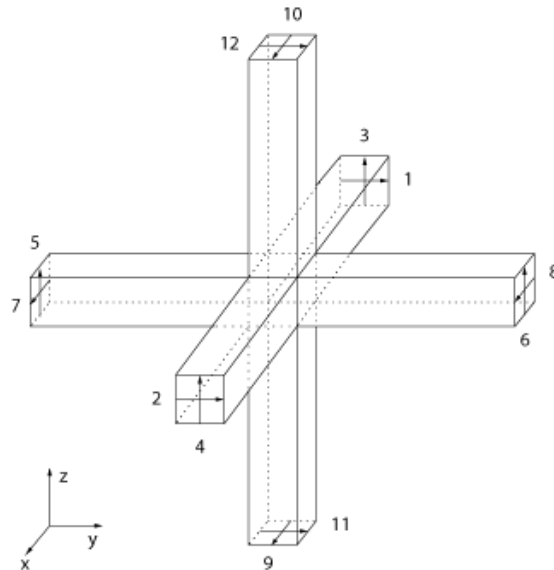


Fig. 2.24 The Symmetrical Condensed Node (SCN), derived by Johns is used to propagate field components through a 3D problem space

For each time step a transmission and reflection coefficient is calculated at each node within the grid and this information is then passed to a neighbouring SCN. In this manner consecutive scattering events are used to propagate the wave through a problem. Computation is divided into two phases: scattering and connection of

Shielding Theory and Modelling Techniques

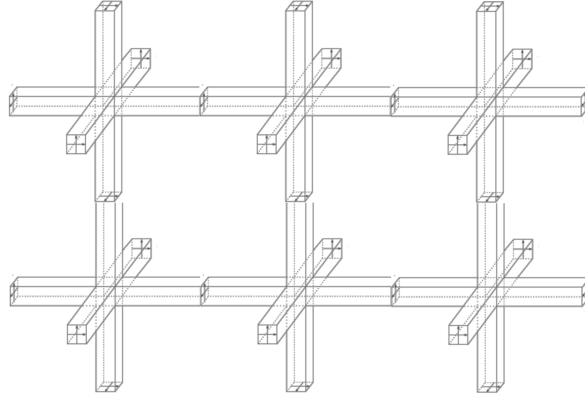


Fig. 2.25 An array of Symmetrical Condensed Nodes

these nodes. As with many of the CEM methods, the finite discretisation of the mesh can lead to numerical dispersion errors when less than 10 nodes/wavelength are used [34]. The disadvantage of using more nodes (mesh cells) is that the total simulation time is increased significantly and so often a compromise must be found.

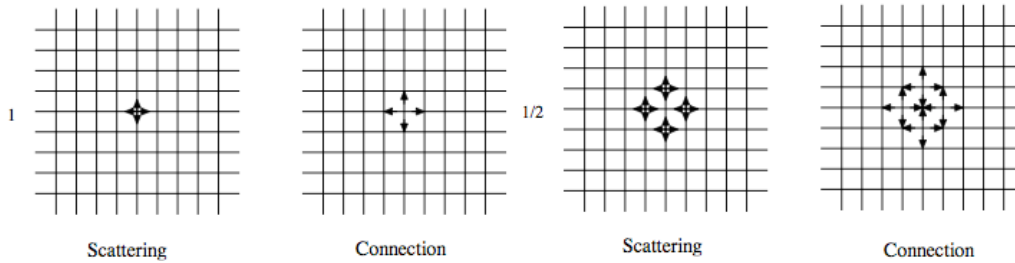


Fig. 2.26 The time evolution of a 2D TLM model [34]

In order to represent materials, different types of series or shunt stub can be added to a particular node [35]. For example, in the case of a dielectric material an open circuit stub is added to increase the effective capacitance of the mesh, a conductive material, a resistive or perfectly matched loss-stub, or in the case of a magnetic material a short circuit stub to increase the effective inductance. In this way the local permittivity, conductivity and permeability can be adjusted in different regions of the grid.

The perforated brass reference sample was modelled using CST Microwave Studio, a 3D Electromagnetic simulation tool inclusive of a user friendly CAD style graphics interface, using the TLM method. TLM was chosen because of the

2.5 Aperture Modelling Techniques

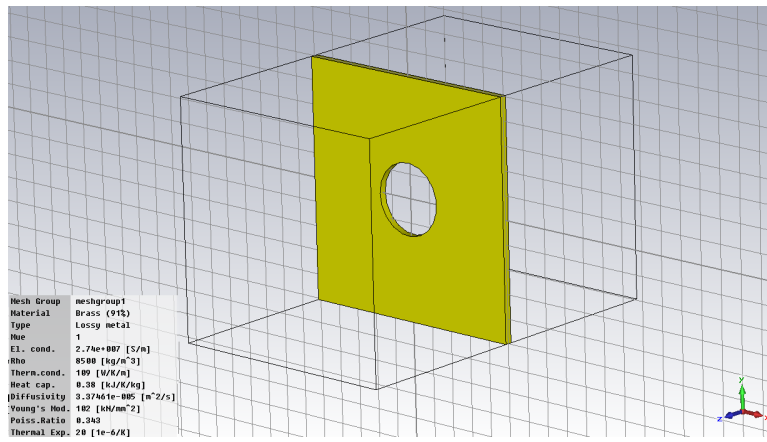
method's suitability in integrating small features into the electromagnetic solution and the fact that the results could be directly compared to the University of York's in house code (Hawk).

Figure 2.27 shows the reference sample in the CST problem space before and after meshing. Initially the measurement units and background materials (free space) must be chosen, before defining the structure properties - which includes the geometry (defined in 2.22), electric conductivity ($\sigma = 2.74 \times 10^7$ S/m) and magnetic permeability $\mu_r = 1$ of the perforated brass sample. An excitation source in the form of waveguide ports (shown in figure 2.27b) is used to transmit electromagnetic energy through the problem. The excitation is a time domain signal, represented by a Gaussian pulse, the width of which corresponds to the frequency range of interest in the problem, 0-20 GHz in this case.

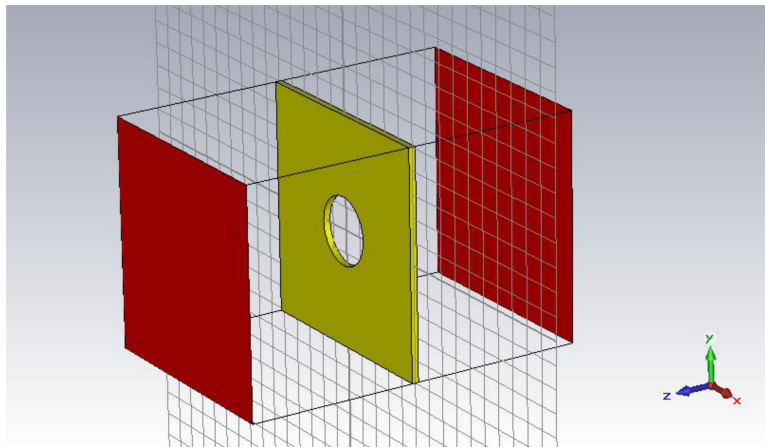
A perfectly matched layer at each end of the problem is used to absorb all energy, once it has passed through the structure, preventing it from interfering with energy in the problem space. A -45dB stopping criterion is shown in figure 2.29, demonstrating the energy being absorbed by the boundary layer. Tangential magnetic ($H_t = 0$) and electric ($E_t = 0$) boundary conditions are used in the ZX and ZY planes, creating perfectly reflecting boundary conditions. Waveguide ports can also be used to determine the scattering parameters of the problem to be determined. Good accuracy of the simulation strongly depends of the mesh type and size. A staircase mesh was used (shown in 2.27c) with 520,000 mesh cells in order to sufficiently represent the structure accurately. This included a depth of 30 mesh cells to represent the samples thickness (in the z-plane). Finally the TLM solver type is chosen and the model is run until a stopping criterion of -80dB reached.

Figure 2.28 was completed using the University of York's 'Hawk' TLM code, and shows a 3 GHz electric field penetrating the aperture at three progressive points in time. As energy encounters the aperture, the wave-front is diffracted and forms a Huygens wavelet. Wavelets from corresponding apertures results in an interference pattern becoming visible.

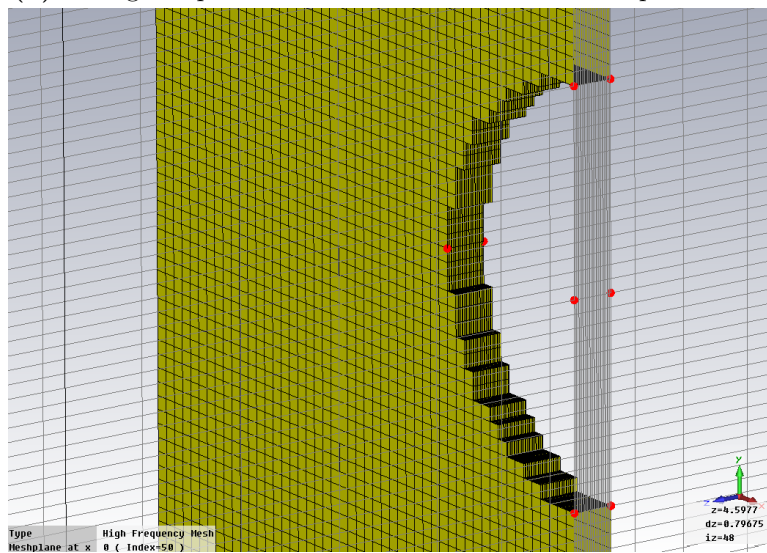
Shielding Theory and Modelling Techniques



(a) 3mm diameter aperture



(b) Waveguide ports used to calculate the relevant S-parameters



(c) The staircase mesh used to discretise the material

Fig. 2.27 A 5x5x0.3mm CST model of a the perforated brass sheet shown in 2.22

2.5 Aperture Modelling Techniques

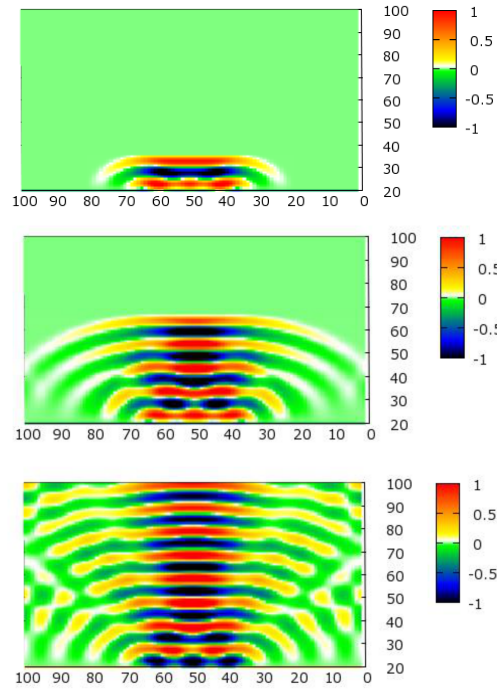


Fig. 2.28 Energy Propagation through the perforated brass sheet at 3 different time steps: 71, 156, 300.

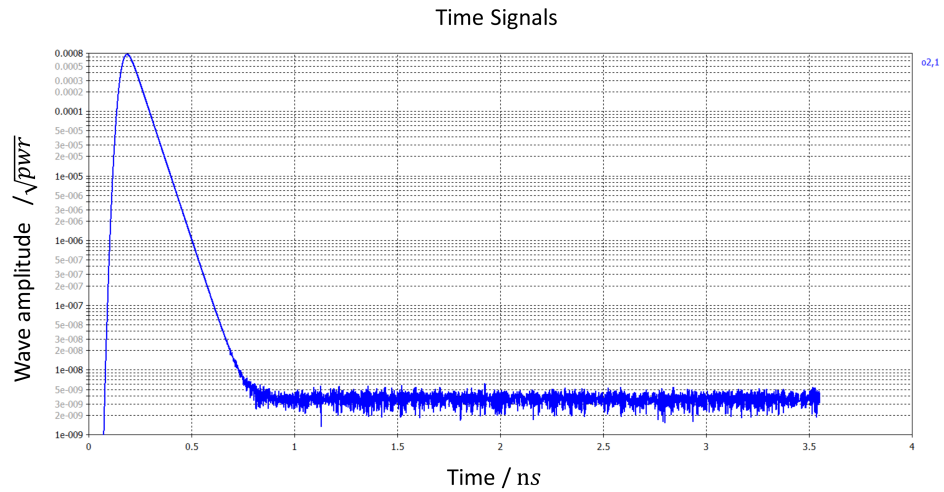


Fig. 2.29 The time response of port 2, showing the gaussian excitation with a -45dB stopping criterion, demonstrating most of the energy has left the mesh

2.5.3 Comparison of Aperture Models

It is interesting to directly compare the results of the two previously defined models and compare them to experimental measurement. In this case the reference sample's Shielding Effectiveness was measured between 1-8.5 GHz using the Nested Reverberation Chamber (NRC) method [36]. This technique makes use of a reflective walled chamber containing a mechanical stirring paddle to create a randomly polarized electric field. A windowed partition enables the shielding effectiveness to be calculated by measuring the power with and without the sample placed across the window.

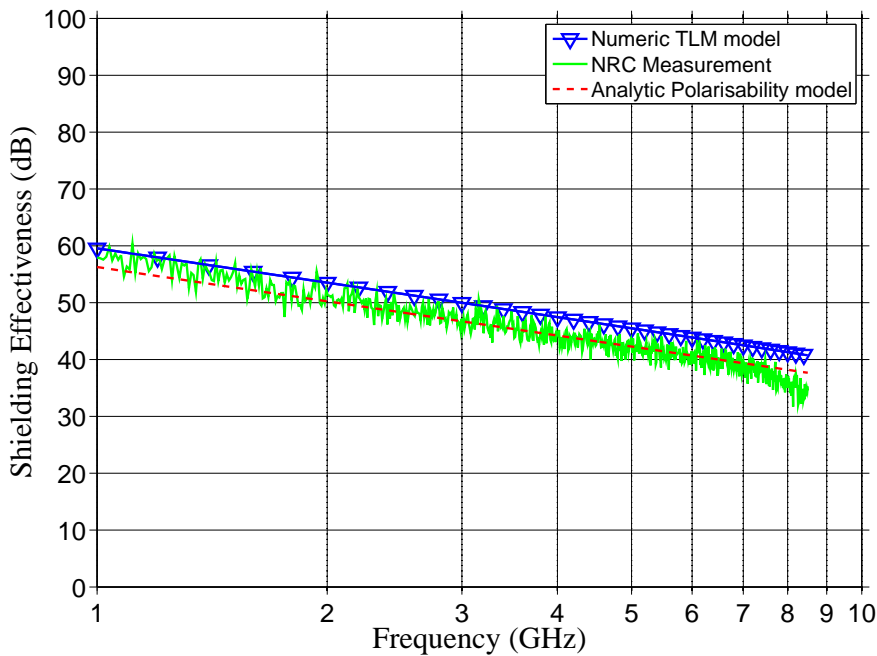


Fig. 2.30 Analytic, numeric and measured shielding effectiveness values of the perforated plate

Figure 2.30 shows reasonable correlation between both modelling and measurement methods, each demonstrating a -20dB per decade fall in the Shielding Effectiveness as more energy couples through the reference plate apertures.

The numeric TLM model is slightly over estimating the shielding effectiveness, which is believed to be caused by the reduction in hole size caused by using a staircase mesh.

2.6 Summary

The aim of this chapter was to introduce the theory required to understand the nature of electromagnetic field interactions with physical media. The shielding effectiveness of planar, homogeneous materials was introduced, using the Schelkunoff model, followed by a detailed discussion of the transmission and reflection mechanics at the various interface within a material. The Schelkunoff model assumes the field is transmitted evenly through a homogeneous shield via diffusion effects alone and is not suitable for more complicated structures which contain apertures. A more appropriate polarizability theory was introduced, which accounts for apertures through the use of fictitious equivalent electric and magnetic dipoles. This theory was used to model the planar shielding effectiveness of a simple aperture containing material - a perforated brass plate. The results of the polarizability theory were then compared directly to experimental measurements and a simulated full wave (TLM) result. In the next chapter, we introduce and examine the materials of interest: wet-laid conductive nonwoven fabrics.

Chapter 3

Nonwoven Materials

Nonwoven Materials

3.1 Overview

This section introduces nonwoven fabrics, their history, manufacture, constituent properties and key physical properties such as; thickness, density, average pore size and micro-structure. Percolation theory of conductive networks is also discussed as well the fundamental electrical conduction mechanisms that occur within the structure.

3.2 Wet-laid Nonwoven Fabrics

3.2.1 Background

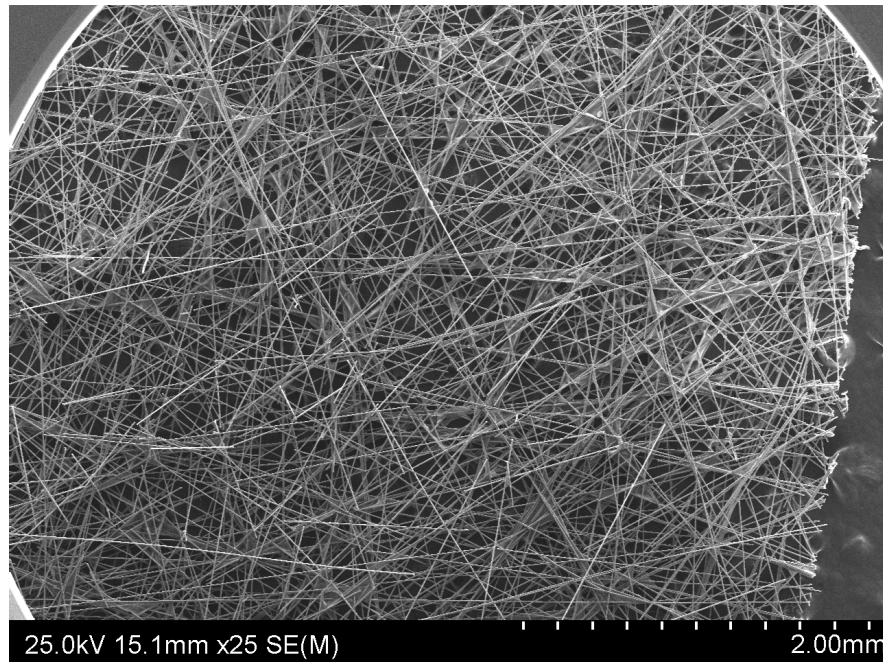
A wet-laid nonwoven fabric is a porous, web-like structure consisting of arrangements of short chopped, man-made fibres that are formed into a flat sheet using a water based process. This results in a flexible, yet dimensionally stable sheet with high surface area and low density. The nonwoven manufacturing process is derived from paper making, in which fibres are first dispersed in water, formed onto a wire screen, drained and dried before being wound onto a reel. However, unlike paper where by the cellulose fibres are held together via hydrogen bonding, nonwoven fabrics containing man-made fibres require the addition of chemical binders for adhesion.

Nonwoven fabrics were originally used within low technology applications such as dust filters, oil filters, thermal/sound insulation, absorbent articles and surgical clothing. Typical fibre types for these applications included polyester (PE), viscose (Rayon), polypropylene (PP), polyethylene terephthalate (PET) and polyamide (PA). More recently advanced nonwoven fabrics have emerged, utilising more sophisticated materials, which has enabled their entry into the composite, aerospace, automotive, defence and energy markets. The choice of fibre and binder type is determined by the requirements of a given application. For example, aramid fibres are used in applications where high abrasion resistance is needed, polyether-ether-ketone (PEEK) thermoplastic fibres used to improve fracture toughness in composite parts and carbon fibres where electrical conductivity is needed. Figure (3.1) shows images of a carbon fibre wet-laid nonwoven fabric.

3.2 Wet-laid Nonwoven Fabrics



(a) A photograph of an A4 sized sample



(b) A scanning electron microscope image (x25 magnification)

Fig. 3.1 Images of carbon fibre nonwoven fabrics

Nonwoven Materials

3.2.2 The Manufacturing Process

The manufacturing of wet-laid nonwoven fabrics is a process that yields stochastic material structures which are determined both by machine settings and random effect (as described by the Brownian motion of turbulent fluids [37]). The process is flexible and can be adapted to accommodate many different man-made fibre types. For example carbon, metallised carbon, aramid, glass, polyester, nylon, silicon carbide and quartz fibre types are possible.

Figure 3.2 shows the key steps within the process. Fibres are first dispersed in chests of water using suitable viscosity modifiers and surfactant systems. Once mixed, the dispersion is pumped along a pipe network to a forming section in which the fibres are filtered onto a porous belt (known as the wire). As fibres are deposited on this belt, they amass to form a loose web which is subsequently bound together using a polymeric binder applied by an overhead coating system. A multi-stage oven evaporates any remaining moisture in the web and cures the binder, stabilising the structure and allowing the material to be wound on to a reel.

Certain process limitations exist, such as fibres that are required to be between 1mm and 25mm in length and have a specific density greater than 1, to ensure effective dispersion is achieved. The fibre web must also possess enough wet tensile strength to support itself as it moves through the process, before the material has entered the drying section.

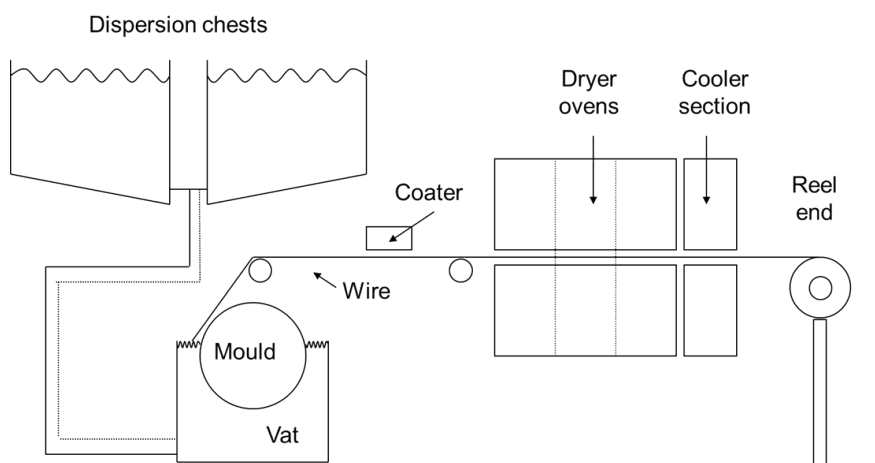


Fig. 3.2 Schematic overview of the nonwoven fabric manufacturing process

3.2 Wet-laid Nonwoven Fabrics



Fig. 3.3 Nonwoven fabric (bottom left) entering the oven section, painted blue

3.3 The Physical Properties of Nonwovens

3.3.1 Constituent Properties

In this study, it is specifically carbon fibre nonwoven fabrics (figure 3.1) which are considered over a range of 4-85 g/m^2 areal weights.

Carbon fibre nonwoven fabrics are constructed from two key components: polyacrylonitrile (PAN) carbon fibre and a liquid based polyethylene terephthalate (PET) binder used to stabilize the structure (tables 3.1 and 3.2 respectively).

Table 3.1 Carbon fibre properties [38]

Carbon Fibre (Toho Tenax-A HT C124)	
Density (ρ_f)	1820 Kg/m^3
Fibre Diameter (d_f)	7 μm
Fibre Length (l_f)	12 mm
Tensile Strength	4275 MPa
Tensile Modulus	225 GPa
Electrical Conductivity (σ_f)	72464 S/m

Table 3.2 Liquid binder properties [39]

Polyester Binder (Hexion WD30)	
Density (ρ_b)	1080 Kg/m^3
Solids (%)	30 %
Glass-Transition Temperature (T_g)	29 $^{\circ}C$
pH	> 5.5
Dispersion Viscosity @ 20rpm	18 Cp

The atomic structure of carbon fibre is very similar to that of graphite - fibres containing at least 92% by weight are defined as carbon, whilst fibres containing at least 99% by weight are known as graphite [40]. Carbon fibre consists of planes of graphene held together by Van der Waals forces at an approximate distance of 0.335nm [41].

In PAN carbon fibre these graphene planes are stacked haphazardly (turbostratic stacking), the exact structure depends heavily on the exact precursors and production methods used. The basic processing steps involve the polymerisation of an acrylonitrile precursor to form polyacronitrile plastic. This plastic is extruded

3.3 The Physical Properties of Nonwovens

through dyes to form fibre filaments, which are stretched and tensioned to align the molecules and control the filament diameter. After a stabilisation step where the fibres are heated in air at around $200 - 300^{\circ}\text{C}$, the fibres go through a carbonisation process ($1000 - 1500^{\circ}\text{C}$) in a nitrogen filled oven. This removes any non-carbon atoms including water, ammonia, hydrogen, nitrogen and yields a tightly interlocked chain of carbon atoms. The fibre tows are finally coated with a water soluble polymer size 3.8 % by weight, improving handling and wind up characteristics on reels.

Within each graphene layer, carbon atoms are arranged into hexagonal patterns with in-plane covalent bonds. A pool of highly mobile de-localised pi-electrons (one per atom) exist above and below the basal plane enabling current to readily move along the structure.

Table 3.3 The deduced masses of carbon fibre and polyester binder in various areal weight nonwoven fabrics

Total Areal weight (g/m^2)	Areal Weight (g/m^2)	
	Carbon Fibre	Polyester Binder
4.4	3.09	1.31
11.1	8.17	2.83
18.2	14.82	3.38
37.6	30.49	7.11
53.5	43.60	9.90
84.1	68.54	15.56

Table 3.3 shows the binder content of each sample, deduced by carrying out a loss on ignition (LOI) test. This destructive method consists of calculating the mass loss of the binder in the sample by heating it to 600°C for a few seconds - leaving only the mass of carbon fibre.

Nonwoven Materials

3.3.2 The Micro-Structure of Nonwoven Sheets

Nonwoven fabrics possess complicated stochastic structures with varying local physical parameters such as thickness, mass and fibre angle. Figure 3.4 shows fibres

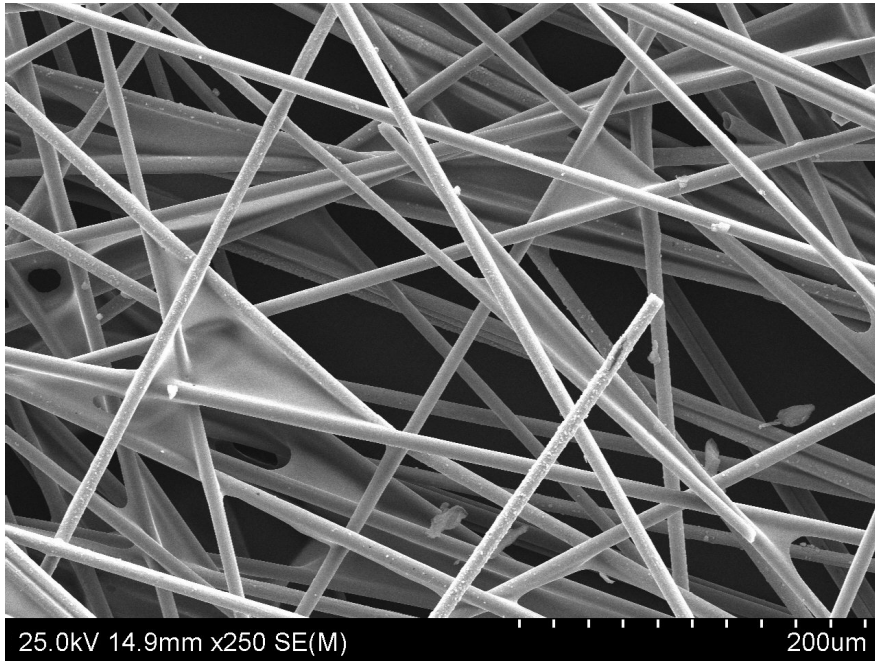


Fig. 3.4 An SEM image demonstrating the micro-structural features of carbon fibre based nonwoven fabrics (x250 magnification)

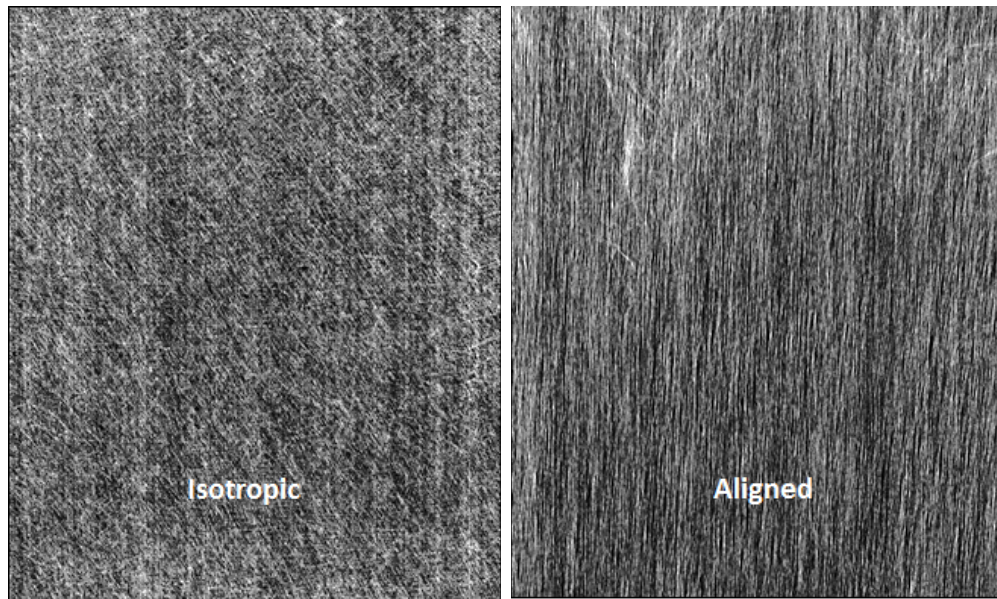
whose principle axes lie within a few degrees of the network plane (azimuthal plane), with a wide distribution of fibre angles running tangential to this plane. Provided these tangential fibre angles are uniformly distributed across the azimuthal plane, the materials can be defined as being perfectly isotropic. In practice, perfect isotropy isn't achievable as there is usually a slight tendency for fibres to be aligned in the manufacturing direction. This means that care must be taken when characterising their properties as at least two measurement orientations should be considered.

3.3.3 Fibre Angle Orientation

By controlling certain manufacturing parameters (details of which are not disclosed), it is possible to influence the fibre angle distribution; anisotropic fibre formations can be achieved, as well as nominally isotropic formations demonstrated in figure 3.5a and 3.5b. The term 'nominally isotropic' is used because the

3.3 The Physical Properties of Nonwovens

manufacturing process always imparts a small amount of orientational bias into the material's structure. Due to this inherent bias certain experimental tests, such as the shielding effectiveness, electrical conductivity and tensile strength have to be repeated in at least two orientations (i.e 0 and 90 degrees with respect to the direction they are formed) in order to characterise the material's properties.



(a) A nominally isotropic fibre angle distribution (b) An aligned fibre angle distribution

Fig. 3.5 A comparison of two fibre angle orientations possible by changing processing parameters

3.3.4 Apertures

As a result of these fibre arrangements, nonwoven fabrics possess a variety of non-periodic, polygonal shaped apertures of different size. Such apertures may be relevant due to the possible polarisability effects described in section 2.4.6 ¹.

Mercury porosimetry intrusion analysis is a method that can be used to determine the average aperture or pore size inclusive to a material, provided the diameter lies between 3.5nm to 500 μ m. Mercury is a non-wetting liquid, with high surface tension which bridges across the opening of small pores and resists penetration caused by capillary action, until an external pressure is applied. The magnitude

¹It is acknowledged that their aperture size versus thickness ratio is different compared to typical meshes or the perforated brass hole plate

Nonwoven Materials

of this pressure is inversely proportional to the pore size. Mercury porosimetry intrusion analysis relies on the gradual intrusion of liquid mercury into the apertures of a structure under controlled applied pressures.

The average aperture diameter D is related to this applied pressure (P) via the Washburn equation² :

$$D = \frac{-4\gamma\cos(\varphi)}{P} \quad (3.1)$$

Where, γ is the surface tension of mercury, φ is the contact angle and P is the applied pressure. A more detailed description of the method can be found by Webb [43].

Work completed using this analysis [44],[45] has indicated that the average aperture size lies between 75 - 91 microns in diameter shown in figure 3.6. It is interesting to note that the average aperture size doesn't change significantly for different areal weight nonwoven fabrics.

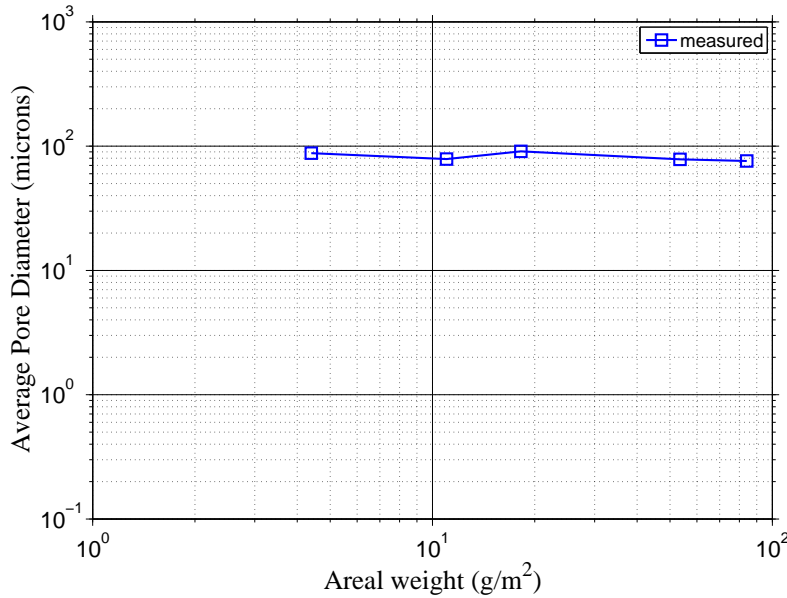


Fig. 3.6 The average aperture size of carbon nonwoven fabrics versus areal weight using mercury intrusion porosimetry analysis (conducted on an Autopore IV 9500 instrument)

²Essentially all mercury porosimetry methods use a theoretic model which conveniently represent these effects using a cylindrical aperture shape assumption [42]

3.3 The Physical Properties of Nonwovens

3.3.5 Density

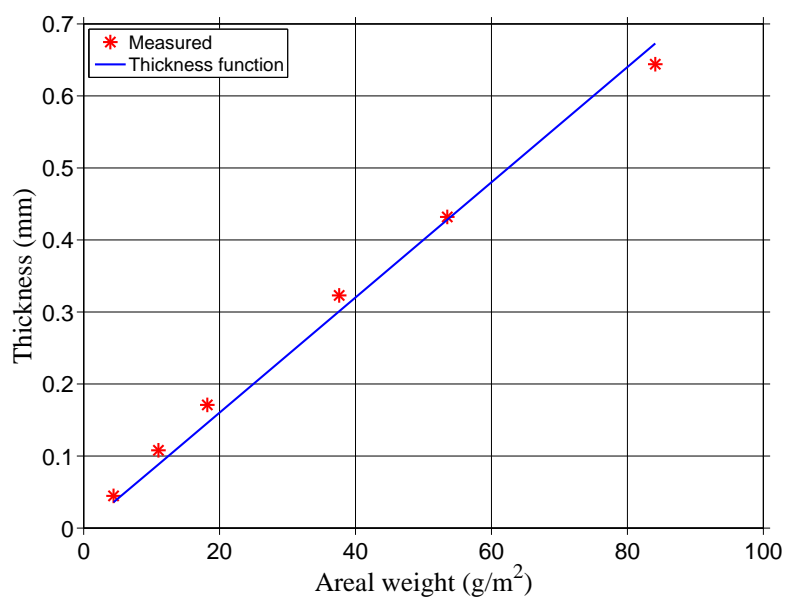
Figure 3.7a shows the measured thickness of 5 different areal weight nonwoven fabrics using a micrometer and an applied pressure of 2 kPa. As the areal weight of the fabric increases, the structure’s density doesn’t change significantly and the thickness is proportional to the areal weight. This is different to many structures such as carbon nanotube networks, which rapidly increase in density with areal weight [46].

Although the density values are relatively constant for real areal weights of material (i.e. those that can be manufactured), it is expected that at very low areal concentrations, the thickness will approach a constant value t_{min} as the fibre diameter is approached. It is therefore useful to define a feasible thickness function such that the possible material behaviour at very low areal densities can be later modelled and studied. The thickness \tilde{t} , defined as the distance between the centres of the outermost fibres, is given by:

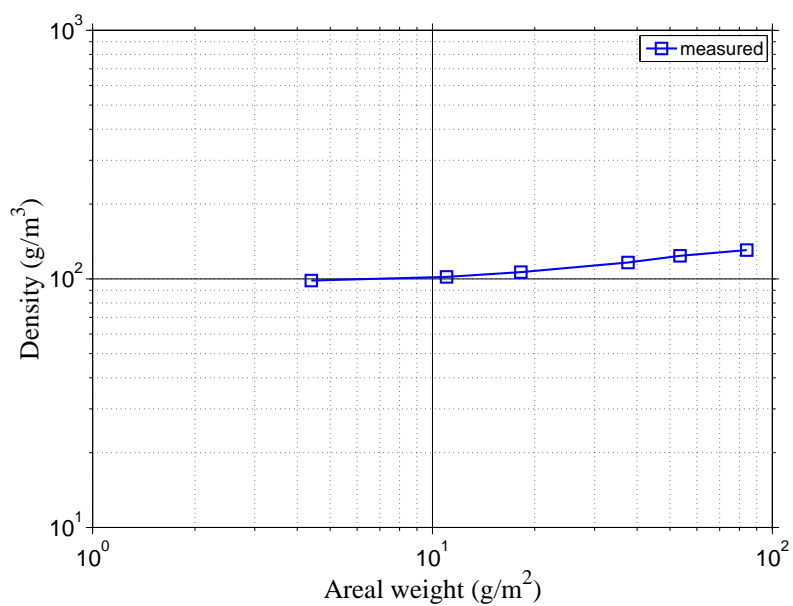
$$\tilde{t} = t_{min} \sqrt[\alpha]{1 + \left(\frac{\rho_A}{\rho_{A0}} \right)^\alpha} \quad (3.2)$$

where $\alpha = 2$ controls the shape of the curve in the transition region, and $\rho_{A0} = 1.05g/m^2$ is the areal density at which the thickness transitions from a constant to proportional behaviour. Figure 3.8 shows this thickness function and comparison to measurement for various areal weight materials.

Nonwoven Materials



(a) Changing thickness versus areal weight



(b) Relatively stable density versus areal weight

Fig. 3.7 The relationship between carbon nonwoven fabric thickness, density and areal weight

3.3 The Physical Properties of Nonwovens

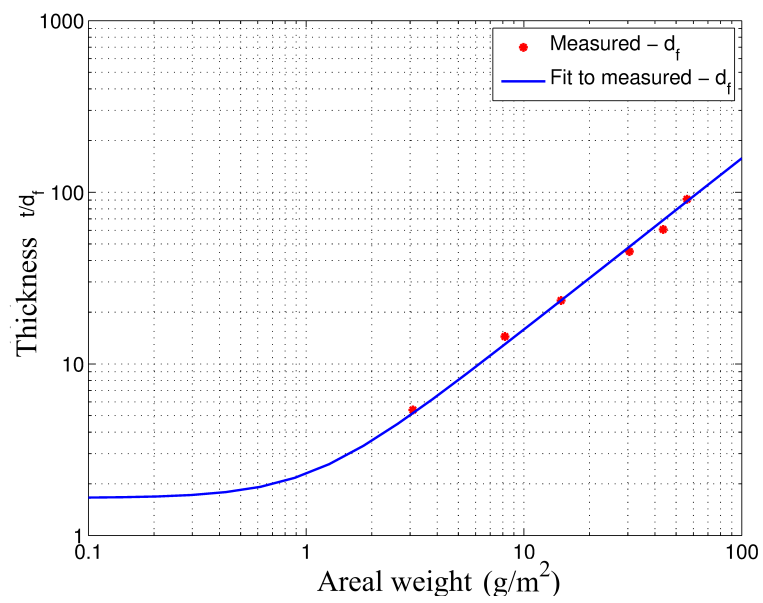


Fig. 3.8 The measured thickness of real nonwoven sheets and a fitted thickness function

3.4 Conduction Mechanisms

3.4.1 Percolation Theory of Conductor Networks

Percolation was a term originally used to describe the behaviour of water flowing through porous rock. Rock structures which have well connected pores allow water to pass readily through them and percolation is achieved. The number of pores and their properties (such as size, location and connectivity) determine how early the onset of percolation can occur. More relevantly to this work, percolation processes are extremely important to the electronic composites industry of today [47], in which electrically conductive fillers (such as carbon nanotubes, copper nanowires, and silver microspheres) are frequently embedded in an insulating matrix in order to improve a system's conductivity [48]. In order to minimise weight, cost and mechanical complications, there is desire to use such fillers at the lowest concentrations possible - underlying the importance of predicting the percolation threshold [49].

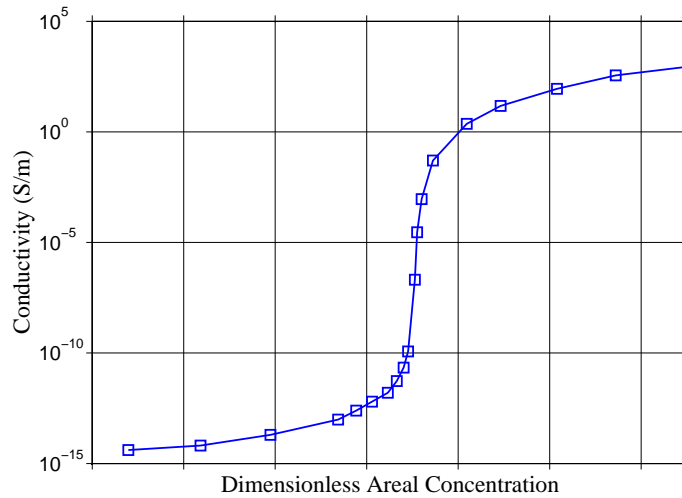


Fig. 3.9 The onset of the electric percolation threshold is marked by the sharp increase in conductivity of a given system with areal concentration.

In a similar way, percolation theory can also be applied towards stick networks, representative of conductive nonwoven fabrics.

Percolation theory predicts there to be an electric phase transition in the bulk conductivity of a system as the number of conductive carriers reaches a critical volume fraction, first discovered by Malliaris and Turner in 1971 [50]. In this case,

3.4 Conduction Mechanisms

the conductive carriers are referred to as sticks due to their high aspect ratio and stick like appearance.

These sticks may exist individually as unconnected members of a network, or collectively as cluster or giant cluster populations depending on the number of connected fibres (figure 3.10). These structures can be defined within a network as a local conductivity, in which current can flow across a limited region of the network. As the concentration of sticks increases, so do the number of available electrical pathways across the network. As the critical concentration of sticks is realised, spanning clusters form, enabling a sharp transition in the material's bulk conductivity, from that of an insulator to that of a conductor (shown in figure 3.11). This transition marks the percolation threshold n_c , which is characterized by the conductivity's power law dependence $\sigma \sim (n - n_c)^t$ where n is the number of fibres and t is the critical conductivity exponent. The percolation threshold corresponds to a percolation probability $< P_x > = 0.5$, and is a function of the number of sticks, stick aspect ratio and the macroscopic orientational anisotropy.

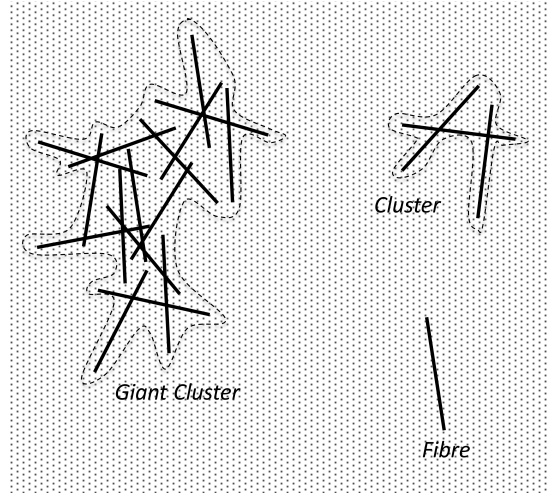


Fig. 3.10 Classifications of fibres, clusters and giant clusters which governs percolation dynamics in stick networks

The sheet conductance of a fibre network is related to the percolation threshold by the equation 3.3, proposed by Zezelj [51]:

$$G_s = a \frac{(n - n_c)^t + c(L/l_f)}{\frac{bn^{t-1}}{G_f} + \frac{(n+n_c)^{t-2}}{G_c}} \quad (3.3)$$

where: n = number of fibres per square fibre length, n_c = percolation threshold, t = critical exponent, G_f = the fibre conductance, G_c = contact conductance, L =

Nonwoven Materials

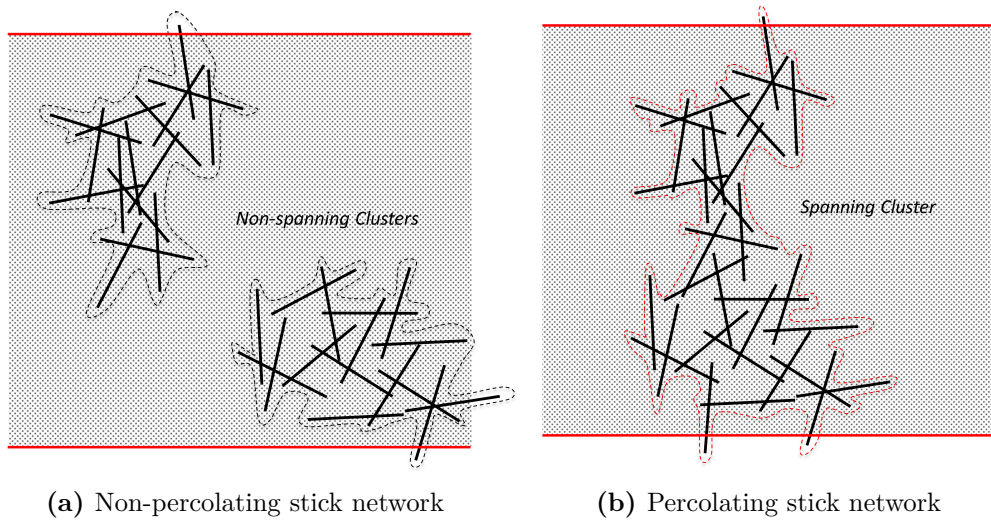


Fig. 3.11 A pictorial representation of percolating and non-percolating stick networks

is the system size, l = the fibre length, $a = 0.027$ and $b = 0.061$ are coefficients determined from least square fitting of the simulated conductance, and $c = 2.5$ is a finite size scaling parameter.

3.4.2 Recent Work

The percolation and conduction of stick networks was first modelled by Pike and Seager [52], who used Monte Carlo approaches to determine the percolation threshold n_c in two-dimensional conducting stick networks. Their stick models consisted of identical, rigid sticks that were randomly distributed and macroscopically isotropic. This work was extended by Balberg and Binenbaum [53] who showed that broader stick length distributions reduced the onset of the percolation threshold and conversely the greater the sample anisotropy, the later the onset of the percolation threshold. Such stick models were also transformed into equivalent circuit models using a resistor network approach by Kirkpatrick [54] in order to calculate the macroscopic electrical conductivity of samples. Such approaches assign a resistor to each stick in the network, apply a fixed voltage across the sample and then solve Kirchhoff's laws to calculate the total sheet conductance. Mutiso [55] used these approaches to also estimate the mean contact resistance between conducting sticks by fitting simulation results to experimental data.

Various methods to lower the percolation conductivity threshold by use of fine material fillers such as carbon nanotubes have also been proposed by Du [56] and

3.4 Conduction Mechanisms

Hu [57]. More recently, Keblinski [58], Li [59] and Zelzelj [51] have reported how the conductivity exponent t is affected by the stick to junction conductance ratio. These methods enable the critical exponent to be obtained and used to model the network conductivity of 2D isotropic stick networks.

In this study, the sheet conductance is dominated by two different scaling behaviours, a non-linear scaling regime close to the percolation threshold and a second high density scaling regime at $10n_c$ and beyond, both of which are reported on. Investigation into the high density regime is considered more relevant because the lowest areal density manufacturable materials have areal concentrations of $\sim 2g/m^2$ and above. An important difference to note, compared to the previous literature to date [60], is that nonwoven fabrics have densities which remain constant (see figure 3.7a) as their areal weight increases, yielding fundamentally different structures.

Also of significance is the work of Heitz in 2011 [46], who produced a theoretical approach to calculating the mean number of contacts per fibre as a function of the areal density for 2D isotropic sheets, as well as the mean contact probability $P_{cont} = 0.2027$ also for 2D isotropic sheets. This work is later developed to produce expressions for the mean number of contacts per fibre in anisotropic 3D systems.

3.4.3 Inter-fibre Contact Resistance

As electrical current flows down a fibre, a portion of electrons are redirected upon reaching an adjoining fibre junction. This junction gives rise to an inter-fibre contact resistance, which (in practise) is different from the fibre resistance. This inter-fibre resistance arises because, on the micro-scale, the fibre surface features are rough and consist of multiple peaks and troughs, limiting the contact area through which current may pass. This reduces the current path interface area, compared to the area of an ideal mechanical contact. If one considers a single fibre-fibre junction, the contact resistance is dependent on the intrinsic fibre resistance and the contact area between the fibres. The contact area between two coalescing bodies is also determined by the respective material's hardness due to elastic surface deformation effects, which are experienced when a load is applied. This work is limited to considering only the mean inter-fibre contact resistance, the reciprocal of which, the mean contact conductance G_c is also referred to.

3.5 Summary

This chapter introduced and defined wet-laid nonwoven fabrics, materials consisting of stochastic ensembles of short chopped carbon fibre held together with a polymer binder. Their key constituent and physical properties were presented, including discussion of their micro-structure, fibre angle distribution, density and thickness. It was noted that nonwoven fabrics have a density that remains constant with increasing areal concentration, fundamentally different to other materials such as carbon nanotube networks. Having been acquainted with nonwoven fabrics, a percolation theory of conductive sticks was put forward in order to describe how a system's conductivity evolves from that of an insulator to that of a conductor, via the formation of fibre clusters which eventually span a region. The contact resistance between fibres was also discussed. The next chapter focuses on the key quasi-static electrical and radio-frequency measurements of the materials introduced in this chapter.

Chapter 4

Experimental Measurements of Nonwoven fabrics

Experimental Measurements of Nonwoven fabrics

4.1 Overview

This chapter presents the key experimental methods used to quantify the electrical properties of nonwoven fabrics, which includes a range of both quasi-static and radio-frequency techniques. The results of each method are presented, compared and discussed. As previously mentioned in section 3.3.3, the nonwoven fabrics in this study are anisotropic which must be reflected by the experimental tests considered to be polarization specific.

4.2 Quasi-static Electrical Measurements

4.2.1 Sheet Conductance Experiments

Nonwoven fabrics can be difficult materials to measure electrically because they possess an uneven structure which is of low density, making electrical termination challenging.

Electrical conductance measurements can be placed into two categories, contact or non-contact based. Contact based methods rely on a direct physical connection between the measurement electrode and sample. This step can in itself, be a source of error, as a variable parasitic resistance between the sample and electrode may exist. As a result, methods have been devised that attempt to minimise this effect - such as by increasing the pressure of the electrode on the sample or by using additional low ohmic contact paste such as indium or silver. However these preparation techniques rarely eradicate the contact resistance entirely and can change the properties of the sample - i.e. by physically compressing the sample or by chemical interaction (i.e.. dissolving of the binder component of the nonwoven). Non-contact based sheet conductance methods avoid these complications as their sensors do not require any physical contact with the sample.

The following four measurement techniques were identified as being possible methods to experimentally determine the sheet conductance:

Vermason 2-wire block: This method uses an electrode block which is positioned on top of the sample and secured with a 1 kg weight to help minimise any contact resistance. The contact resistance between the electrodes and sample was previously determined and subtracted from the final results using the two-terminal

4.2 Quasi-static Electrical Measurements

resistor method described in [61]. The electrode is constructed from two 75 mm long brass strips, separated by a distance of 75 mm, bonded to an insulating polymer block. The electrode is plugged into a multi-meter (Megger M8035) and the resistance obtained. The method is polarization specific and contact based.



Fig. 4.1 The Vermason contact block and multi-meter

Ecopia HMS-300 Van Der Pauw probe [62]: This method is commonly used to measure the sheet resistance of flat samples of arbitrary shape using a four-point probe. Four gold pins, spaced 20 mm apart, are placed on the perimeter of the sample. The gold pins are spring loaded to secure the sample, preventing the need to use bonding wires. A silver paste can be used in the proximity of the pin to improve the contact point into the material further. The method is applied across two orientations to produce the average sheet conductance value and is contact based.

Delcom 873 Eddy current instrument: The instrument uses a high frequency oscillator to generate an alternating magnetic field (3 MHz), inducing circulating eddy currents to flow in the plane of the sample (following the law of induction). In turn, these eddy currents create a secondary magnetic field which is received by a pickup coil, from which the sheet conductance is deduced in a contact-less manner. Eddy current techniques are sensitive to the ambient temperature (a result of the varying resistance of the active coil, which has an effect on the impedance of a series of tuned circuits). Temperature induced zero drift can occur

Experimental Measurements of Nonwoven fabrics

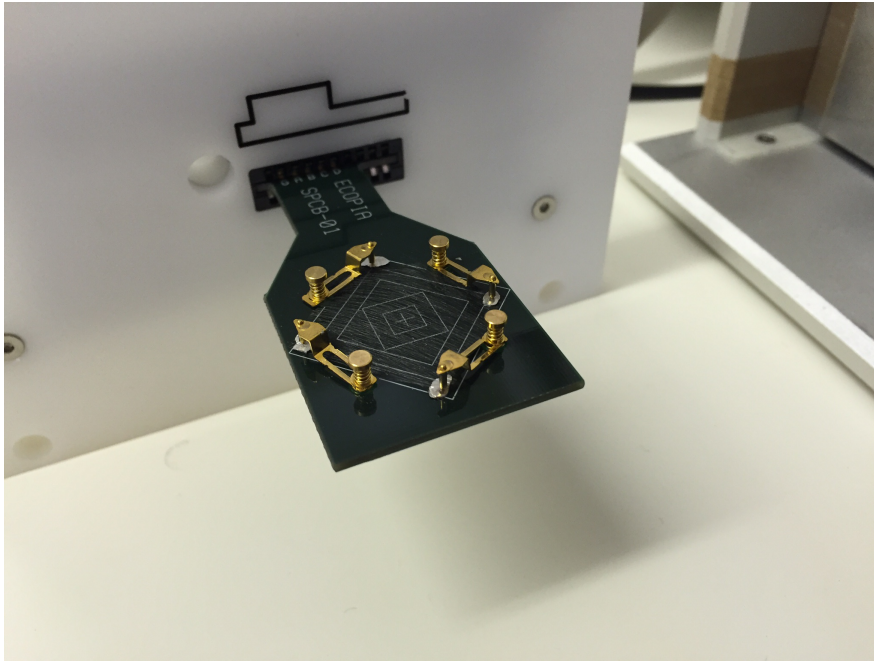


Fig. 4.2 The Ecopia probe which utilises sprung loaded gold electrodes

at a rate $2.3mS/^{\circ}C$ [63] and so use within controlled laboratory conditions is important. The sensor head slot gap is 3mm and has a spatial resolution of 2.5cm. The specific sensor used (20J3) covers a resistance range $0.5 - 10,000 \Omega/sq$. Due to the circular eddy current paths in the material, the method characterises the average sheet conductance of the sample.



(a) Eddy Current meter measurement setup with sample (b) Eddy Current meter sensor head

Fig. 4.3 The Delcom PC873 Eddy Current instrument used to deduce the sheet conductance in a contactless manner

4.2 Quasi-static Electrical Measurements

Curve fitting of Shielding data: It is possible to derive the sheet conductance from the shielding effectiveness measurements (discussed in section 4.3.1). To do this, the Schelkunoff shielding effectiveness expression (equation 2.12) for a homogeneous electrically thin sheet is curve fitted to the complex valued SE data from the Absorber Box method [64], using the Levenberg-Marquardt (LMA) least squares algorithm [65]. Data in the 1 - 2.5 GHz portion of the measurement was selected to do this, as the values in this region are well behaved and the standard deviation is low.

Experimental Measurements of Nonwoven fabrics

4.2.2 Results

Figure 4.4 shows the average sheet conductance of various areal weight carbon fibre nonwovens using the four test methods previously defined. In order to generate average conductance values, each areal weight was sampled 36 times at different measurement positions. Although differences exist, the results largely lie within one standard deviation from one another. The contact based methods indicate a slightly lower conductance at higher areal weights compared to the contactless methods, attributed to the fact that the electrode cannot connect with all of the fibres that exist in the z-plane. The two contactless methods do not suffer from this effect and produce the expected linear relationship between sheet conductance and areal weight throughout the grammage range. In the case of the eddy current method, this is because the 3 MHz magnetic field is able to activate eddy currents throughout the thickness of the sample (skin depth = 10mm). In the case of the derived G_s from curve fitted SE data, the sheet conductance is derived from the S21 parameter which represents the total energy passing through the sample, in which all of the fibres in the thickness of the sample contribute. This improved accuracy means that the contactless experimental methods are a much more suitable way to quantify the sheet resistance for the materials in this study.

Figure 4.5 compares the results of the two contactless sheet conductance techniques - the Eddy current method and the values obtained from the fitted Absorber Box data. The later produces polarization specific values which need to be averaged over x-y directions before they can be compared to the eddy current data. Having done this, good agreement between the measurement methods can be seen. An advantage of the polarization specific SE fitted G_s values, is that the sample anisotropy can be seen by comparing the minimum and maximum y-axis values for each areal weight. It can be seen that all of the samples possess similar levels of anisotropy, with the exception of the $18g/m^2$ sample which displays a greater y-axis difference and is more anisotropic than the other areal weights. This is attributed to change in manufacturing conditions whilst the samples were being prepared.

Figure 4.6 shows sheet conductance variability mapping of various areal weight samples. The high spatial resolution (3cm) of the eddy current probe allows the sheet conductance variability from point to point to be mapped. In this case each

4.2 Quasi-static Electrical Measurements

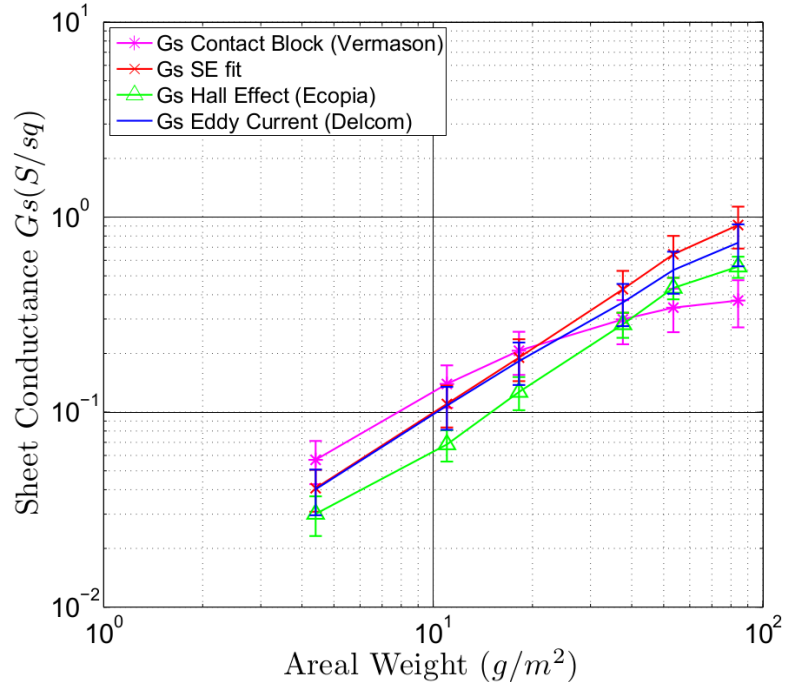


Fig. 4.4 The change in sheet conductance of carbon nonwovens versus areal weight, using four different measurement methods

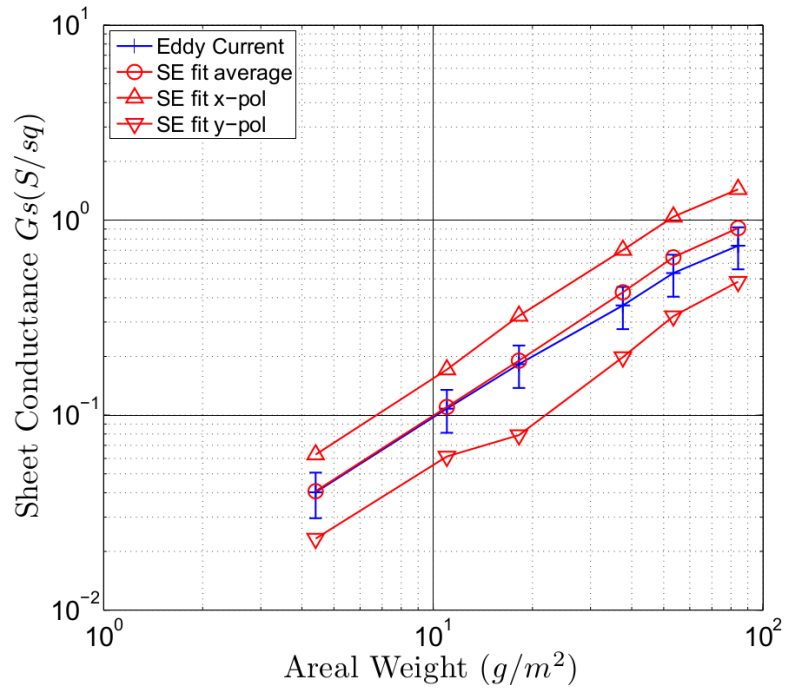


Fig. 4.5 Strong correlation of sheet conductance between two contactless techniques - SE fit and the Eddy current method

Experimental Measurements of Nonwoven fabrics

graphic represents mapping of a 50x50cm sized sample, with a 8cm gap between samples.

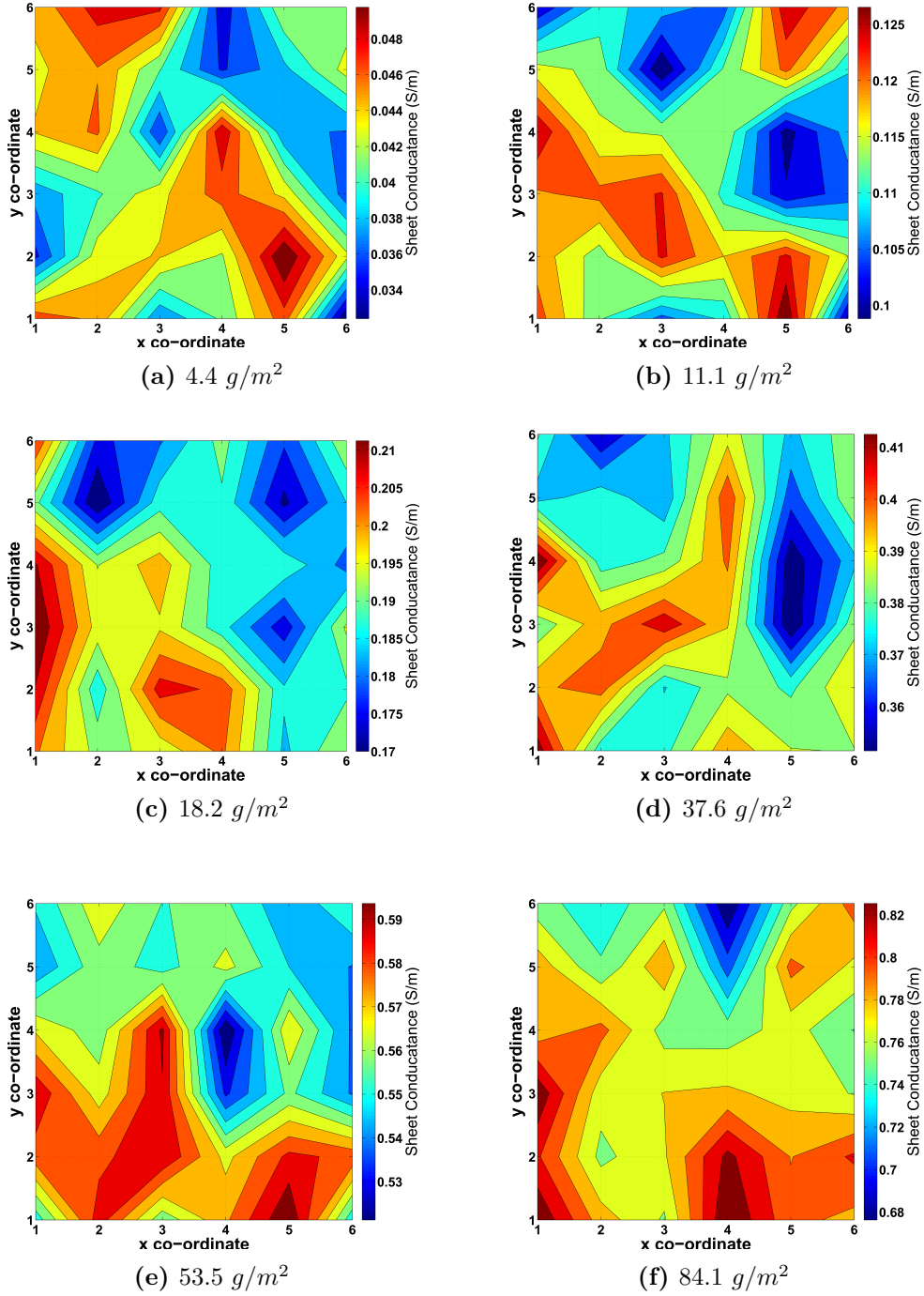


Fig. 4.6 The variability of sheet conductance at different positions across various areal weight carbon nonwoven fabrics

4.3 Radio Frequency Measurements

Many different planar shielding effectiveness measurement techniques exist which accommodate a range of different materials and applications. In this section one specific method, the Absorber Box, is discussed in detail due the fact that its design is the most suitable towards the materials in the study.

4.3.1 Shielding Effectiveness Experiments

The Absorber Box is a shielding effectiveness measurement system, suitable for the characterisation of planar materials between 1 - 8.5 GHz [64]. In particular, the method overcomes surface termination effects by eliminating the need to directly connect with the sample. In many alternate methods (such as ASTM-D4935 [66]), good electrical termination with the sample is required in order to prevent energy from leaking around the sample edge, reducing accuracy. Good termination can be impossible to achieve when the sample has insulating or diffuse surfaces, such as carbon fibre composites or nonwoven fabrics respectively.

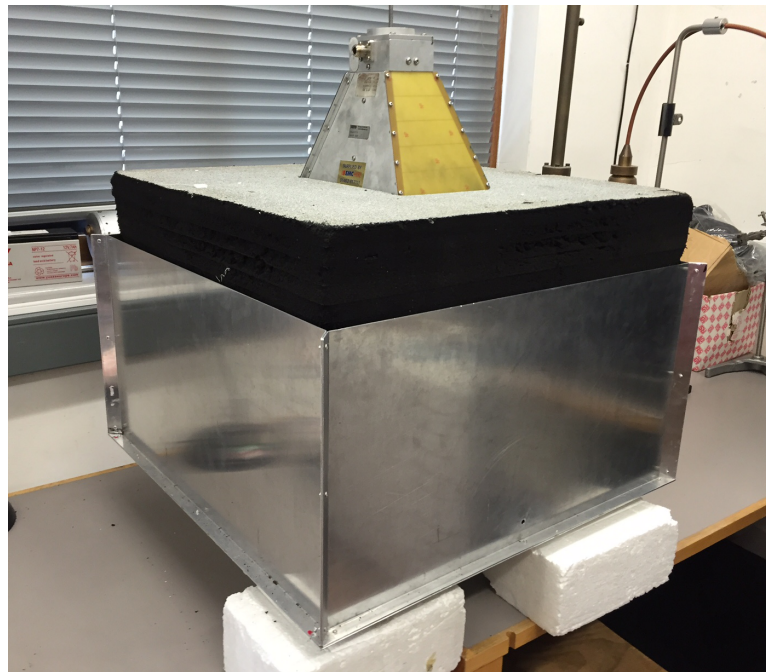
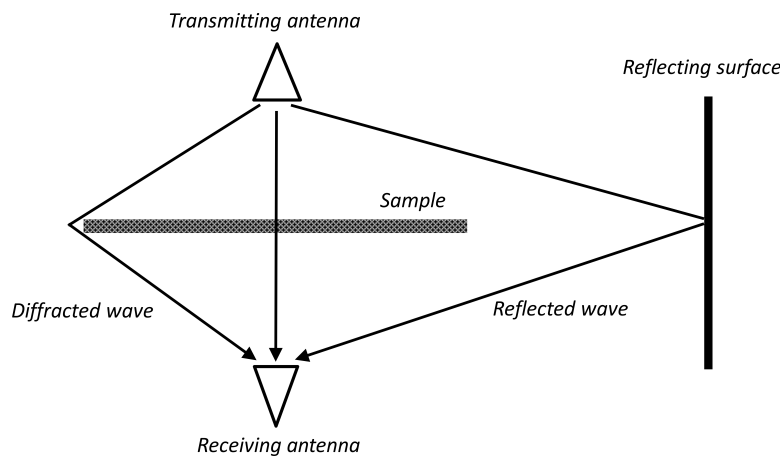


Fig. 4.7 The Absorber Box - a planar material shielding effectiveness measurement system

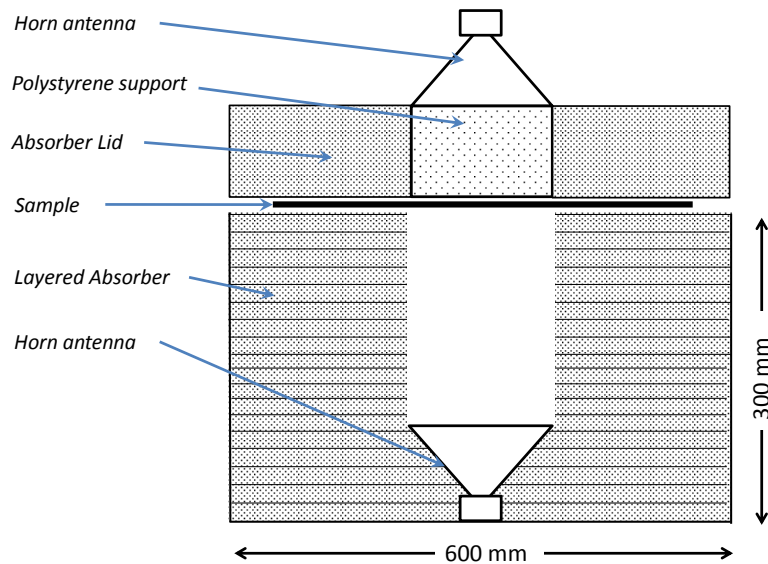
The Absorber Box utilises stacked layers of microwave absorbing foam (Eccosorb LS22 and AN79), which have sufficient loss to attenuate any energy leaking or

Experimental Measurements of Nonwoven fabrics

diffracting around the sample perimeter. The technique has a dynamic range of up to 100dB for samples which are 50x50cm in size. Measurements on anisotropic materials are also possible, limited by the polarization purity and alignment accuracy of the two antennas. Figure 4.8a shows the basic Absorber Box concept and figure 4.8b shows a schematic diagram of the setup.



(a) A ray diagram of the possible wave paths, based on [64]



(b) A schematic of the Absorber Box system

Fig. 4.8 The configuration of the Absorber Box system

4.3 Radio Frequency Measurements

4.3.2 Setup and Equipment

The following network analyser procedure was applied for all S-parameter measurements.

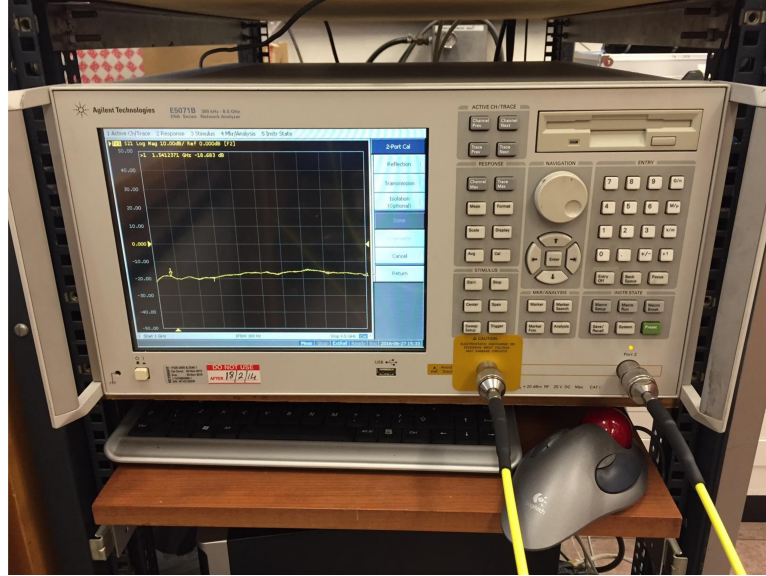


Fig. 4.9 The Agilent Technologies Japan E5071B network analyser

- Connect the two-port network analyser to the desktop computer.
- Switch on the network analyser and allow a 30 minutes warm up period.
- Select a start/stop frequency range 1 GHz : 8.5 GHz.
- Select the intermediate frequency band width (IFBW) to 100 Hz, improving dynamic range.
- Select power: 6dBm (4mW) using the sweep setup menu.
- Choose sampling frequency: 1601 points.
- Calibrate to the ends of both SMA leads using a 85033S calibration kit (open, short, load and through).
- Connect SMA cables to horns using the torque wrench (90 N-cm).
- Run the software package 'Pynadump' to collect S-parameter data.

For each measurement, the sample under test was placed squarely on the last layer of LS22 absorber (shown in figure 4.10d). The Absorber Box lid is then carefully

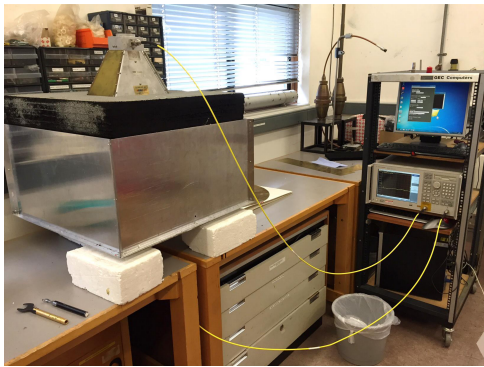
Experimental Measurements of Nonwoven fabrics

placed on the sample and aligned to the lower cavity using the markers on the outside of the box, ensuring the horns are placed in the same position for each measurement. Finally the transmitting horn is placed on top of the Absorber Box lid, directly on the polystyrene support window.

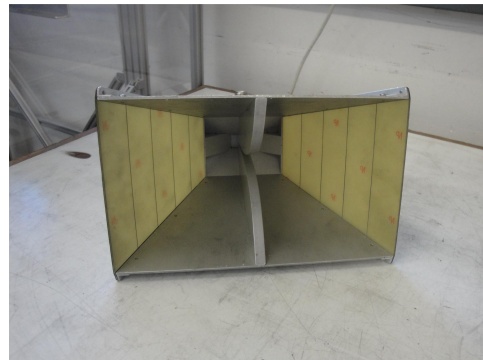
The equipment specification used to complete the measurements was as follows:

Table 4.1 Equipment details

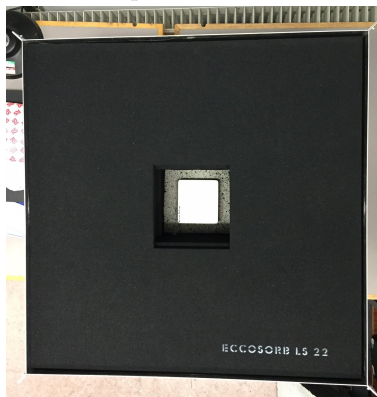
Equipment	Manufacturer	Model info
RF Network Analyser 300 kHz - 8.5 GHz	Agilent Technologies	E5071B
Broadband Horn Antenna 1-18 GHz	Q-par Angus	P/N WBH1-18S
Double Ridged Horn 1-18 GHz	ETS-Lindgren	Model 3115
Eccosorb RF absorbing foam	Emerson & Cuming	LS22, AN79
N-type SMA leads	Teledyne Reynold	-
Absorber Box Cavity	University of York	-



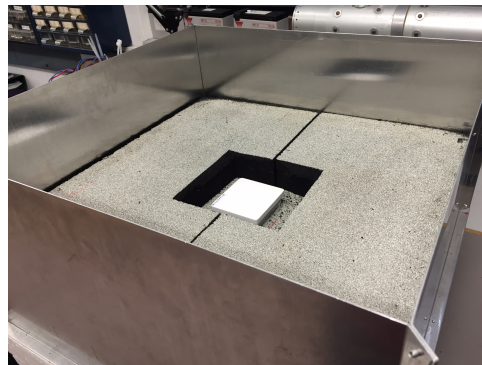
(a) Lid closed with polystyrene spacer and top antenna in position



(b) The ETS double ridged waveguide horn



(c) Plan view with lid open showing the bottom Q-Par Angus horn antenna



(d) LS22 absorbing foam layers removed

Fig. 4.10 Different views of the Absorber Box system

4.3 Radio Frequency Measurements

4.3.3 Absorber Box Calibration

In order to generate absolute measurements, the Absorber Box requires a calibration factor to be applied which is calculated from a reference sample of predetermined shielding effectiveness (SE_{ref}). The sample's shielding effectiveness can be deduced using:

$$SE = SE_{ref} \frac{S_{21,ref}}{S_{21}} \quad (4.1)$$

Where S_{21} is the measured transmission coefficient of the sample of interest and $S_{21,ref}$ is the measured transmission coefficient of the reference sample.

The reference sample is a perforated brass sheet, 300 μm thick, containing a square array of circular apertures, each of which is 3mm in diameter, with a pitch equal to 10mm.

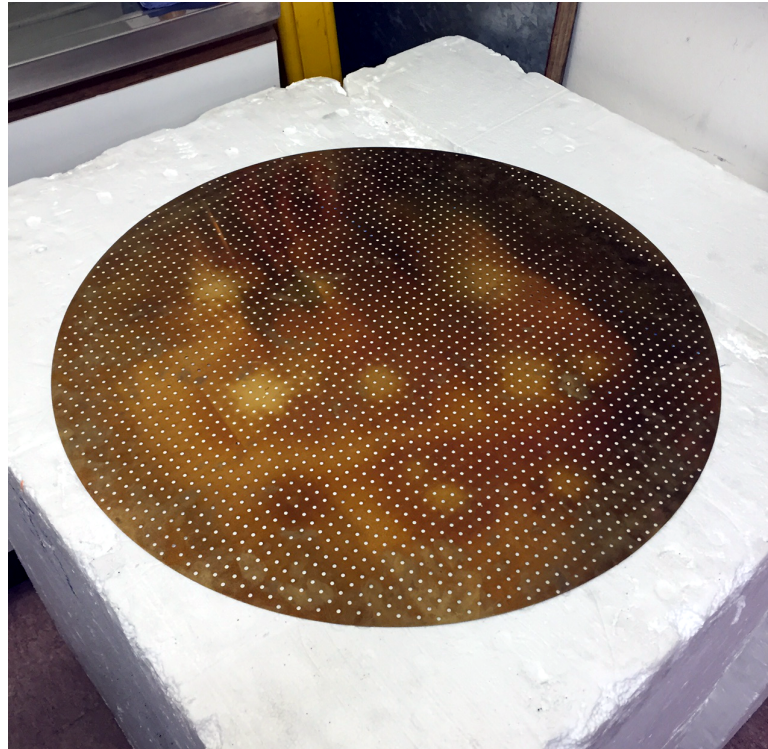


Fig. 4.11 A photograph of the perforated brass plate sample used to calibrate the Absorber Box

The shielding effectiveness of the reference sample has been determined using a variety of methods (shown in figure 2.30) which includes; experimental measurement using a Nested Reverberation Chamber (NRC) and ASTM4935 cell, and

Experimental Measurements of Nonwoven fabrics

various Transmission Line Matrix (TLM) models. The close agreement between the various measurements and models allow the fitted expression below to be used to determine the reference sample's shielding behaviour.

$$SE_{ref}(dB) = 117 - 20\log_{10}f(MHz) \quad (4.2)$$

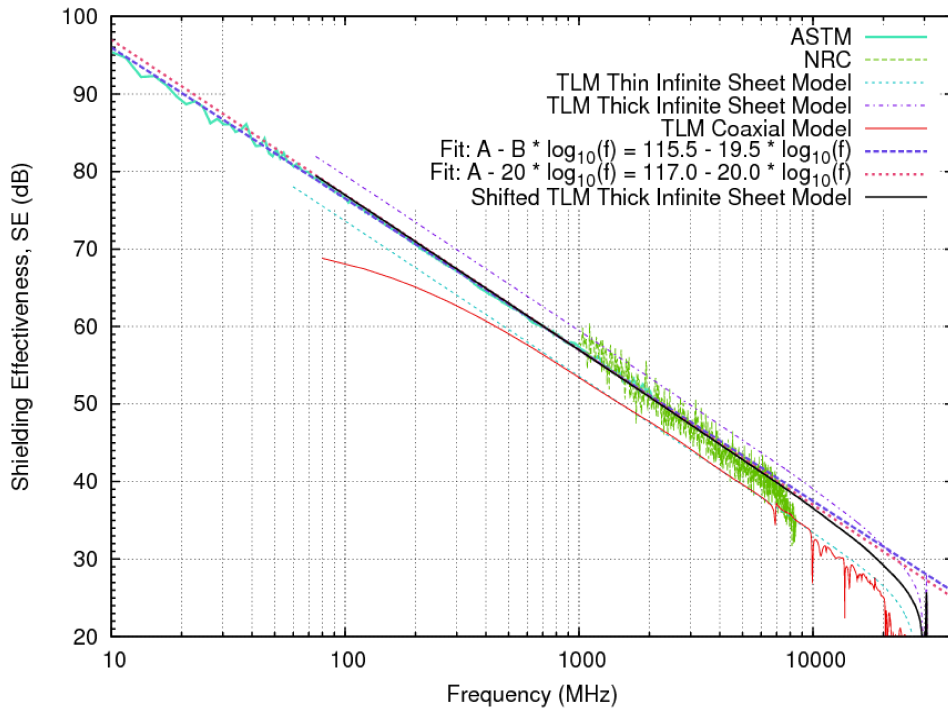


Fig. 4.12 The shielding effectiveness of the perforated brass plate using a variety of measurement and modelling methods, reproduced with permission [67]

4.3.4 Error and Variability

Errors may arise within the Absorber Box measurement if there is any frequency shift in the standing wave pattern inside the Absorber Box cavity. Such a shift can be caused if the sample under test has a significantly different thickness or reflection coefficient compared to the reference sample, resulting in a mismatch ripple being imposed on the obtained data. It has been noted that the polarization of the field in the plane of sample requires further investigation and that a low-pass characteristic reference sample would be advantageous for particular sample types.

4.3 Radio Frequency Measurements

4.3.5 Shielding Effectiveness Results

Figure 4.13 shows the shielding effectiveness of various areal weight carbon nonwoven fabrics completed using the Absorber Box over the 1-8.5 GHz frequency range. Each areal weight nonwoven fabric was characterised 5 times in each polarization resulting in the mean shielding effectiveness, which is plotted with one standard deviation (the shaded region). The graph represents a total number of data points equal to 96,060.

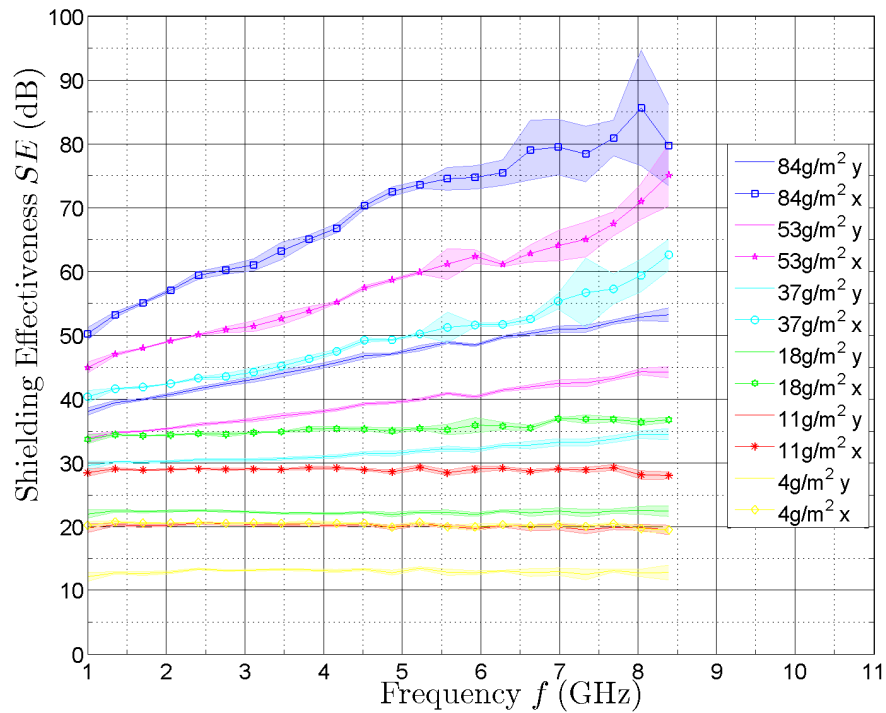


Fig. 4.13 The average shielding effectiveness of carbon fibre nonwoven fabrics, plotted with one standard deviation (shaded region)

The fabric's shielding effectiveness follows a logical order with heavier basis weights providing higher shielding levels. For areal weights $< 18\text{g/m}^2$, the shielding effectiveness remains constant across 1 - 8.5 GHz frequency range, and is proportional to the materials sheet conductance. Materials with areal weights $> 18\text{g/m}^2$ show a shielding effectiveness which increases linearly with frequency due to the dominating effects of the skin effect and thickness. The anisotropic nature of the materials micro-structure is also evident from the divergence in the shielding values for each x-y field polarization. The x-polarization corresponds to an alignment of the field with the materials highest conductivity (i.e. the manufacturing direction). The y-polarization is at right angles to this and corresponds to the material's

Experimental Measurements of Nonwoven fabrics

lowest conductivity (the manufacturing cross direction). At 1 GHz, the sample's anisotropy causes an 8-12 dB difference in the shielding performance, for a given areal weight. As the frequency increases, this difference grows, particularly for heavier areal weights, up to 30 dB in the case of the $84\text{g}/\text{m}^2$ samples.

4.4 Summary

This chapter presented electromagnetic measurements completed on nonwoven fabrics using a variety of experiments to determine the material's sheet resistance and shielding effectiveness. Four different methods were used to characterise the sheet conductance of the nonwoven fabric. It was concluded that contactless methods provided more accurate results as they do not suffer from additional parasitic resistance arising from termination issues with the sample. The strong correlation between the eddy current method and the curve fitted shielding data methods (both contactless) provide confidence in the determined sheet resistance. It was also shown that both the sheet resistance and the shielding effectiveness yield minimum and maximum values depending on the material's orientation relative to the measurement instrument ¹, explained by the anisotropic nature of the material's micro-structure. The maximum sheet conductance and shielding effectiveness occur when the polarisation plane is aligned with the dominant fibre direction, alternatively minimum values are obtained when the polarisation plane is orthonormal to the dominant fibre direction.

In creating accurate models of nonwoven fabrics, these results highlight the importance in quantifying the anisotropy of the material. The next chapter focuses on the development of a new experimental method which is used to determine the material's fibre angle distribution. Amongst other parameters, this information is then used to produce analytic and numeric models.

¹For experiments capable of producing polarisation specific results.

Chapter 5

Modelling Methodology of Nonwoven Fabrics

5.1 Overview

This Chapter focuses on the development of analytic and numerical models used to simulate the nonwoven fabric's electro-conductive behaviour. Before any meaningful simulation can take place, the material's complex and stochastic micro-structure must first be represented. The nonwoven micro-structure is composed of fibres that lie at different in-plane angles, described by a fibre angle distribution. For the nonwoven fabrics in this study, this distribution is non-uniform, meaning that there is a preference for fibres to be orientated in the X-direction over the Y-direction. The X-direction is aligned with the longitudinal aspect of the manufacturing machine and the Y-direction is orthonormal to this in the crosswise direction of the machine. Such effects are immediately observed on the macroscale as was shown in the sheet conductance and shielding effectiveness measurements (discussed in Chapter 4) and important to include within the model such that polarization specific effects are accounted for. The starting point therefore, is to develop a methodology capable of determining the fibre angle distribution for a given sample, which can then be coupled with the key physical data already obtained in Chapter 3 to construct a representative model. Figure 5.1 illustrates the key steps involved in simulating the nonwoven's behaviour, discussed in more detail throughout this Chapter.

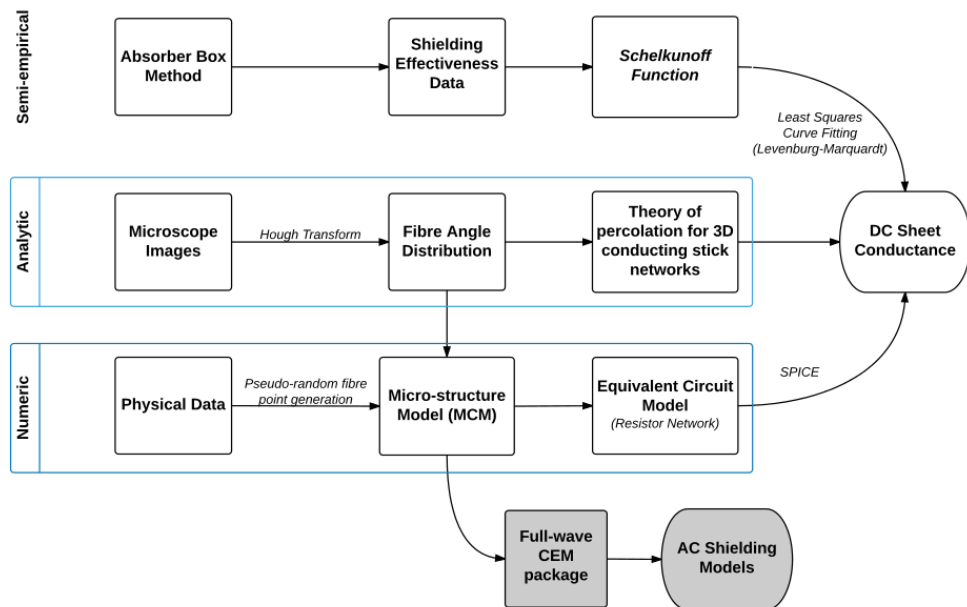


Fig. 5.1 The modelling framework

5.2 Fibre Angle Distribution: Methodology

A new method is proposed and subsequently validated in order to quantify the fibre angle distribution in nonwoven fabrics. This method relies on the data processing of microscope images and the use of a feature extraction method called the Hough transform, in order to generate the probability distribution of fibres over the range of possible angles $-90^\circ \leq \theta \leq 89^\circ$ ¹. The method was applied to microscope images depicting $4g/m^2$ and $10g/m^2$ nonwoven carbon fabrics, where the optical density was low enough to allow fibres to be readily resolved. Testing the method above this areal weight, results in images which quickly become opaque with foreground fibres masking other background fibres, deteriorating the accuracy. It is assumed and subsequently proved that the fibre angle distribution does not change significantly with areal weight by comparing the modelled and measured sheet conductance values.

The following subsections discuss the method and validation process in more detail.

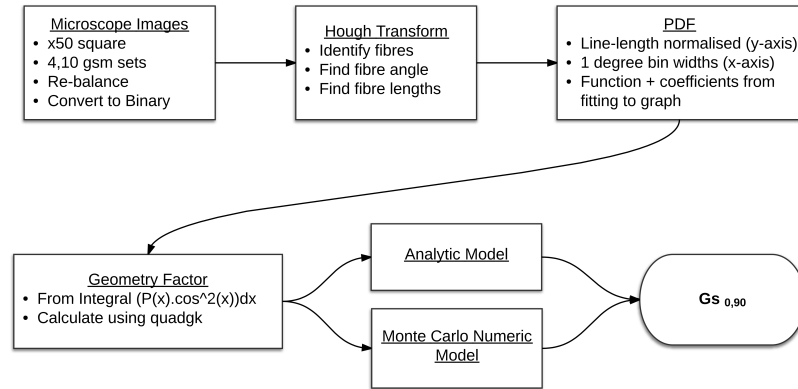


Fig. 5.2 Key processes in calculating fibre angle distribution and polarization dependent sheet resistance

¹A fibre positioned at an angle of -90° and $+90^\circ$ is in the same plane, hence why an asymmetric range is chosen

5.2.1 The Hough Transform

The Hough transform is a feature extraction technique used in image processing to isolate particular lines or curves, first proposed by Duda in 1972 [68]. In this implementation, the Hough function was applied as part of a larger algorithm written to determine the fibre angle distribution, under Matlab within the image processing toolbox. Figure 5.3 depicts the basic fundamentals of the Hough transform function.

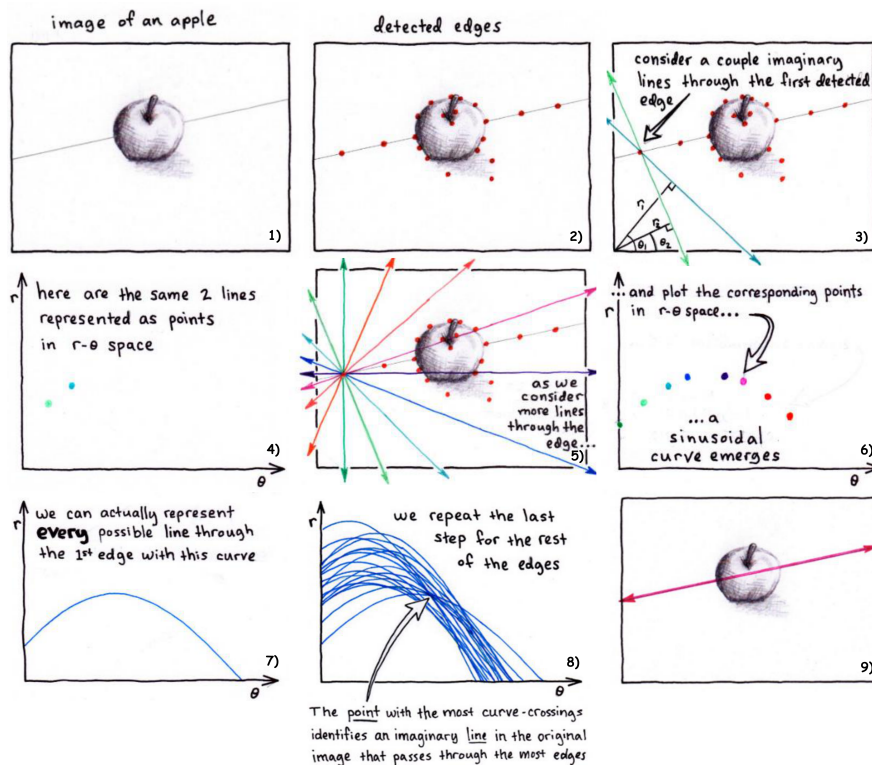


Fig. 5.3 The basic fundamentals of the Hough transform function, reproduced with permission [69]

The Hough transform is based on the identification of line edges in a binary image, determined by two types of pixel: dark which correspond to the image background or light that correspond to part of a line. Pixels that are part of a line, are converted from their parametric Cartesian representation of a line, into polar co-ordinates such that their position is represented by a direction θ and a distance r . Edge pixels mapping to the same co-ordinates in the $r - \theta$ space are assumed to define a line in the image. This is then repeated for all of the remaining lines (edges) in an image.

5.2 Fibre Angle Distribution: Methodology

The Hough function has a range of input parameters including a threshold factor which determines the minimum peak values to be considered (representing potential lines in an image) which determines which data should be recorded or ignored. This is discussed in more detail in section 5.2.5.

Figure 5.4 shows the Hough transform of a microscope image of $4g/m^2$ carbon nonwoven fabric. Figure 5.5c shows a single processed binary microscope image with the lines detected by Hough transform plotted on top of the fibres in the image using the coloured lines.

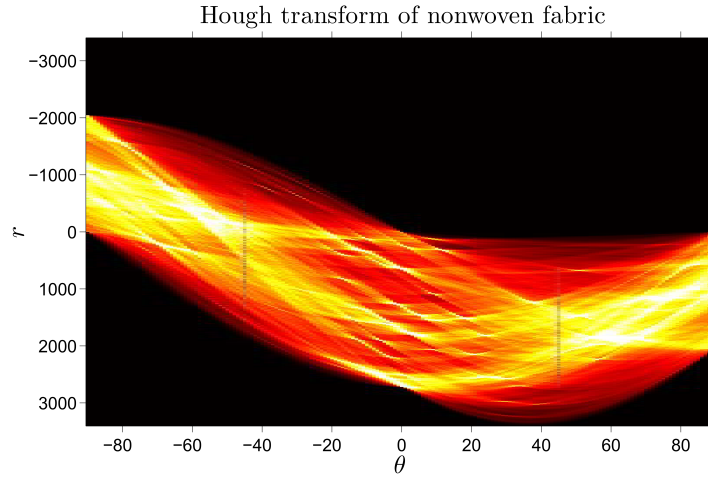
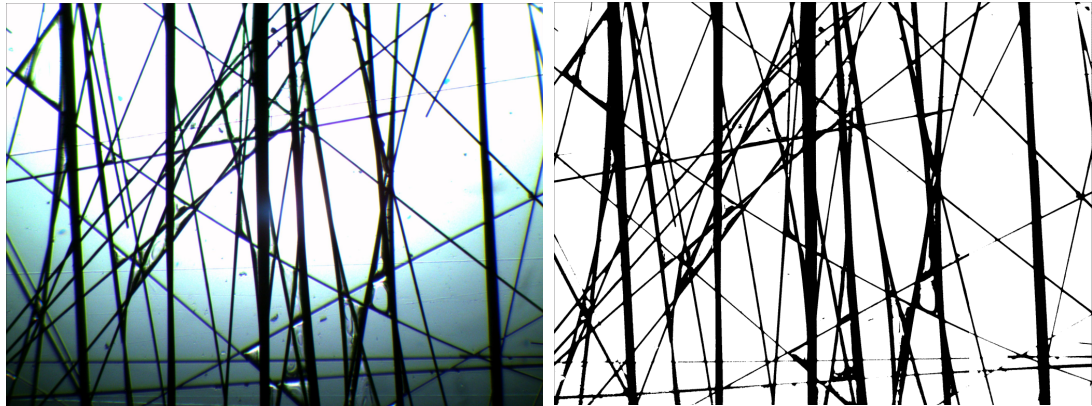
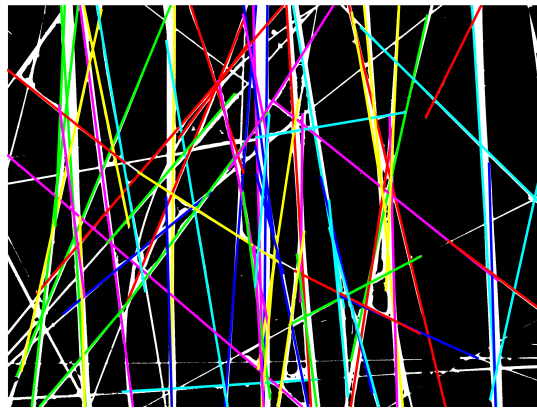


Fig. 5.4 The Hough transform of a nonwoven fabric

Modelling Methodology of Nonwoven Fabrics



(a) A raw microscope image of a $4g/m^2$ carbon fabric (b) A rebalanced, binary microscope image suitable for image processing



(c) The Hough transform recognised fibres (coloured lines)

Fig. 5.5 The image processing and detection of fibres using the Hough transform (each image represents an area of $3.61mm^2$)

5.2 Fibre Angle Distribution: Methodology

5.2.2 Image Processing

To ensure that a representative dataset is collected, 50 images were captured across different positions in the materials plane using a Brunel SP60 microscope shown in figure 5.6 and x5 magnification lens. Each sample was cut to the dimensions $80 \times 230\text{mm}$ using a scalpel and mounted between two glass slides. This compressed the sample slightly, helping to improve the image's focus by reducing the depth of field. It was important to ensure that the sample is cut and mounted squarely on the microscope stage as any misalignment would skew the measurement result. A slide reticule with a grating was used to facilitate the alignment of each sample prior to image capture. The lower illumination bulb and adjustable diaphragm were set to ensure the best image exposure on a sample by sample basis. A typical raw image captured using this method can be seen in figure 5.5a. Further rebalancing and conversion to a binary image (figure 5.5b) was completed in order to remove the vignette and reduce image noise for subsequent processing.



Fig. 5.6 Images of the nonwoven micro-structure were captured using a Brunel SP60 light microscope.

5.2.3 Generation of the Probability Density Function

The data acquired through applying the Hough transform algorithm to all 50 images, allows a probability density of fibre angles to be deduced, which was weighted by line lengths detected rather than the total number of fibres (figure 5.7a). This distribution can be fitted by a Probability Density Function (PDF), which was accurately fitted by the double Gaussian shown in figure 5.7b.

The double Gaussian function, scaled in degrees, is of the form:

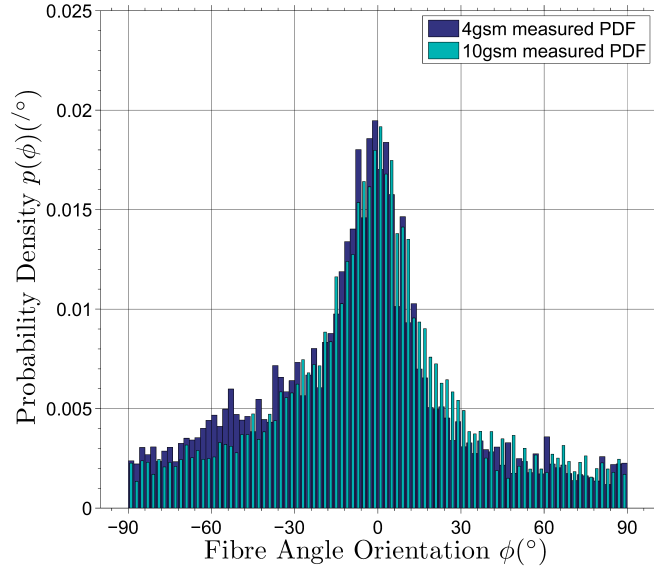
$$p(\phi) = a_1 e^{-[(\phi-b_1)/c_1]^2} + a_2 e^{-[(\phi-b_2)/c_2]^2} \quad (5.1)$$

where the constants ' $a_{1,2}$ ' represent the height of the peak, ' $b_{1,2}$ ' the position of the central peak, and ' $c_{1,2}$ ' the standard deviation (or width of the bell profile) and takes the following values:

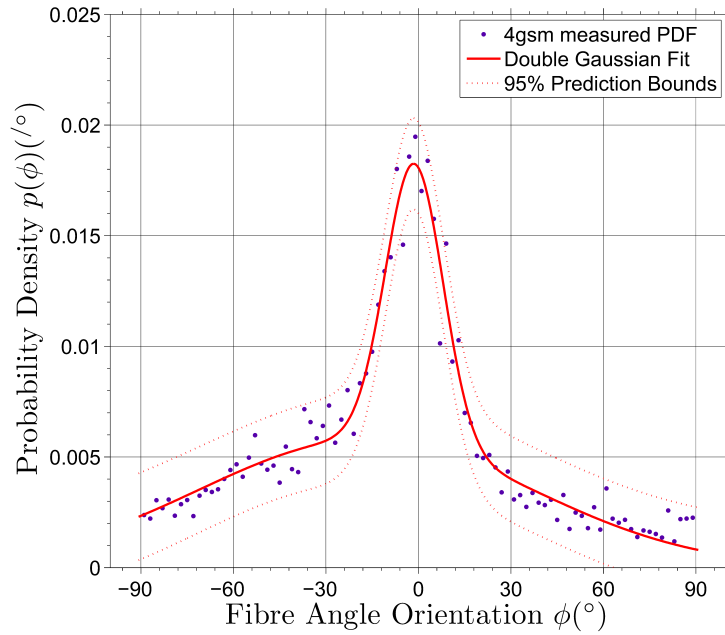
Table 5.1 The coefficients of the double Gaussian PDF

Coefficient	Areal Weight	
	$4g/m^2$	$10g/m^2$
a_1	0.0127	0.01191
b_1	-1.353	0.115
c_1	13.17	15.76
a_2	0.00579	0.00556
b_2	-17.1	-5.984
c_2	75.76	73.26

5.2 Fibre Angle Distribution: Methodology



(a) A comparison of PDF's derived from 4 and 10 g/m^2 materials



(b) A double Gaussian function fitted to the fibre angle distribution of a 4 g/m^2 material

Fig. 5.7 PDF's determined from measurements of the fibre angle distribution using the Hough transform method over 50 images (approximately 10,000 fibres)

5.2.4 Calculation of the Geometry Factor Φ

Arising from analysis of the physical behaviour of nonwoven fabrics (reported in Chapter 4), a new variable defined, as the Geometry Factor $\Phi(\phi)$ can be introduced [70]. This is a geometrical factor, dependant on the fibre angle distribution, enabling a material's anisotropy to be described efficiently in X or Y orientations. To illustrate further, in a more uniform structure, such as a square mesh, the Geometry Factor values are defined as $\Phi(0^\circ) = \Phi(90^\circ) = 0.5$ because equal amounts of the structure lie in each direction. In a 1D diffraction grating, all of the structure lies parallel and in one direction resulting in a Geometry Factor defined as $\Phi(0^\circ) = 1$ and $\Phi(90^\circ) = 0$. In a nonwoven fabric, the Geometry Factor can be calculated by integrating the PDF over the range of possible angles (in radians) and multiplying by the following trigonometric terms for each orientation:

$$\Phi_x = \int_{-\frac{\pi}{2}}^{\frac{\pi}{2}} p(\phi) \cdot \cos^2(\phi) \delta\phi \quad (5.2a)$$

$$\Phi_y = \int_{-\frac{\pi}{2}}^{\frac{\pi}{2}} p(\phi) \cdot \sin^2(\phi) \delta\phi \quad (5.2b)$$

Where $\Phi_x + \Phi_y = 1$.

In order to determine the Geometry Factor for the real materials in the study it is possible to solve this integral computationally using Matlab's 'quadgk' function. Later it was also found that the Geometry Factor can be directly calculated from the individual fibre lengths and angles using a numerical approach, bypassing the use of the PDF. This was calculated using the following expression:

$$\Phi = \frac{1}{\sum_{n=1}^{N_f} l_f^n} \langle l_f^n \cos^2(\phi_n) \rangle = \frac{1}{\sum_{n=1}^{N_f} l_f^n} \sum l_f^n \cos^2(\phi_n) \quad (5.3)$$

5.2 Fibre Angle Distribution: Methodology

Table 5.2 shows a comparison of the results from the two methods, which are in good agreement. The Geometry Factor values are very similar for both $4g/m^2$ and $10g/m^2$ nominal areal weights fabrics. The calculated Geometry Factors are later used as part of both the numeric and analytic model generation protocols.

Table 5.2 Calculated Geometry Factor values of the nonwoven veil using two methods

Areal Weight	Method: PDF using 'quadgk'		Method: Directly from histogram	
	Φ_x	Φ_y	Φ_x	Φ_y
4.4 g/m^2	0.719	0.275	0.716	0.284
11.1 g/m^2	0.740	0.254	0.738	0.262

5.2.5 Geometry Factor Error Analysis

When calculating the PDF there are two sensitivities which could lead to errors in the calculation of the Geometry Factor if not carefully considered. The first, is the sensitivity of the Hough transform function to the fibres in a given image, controlled within the algorithm by a Hough threshold parameter H_t . The Hough threshold can take any value between 0 and 1, the closer this value is to 1 the lower the Hough transform's sensitivity to identifying fibres. Figure 5.8 shows how different values of the Hough threshold parameter impact the calculation of the Geometry Factor. In noisy images (perhaps containing binder fragments), low threshold values can cause the algorithm to falsely identify image artefacts which are not fibres, although the previously mentioned image clean up routine significantly reduces this issue.

For Hough threshold values $H_t > 0.6$ the transform loses sensitivity to enough fibres that the Geometry Factor is miscalculated. For threshold values $H_t \leq 0.6$ the geometry factor converges, therefore a value less than this ($H_t = 0.4$) was used in the final analysis. Figures 5.9a and 5.9b demonstrate the visual impact of choosing different threshold values.

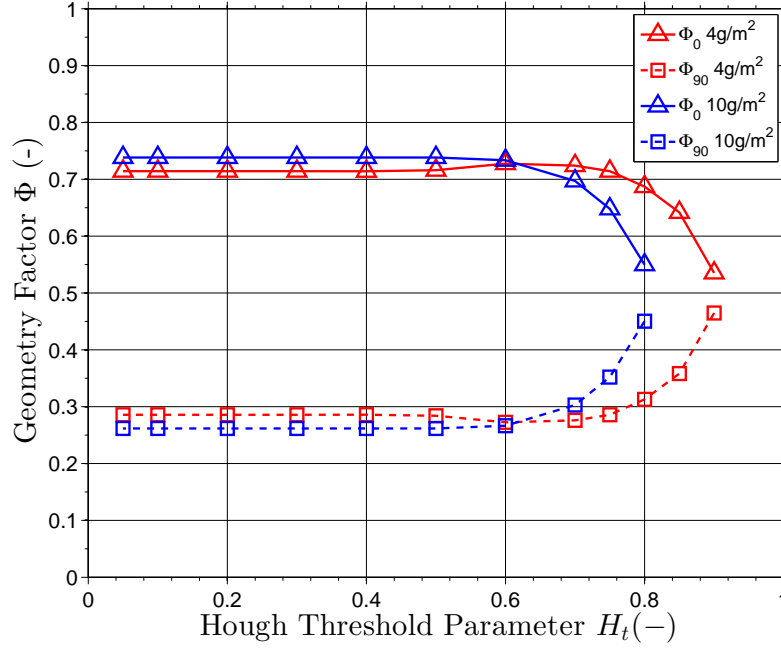


Fig. 5.8 The impact of Hough threshold H_t on the Geometry Factor Φ

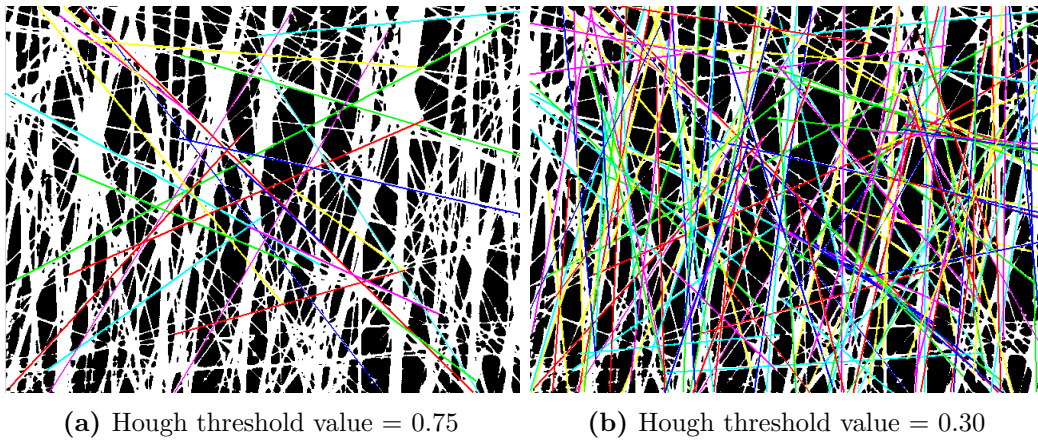


Fig. 5.9 Images showing identified fibres at two different Hough threshold values in $10g/m^2$ materials

5.2 Fibre Angle Distribution: Methodology

The second sensitivity is the impact of the histogram bin width on the Geometry Factor. This occurs because changing the histogram bin width can significantly change the graph's shape and therefore the coefficients within the fitted PDF. Figure 5.10 shows the impact of different sized bins, between $0.5 - 20^\circ$ on the Geometry Factor.

The effect of bin width was later overcome by calculating the Geometry Factor directly from the histogram data using the numerical solution in equation 5.3 is plotted on the y-axis in green and yellow. The numerical solution of the Geometry Factor agrees with the histogram solution provided the bin width is $\leq 6^\circ$. At bin widths above 6° , the shape of the PDF is compromised to such a degree that it no longer can be used to calculate the Geometry Factor accurately.

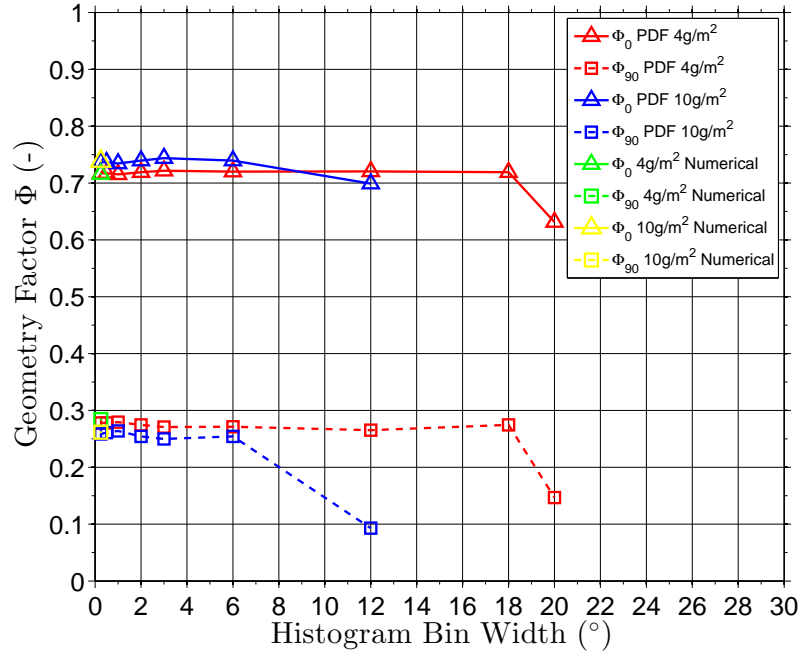


Fig. 5.10 The impact of histogram bin widths on the Geometry Factor Φ

5.3 Development of Numerical Models

5.3.1 Monte Carlo Modelling

Monte Carlo methods are extremely useful in simulating systems in which some of the parameters have a random variation according to a known probability density function and often consist of a range of computational algorithms that depend on repeated random sampling in order to obtain results. In this case, a Monte Carlo approach is used to generate a three-dimensional nonwoven fabric model. Algorithms were developed that pseudo-randomly generate fibres within a defined space, constraining their position by applying particular logic based rules. Generating the fibres in this manner enables an accurate numerical model to be constructed which can later be used to simulate a range of different physical problems. The repeated random sampling of these models also enables features such as the local scale variability to be reflected. A flow chart of the key programming files is shown in 5.11.

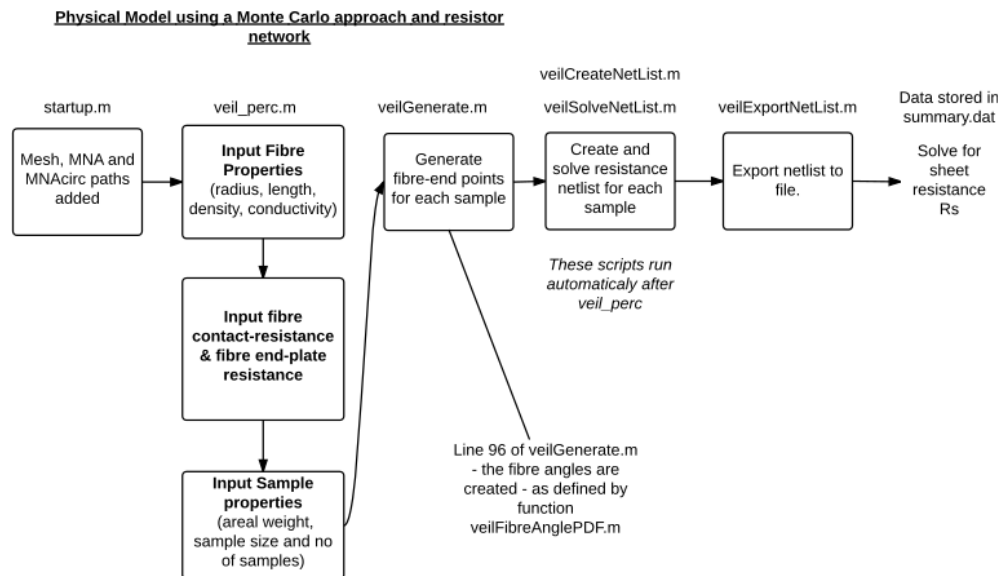


Fig. 5.11 The key programming steps used to generate the numerical models

5.3 Development of Numerical Models

5.3.2 Micro-structure Generation

Micro-structural models were generated by writing algorithms which incorporate factors such as; the fibre properties (length, diameter, density, mass) and sheet properties (volume, areal weight, fibre angle distribution) to produce representative soft-core (inter-penetrating) fibre models. Because some of these factors vary locally within the material, first a large material model is generated from which a number of smaller samples are taken (which is analogous to the experimental process in which smaller samples are cut from larger pieces). The coordinate system used to define the material is shown in figure 5.12 and a typical model with four samples is shown in 5.13. The algorithm for generating the model was implemented using the MATLAB programming language [71] and consists of the following steps:

1. Define a volume larger than the sample size (in the x and y directions) by at least half a fibre length and equal to the thickness in the z direction. The area is made larger than the veil size (the blue region in figure 5.13) so that partial fibres are produced that intrude into the volume at the edges.
2. Randomly generate the positions of the desired number of sample regions (the red regions of figure 5.13).
3. Generate a fibre midpoint within the volume using a uniform random distribution in x, y and z.
4. Generate the azimuthal angle (ϕ) for the fibre according to the empirical angular PDF previously defined in equation 5.1.
5. Generate the elevation angle (θ) with a uniform distribution, but limiting its range so that the end-points of the fibre are within the thickness of the volume.
6. Determine the mass of the fibre that lies within each sample and add this to a mass accumulator.
7. Determine if the fibre is within the specified sample regions. If inside, truncate the fibres at the edge of each sample and store the segment end-points, separately for each defined sample region.
8. Repeat 3-7 until the mass of sample gives the required areal density.

Modelling Methodology of Nonwoven Fabrics

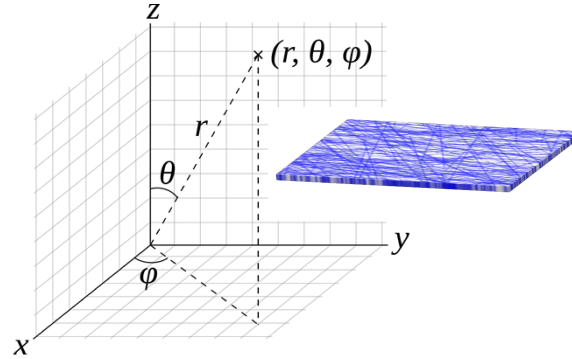


Fig. 5.12 The co-ordinate system used to generate the nonwoven fabric geometry - the sample lies in the XY plane, thickness along the Z plane. X is along the 0° orientation and Y along the 90° orientation

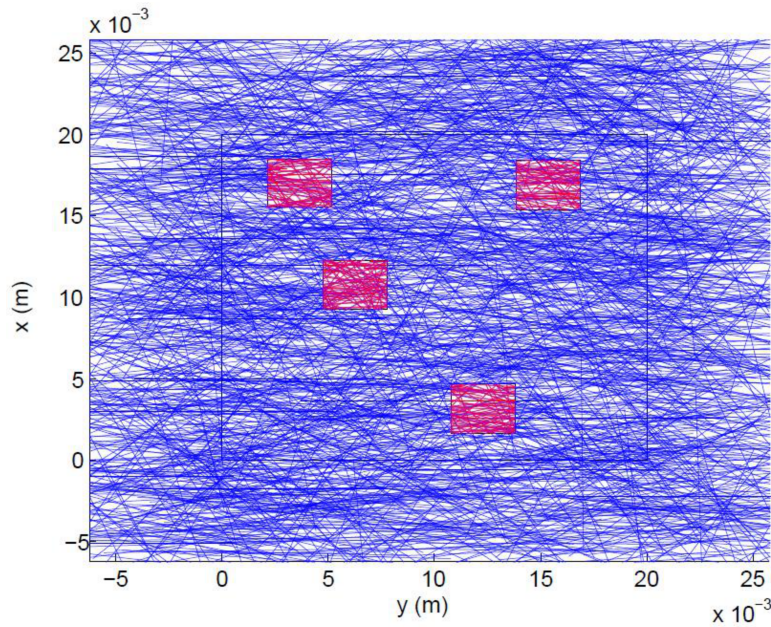
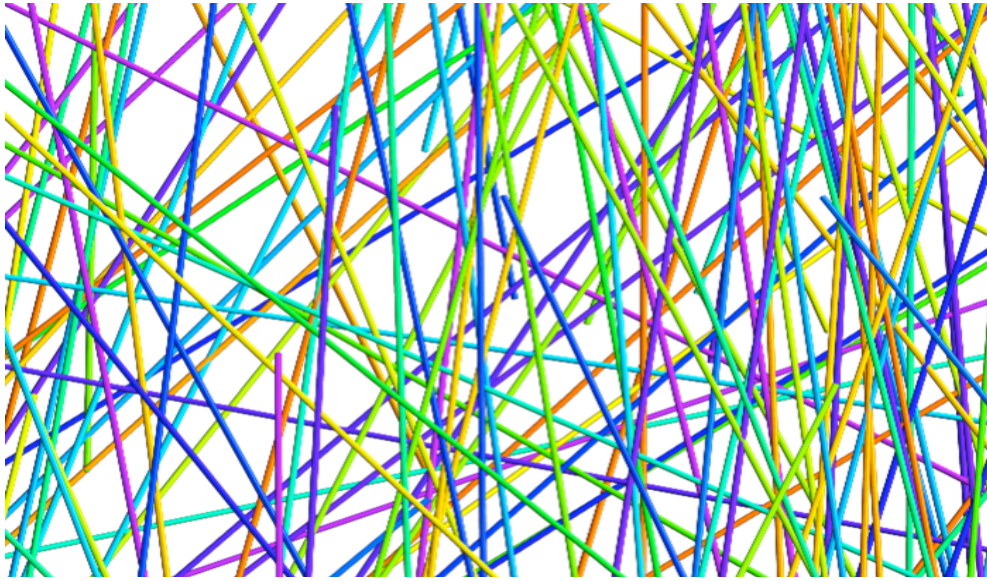


Fig. 5.13 A plan view of the holistic stochastic fibre model, directly generated by the written algorithms. Four samples (red) are shown here. 50 samples were used to generate the data in the later results

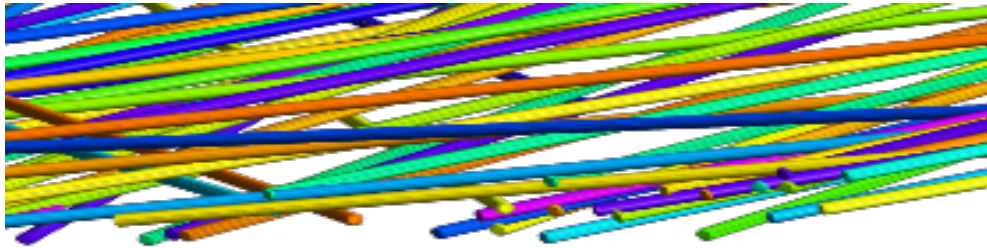
5.3 Development of Numerical Models

5.3.3 Meshing of 3D CAD geometries

Until now, the fibres within the model were represented spatially as two-dimensional lines. Their three-dimensional structure can be meshed into more realistic CAD geometries by transforming the line segments into cylinders using a mesher such as Gmsh [72]). Gmsh is a 3D finite element mesh generator which enables the meshing of structures by meshing points into lines, lines into surfaces and surfaces into volumes. Examples of meshed fibres are shown in figures 5.14 and 5.17.



(a) Plan view



(b) Cross sectional view

Fig. 5.14 The meshed CAD output of the Monte Carlo generated nonwoven fabric structure

5.3.4 Equivalent Resistor Networks

Using the micro-structure ensemble as a framework, it is possible to transform the geometric features of the physical model to an equivalent circuit model. Such a circuit model is formed by representing the fibres in the structure with a quantity of corresponding resistors. The resistance of each line segment can be calculated as $R_f = \frac{l_f}{\sigma A}$, where σ is equal to the conductivity of the real fibre and l_f refers to the length of fibre under consideration (truncated or otherwise). A second set of resistors R_j is also required to represent the mean inter-fibre contact resistance. These contact points can be identified by searching for all of the fibre pairs which lie within a defined separation distance δ . Fibres whose minimum separation distance is less than one fibre diameter ($7\mu m$) are regarded as contacting at the points of closest approach. It is also necessary to identify the points of contact between the fibres and the boundaries of the sample, across which a voltage is applied for the polarization under consideration.

The ends of each fibre are connected to the reference node via a $R_\infty = 100M\Omega$ resistor. This eliminates the iterative removal requirement of floating parts of the structure that would otherwise lead to a singular modified nodal analysis matrix. A DC source is applied between the nodes corresponding to the two opposite boundaries of the sample and the current through the source is monitored to allow the conductance of the sample to be determined. The constructed circuit net-list of fibres can then be analysed using a nodal analysis tool such as SPICE [73].

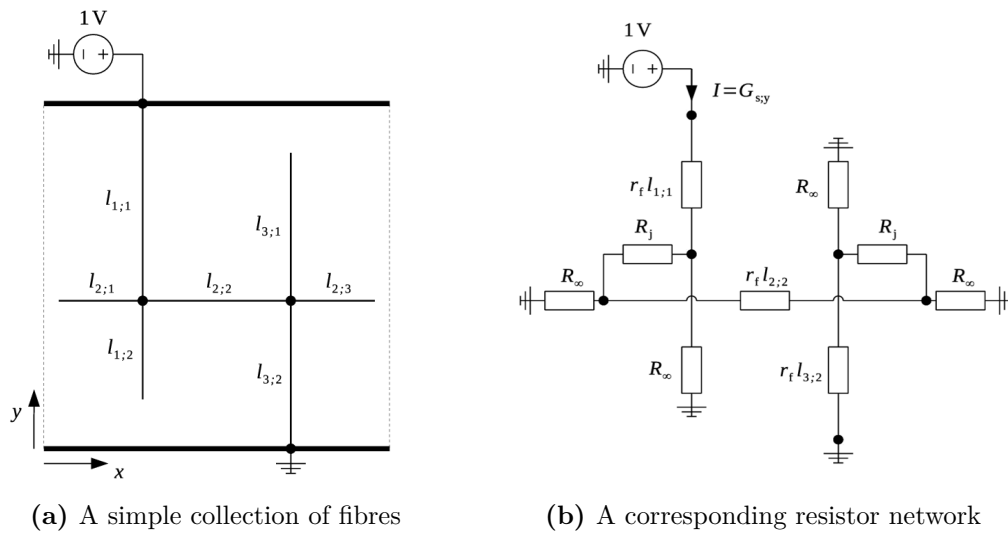


Fig. 5.15 An equivalent circuit model of the fibre network

5.3 Development of Numerical Models

Figure 5.16 shows instances of fibres which lie within the minimum separation distance δ and are therefore assumed to be in contact, visually highlighted using a sphere placed at the crossing point.

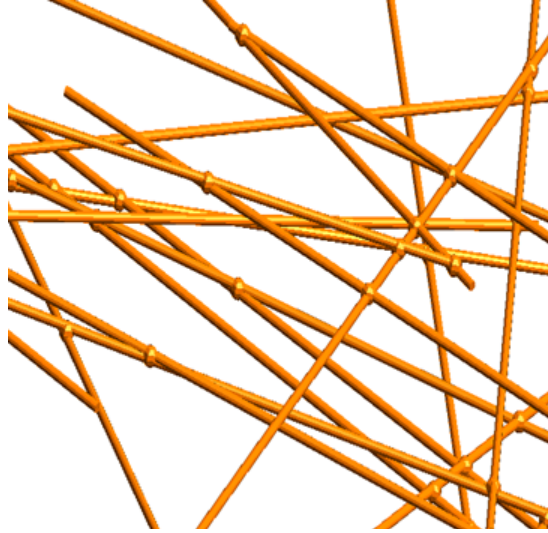


Fig. 5.16 A CAD image portraying the fibres and contact points between fibres

Simple Validation Cases

A number of simple validation cases were run in order to check that the Monte Carlo model produces results that agree with simple circuit solutions (i.e. by applying Ohm's and Kirchhoff's laws). This included checking different conduction planes, fibre orientations, connected and unconnected cases of multiple fibres - examples of which are shown in figure 5.17. For example, taking geometry 5.17(e), a corresponding circuit network can be constructed which consists of an array of resistors used to model the fibres, fibre end points and fibre contact points shown in figure 5.15b. With knowledge of the fibre lengths, resistivity and cross sectional area, the total network's resistance can be calculated manually using simple circuit analysis and compared to the output from SPICE.

Modelling Methodology of Nonwoven Fabrics

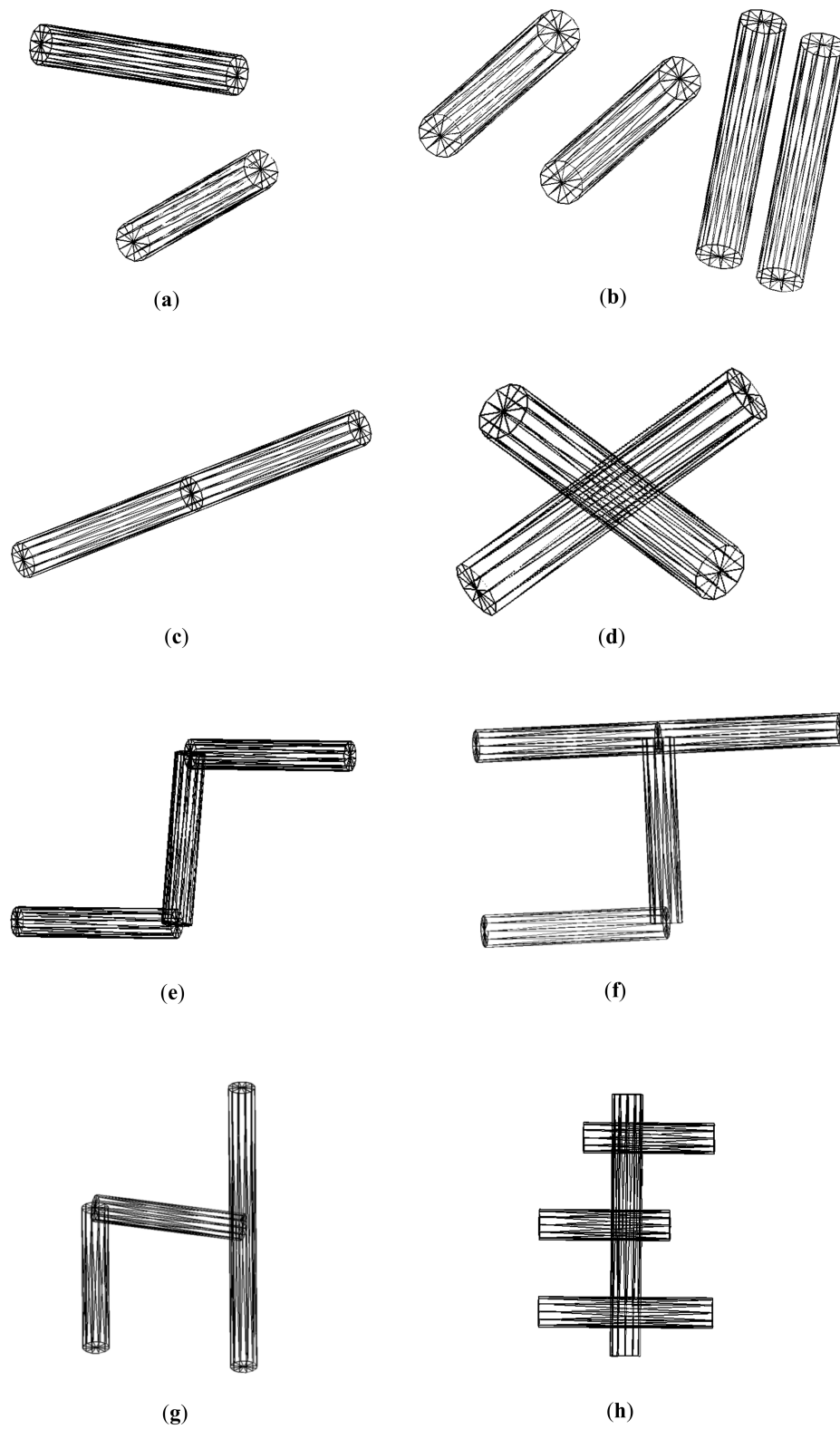


Fig. 5.17 The meshed CAD geometries of simple test cases used to validated the numerical model

5.3 Development of Numerical Models

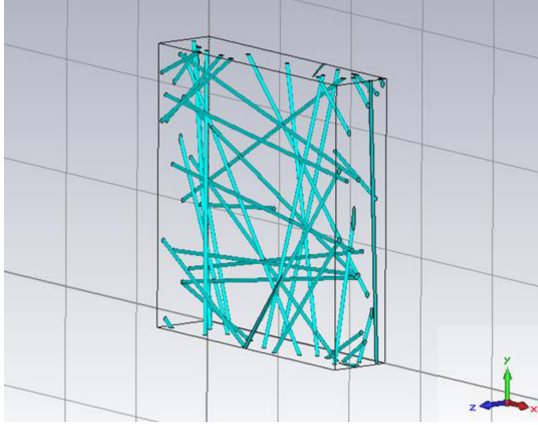
5.3.5 TLM Modelling of the Shielding Effectiveness

The micro-structure model can also be imported into a full-wave computational electromagnetics suite (such as CST Microwave Studio) in order to simulate the AC properties of the materials, such as the shielding effectiveness. Full-wave numerical models of nonwoven fabrics are challenging because of the computational resources required to capture the full scale of the problem, which includes fine features such as the $7\mu\text{m}$ diameter fibres, as well as regions large enough to represent the full variability of the material.

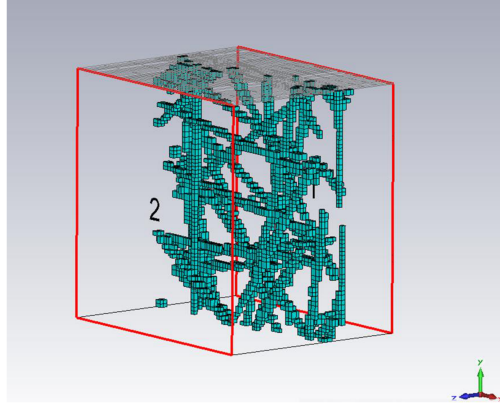
Figure 5.18a shows the CAD representation of a 3×3 mm model of $4g/m^2$ carbon nonwoven fabric within the CST environment. The electrical conductivity of the fibre was defined as 72464 S/m and the magnetic permeability $\mu_r = 1$. Wave-guide ports were used to transmit electromagnetic energy through the problem, exciting frequencies between 0-20 GHz. A perfectly matched layer at each end of the problem is used to absorb all energy, once it has passed through the structure, preventing it from interfering with energy in the problem space. Tangential Magnetic ($H_t = 0$) and electric ($E_t = 0$) boundary conditions are used in the ZX and ZY planes, creating perfectly reflecting boundary conditions. As the excited wave propagates through the modelled volume, the total energy content falls as the field is dissipated by the conductive structure and is absorbed by the matched wave-guide ports. In order to end the simulation without excessively truncating the output field, a termination criteria is set to -80 dB. Wave-guide ports were then used to determine the scattering parameters and shielding effectiveness, using a time domain solver, over a number of sampled regions and polarizations. A cuboid mesh was used (as shown in 5.18d) with approximately 11 million cells of size 0.00175mm in order to discretise the problem in enough detail to resolve the fibre positions sufficiently and calculate the field gradients accurately. Larger mesh sizes were found to reduce the accuracy of the model due to increased staircasing and a thickening effect of the fibres 5.18b, resulting in an artificial rise of the shielding effectiveness.

Figure 5.19 shows the convergence of the shielding effectiveness for the 3 different mesh sizes. As the mesh size is reduced, the fibre's positions are resolved with greater resolution and fibre thickening effects are minimised.

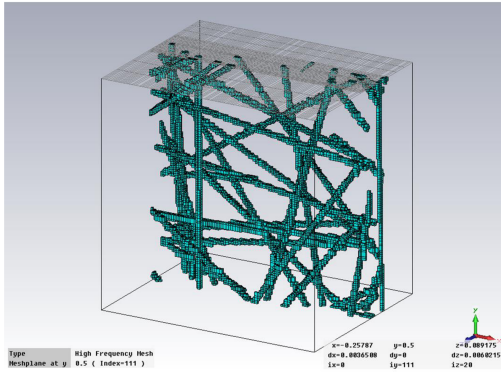
Modelling Methodology of Nonwoven Fabrics



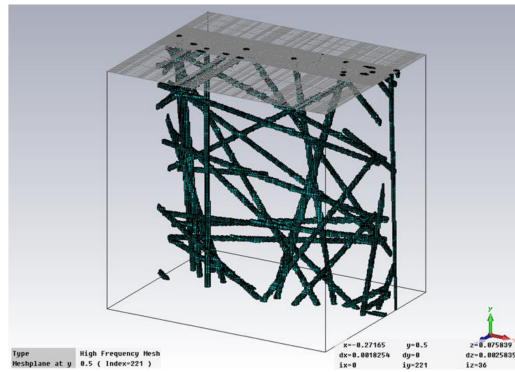
(a) A CAD model of the structure in CST



(b) Mesh representation with cell size = 0.007mm and waveguide ports shown



(c) Mesh representation with cell size = 0.0035mm



(d) Mesh representation with cell size = 0.00175mm

Fig. 5.18 Different resolutions of the mesh and its effect on the fibre's thickness

5.3 Development of Numerical Models

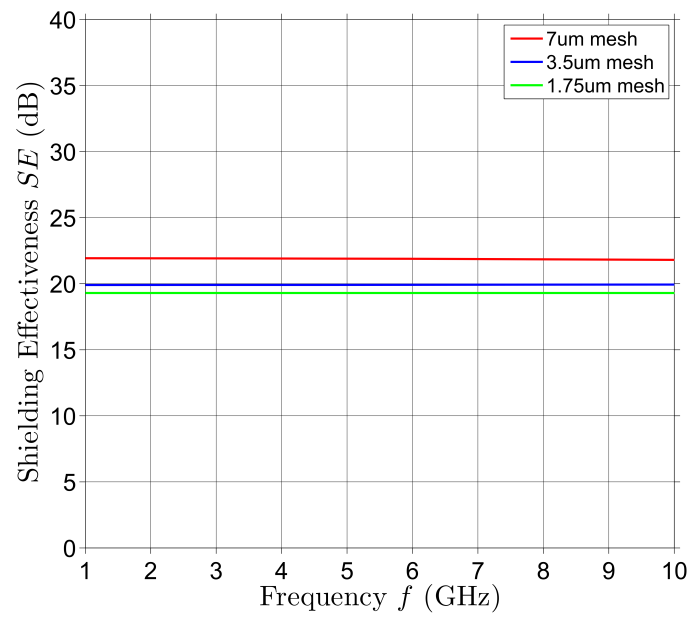


Fig. 5.19 The convergence of finer mesh sizes when modelling a $4g/m^2$ fabric

5.4 Analytic Formulation of the Sheet Conductance

The formulation of analytic expressions of the material's sheet conductance allows insight into the parametric relations that govern the materials performance and enable efficient predictions of the behaviour. In this section, 2D and 3D models are defined, the results of which are given in the following Chapter and compared to experimental and numerical values.

5.4.1 Overall Conductance of a 2D mesh

A real nonwoven fabric consists of both fibres and fibre contacts that act in series to contribute to the total sheet conductance. For a 2D mesh, the total sheet conductance (G_s) is calculated by:

$$G_s = \frac{1}{1/G_{sf} + 1/G_{sc}} \quad (5.4)$$

A nonwoven network with no contact resistance (infinite contact conductance) has a sheet conductance due to the fibres only, G_{sf} . Conversely a network with no fibre conductance has a sheet conductance due only to the contact conductance G_{sc} . These are both hypothetical situations, however in order to simplify the formulation they are initially dealt with separately and then combined in the following sections.

5.4.2 Conductance of a 2D mesh neglecting contact resistance

If the fibre contact conductance G_c is neglected, the sheet conductance G_s is directly equal to the fibre conductance of a square G_{sf} :

$$G_s = G_{sf} \quad (5.5)$$

5.4 Analytic Formulation of the Sheet Conductance

The electrical conductance of a single fibre G_f is given by Pouillet's law:

$$G_f = \frac{\sigma_f A_f}{l_f} \quad (5.6)$$

where σ_f is the bulk conductance of the fibre, A_f is the cross sectional area of fibre and l_f is the length of fibre under consideration. The mass of a single fibre m_f is defined as

$$m_f = \rho_f A_f l_f \quad (5.7)$$

where ρ_f is the fibre density.

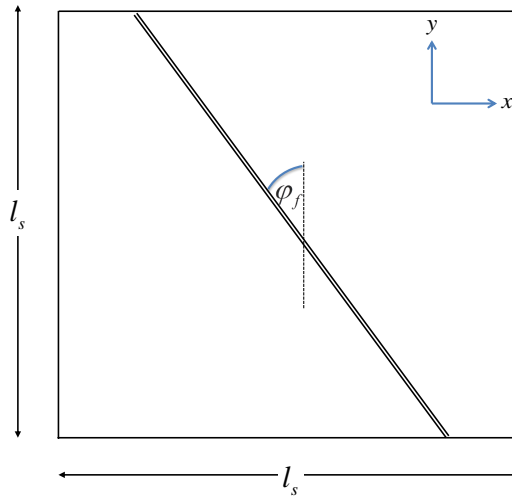


Fig. 5.20 A conducting fibre path in a material of square dimensions l_s

If such a fibre is placed within a square area of dimension $l_s \times l_s$, and angle ϕ_f shown in 5.20, the length of fibre under consideration l_f , required to span the square is equivalent to:

$$l_f = \frac{l_s}{\cos(\phi_f)} \quad (5.8)$$

and the square conductance in the y-direction becomes:

$$G_{sf,y} = \sigma_f A_f \frac{\cos(\phi_f)}{l_s} \quad (5.9)$$

Modelling Methodology of Nonwoven Fabrics

Therefore, if a number of fibres N_f of corresponding angle $\phi_{f,n}$ are present, the square conductivity in the y-direction is:

$$G_{sf,y} = \frac{\sigma_f A_f}{l_s} \sum_{n=1}^{N_f} \cos(\phi_{f,n}) \quad (5.10)$$

It is also possible to define the areal density contribution due to a single fibre:

$$\rho_{Af} = \frac{A_f l_f \rho_f}{l_s^2} = \frac{A_f \rho_f}{l_s^2} \frac{l_s}{\cos(\phi_f)} = \frac{A_f \rho_f}{l_s \cos(\phi_f)} \quad (5.11)$$

If a number of fibres N_f are present at angles $\phi_{f,n}$ then:

$$\rho_A = \sum_{n=1}^{N_f} \rho_{Af,n} = \sum_{n=1}^{N_f} \frac{A_f l_{f,n} \rho_f}{l_s^2} = \frac{A_f \rho_f}{l_s} \sum_{n=1}^{N_f} \frac{1}{\cos(\phi_{f,n})} = N_f \langle \rho_{Af} \rangle \quad (5.12)$$

where $\langle x \rangle = \frac{1}{N_f} \sigma_f A_f \sum_{n=1}^{N_f} x$ is the average of x over N_f fibres. It is worth remembering that the length of the fibre under consideration l_f is a variable that is dependant on the angle such that it is always adjusted to span the square region.

Rearranging 5.12

$$\frac{A_f}{l_s} = \frac{\rho_A}{\rho_f} \sum_{n=1}^{N_f} \cos(\phi_{f,n}) \quad (5.13)$$

and substituting into the square conductance (5.10):

$$G_{sf,y} = \sigma_f \frac{\rho_A}{\rho_f} \frac{1}{N_f} \sum_{n=1}^{N_f} \cos^2(\phi_{f,n}) \quad (5.14)$$

We can now introduce the Geometry Factor Φ to find:

$$G_{sf,y} = \sigma_f \frac{\rho_A}{\rho_f} \langle \cos^2(\phi_{f,n}) \rangle = \sigma_f \frac{\rho_A}{\rho_f} \Phi_y \quad (5.15)$$

5.4 Analytic Formulation of the Sheet Conductance

The value of the y-direction Geometry Factor $\Phi_{x,y}$ depends on the angular distribution of fibres. If the angular distribution is known, we can evaluate the average numerically or approximate using the integrals shown below:

$$\Phi_y = \langle \cos^2(\phi_f) \rangle = \frac{1}{N_f} \sum_{n=1}^{N_f} \cos^2(\phi_{f,n}) = \int_{-\pi/2}^{\pi/2} p(\phi) \cos^2(\phi) d\phi \quad (5.16)$$

$$\Phi_x = \langle \sin^2(\phi_f) \rangle = \frac{1}{N_f} \sum_{n=1}^{N_f} \sin^2(\phi_{f,n}) = \int_{-\pi/2}^{\pi/2} p(\phi) \sin^2(\phi) d\phi \quad (5.17)$$

$$\Phi_x + \Phi_y = 1 \quad (5.18)$$

5.4.3 Conductance of a 2D mesh with contact resistance

Electric current travelling between fibres experiences a contact resistance. The value of this resistance depends on the effectiveness of each contact k_e determined by the contact area, pressure and potential difference that exists between fibres. As half the contacts are considered to allow current to flow onto the fibre and half to allow current to flow off each fibre, division by a factor of 2 is also necessary. Defined in detail by Dawson [74], the mean number of contacts per fibre for a 2D isotropic case is:

$$N_{cf} = P_{cont} \pi \frac{\rho_A l_f^2}{m_f} \quad (5.19)$$

where $P_{cont} = 0.2027$ is the mean contact probability predicted by Heitz [46]. Here the length of the fibre under consideration l_f , is the chopped fibre length.

The square conductance due to the contacts in 2D cases (derived in more detail in [75] is therefore:

$$G_{sc} = \frac{k_e N_{cf}}{2} G_c \frac{\rho_A l_f^2}{m_f} \Phi \quad (5.20)$$

Where $k_e = 0.1696$ by equating coefficients to that of Zezelj and Stankovic for a uniform fibre angle distribution.

Modelling Methodology of Nonwoven Fabrics

Combining the contact conductance and the fibre conductance (equation 5.15) in series, the total sheet conductance of a 2D nonwoven fabric is:

$$G_s = \frac{1}{\frac{1}{\sigma_f \frac{\rho_A}{\rho_f} \Phi} + \frac{2}{k_e N_{cf} G_c \frac{\rho_A l_f^2}{m_f} \Phi}} \quad (5.21)$$

5.4.4 Conductance of a 3D mesh with contact resistance

Building on the mathematics of the uniform 2D model, an anisotropic 3D model can be generated by including the effects of anisotropy and thickness \tilde{t} on the mean number of contacts per fibre (N_{cf}).

Taking these in turn, the number of contacts per fibre predicted by Heitz for a uniform 2D distribution (N_{cHeitz}) was compared to a truncated Gaussian PDF 2D Monte Carlo Model (N_{cMCM})². Figure 5.21 shows that for truncated Gaussian PDFs (i.e. aligned materials) the number of contacts is reduced compared to the uniform case. This is approximated well by the term $\frac{N_{cHeitz}}{N_{cMCM}} = \sqrt{\sin(\pi\Phi)}$.

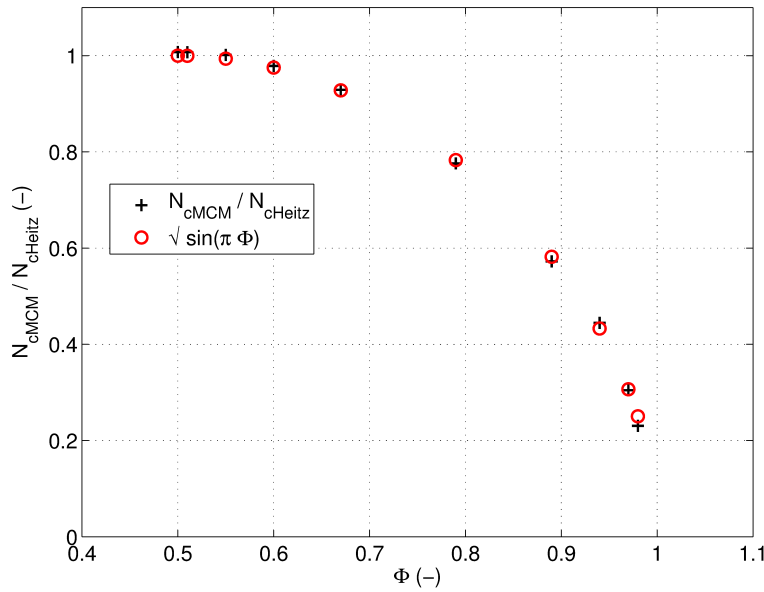


Fig. 5.21 Comparing the number of contacts per fibre predicted by Heitz for a uniform 2D sheet with 2D MCM sheets with a Gaussian angular PDF and an empirical estimate

The effect of thickness on the number of contacts per fibre can also be determined in a similar way. In this case a comparison of the mean number of contacts

²The Monte Carlo Models referred to have not yet been introduced or defined. However they were important in developing the 3D analytic models and therefore they are referenced here

5.4 Analytic Formulation of the Sheet Conductance

for Heitz's 2D uniform distribution is made to the mean number of contacts for uniform 3D MCM models. In Figure 5.22, a comparison of the 3D uniform MCM model to 2D uniform case also shows the number of contacts per fibre reducing with thickness. This occurs because in the 3D case once enough fibre has amassed the material's density stops increasing and the total thickness increases. Whereas in the 2D case, all of the fibre is forced to exist in the same plane and so increasing the areal concentration of fibre, forces the density and therefore the mean number of contacts per fibre to increase.

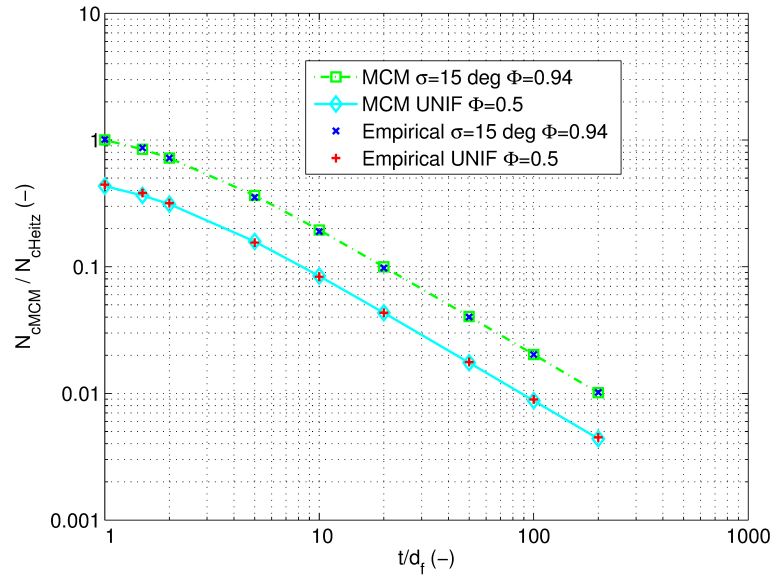


Fig. 5.22 Comparing the number of contacts per fibre predicted by Heitz for a uniform 2D sheet with 3D MCM sheets, and an empirical estimate

Taking into account the change in number of contacts due to the non-uniform distribution of fibre angles and the effects of thickness, the following relationship was derived empirically for 3D anisotropic samples (reported in [75]):

$$N_{cf} = P_{cont} \pi \frac{\rho_A l_f^2}{m_f} \sqrt{\sin(\pi \Phi)}^{1.5} \sqrt{\frac{1 + (0.66)^{1.5}}{1 + (0.66 \tilde{t})^{1.5}}} \quad (5.22)$$

Where \tilde{t} was defined (equation 3.2).

Modelling Methodology of Nonwoven Fabrics

Substituting this into equation 5.21, the anisotropic 3D sheet conductance of a nonwoven network can be defined as:

$$G_s = \left[\sigma_f \frac{\rho_A}{\rho_f} \Phi + \frac{2G_c \frac{\rho_A l_f^2}{m_f} \Phi}{k_e P_{cont} \pi \frac{\rho_A l_f^2}{m_f} \sqrt{\sin(\pi \Phi)}^{1.5} \sqrt{\frac{1+(0.66)^{1.5}}{1+(0.66t)^{1.5}}}} \right]^{-1} \quad (5.23)$$

If one is to include the percolation threshold and critical exponent from Zezelj [51] and equate coefficients, the full expression for the 3D sheet conductance can be written as:

$$G_s = \frac{(\tilde{n}_A - n_c)^T + c(L/l_f)}{\frac{\tilde{n}_A^{T-1}}{G_f} + \frac{2\tilde{n}_A(\tilde{n}_A + n_c)^{T-2}}{k_e N_{cf} G_c}} \Phi \quad (5.24)$$

5.5 Summary

The purpose of this chapter was to introduce the methods used to generate micro-structure models of nonwoven fabrics. These models can be used to simulate a range of performance types including the sheet conductance and the shielding effectiveness. A number of challenges had to be overcome in order to generate accurate structure models, including creating structures which had the same fibre angle distribution and variability as the real materials. To solve these challenges, a new measurement technique was developed which enabled the material's fibre angle distribution to be determined from microscope images. The geometry factor (a factor representing the material's anisotropy) was obtained: $\Phi_x = 0.727$, $\Phi_y = 0.273$. This information was coupled with the remaining physical material parameters and incorporated into an algorithm to pseudo-randomly generate the fibres in the model. A Monte Carlo approach was used to create many models allowing the material's local scale variability and mean properties to be assessed.

The micro-structure model was meshed to produce realistic fibre geometries and used directly as inputs to equivalent circuit and TLM modelling frameworks. Finally a semi-analytic model of the material's sheet conductance was presented, drawing upon the previously defined fibre angle distribution (geometry factor) and physical data mentioned.

The next chapter focuses on the results of these models and analyses how they compare to the experimental measurements of the previous chapter.

Chapter 6

Results and Analysis

Results and Analysis

6.1 Overview

This chapter presents the final results of the developed analytic and numeric models discussed in the previous chapter and compares them directly to experimental measurement of the sheet conductance and shielding effectiveness. At low frequencies (where the effects of the skin-depth are negligible) the sheet conductance is the principle factor in determining the shielding effectiveness. However at frequencies where the skin-depth becomes more significant, full wave TLM modelling is required to predict the shielding performance.

Initially the effects of the percolation on the sheet conductance are discussed, before a range of idealised models are considered, concluding with real material models which reveal new insights into parameters such as the mean number of contacts per fibre and the average contact resistance between fibres. Finally the full-wave modelled TLM shielding effectiveness results are presented. Throughout all of the results are compared to the experimentally determined values from chapter 4.

The dimensionless areal concentration \tilde{n}_A is used throughout as a dimensionless measure of the areal weight ρ_A of the material. This is the number of fibres in an area equal to a square of fibre length l_f .

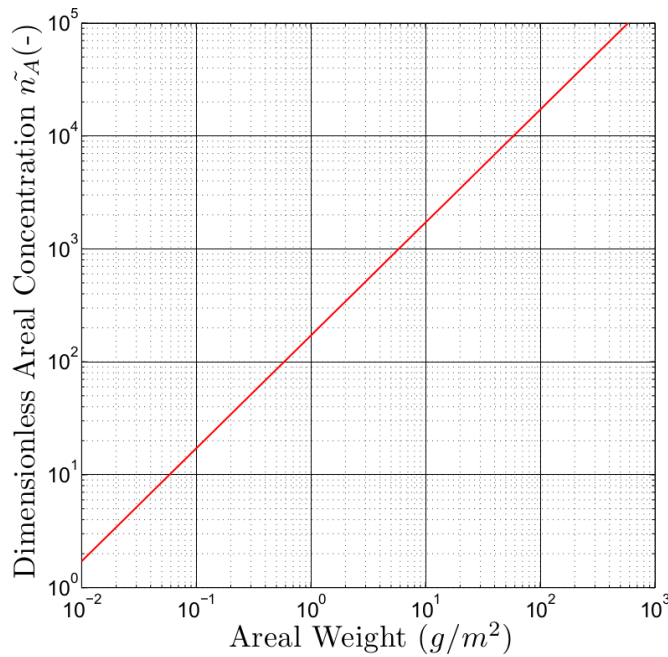


Fig. 6.1 Relationship between the dimensionless areal concentration and areal weight, particular for 12mm fibres of density 1820 Kg/m^3

6.2 Percolation Threshold Models

For convenience figure 6.1 shows the relationship between the dimensionless areal concentration and the areal weight, defined by the following equation;

$$\tilde{n}_A = \frac{\rho_A l_f^2}{m_f} \quad (6.1)$$

6.2 Percolation Threshold Models

Before turning to the sheet conductance results, the MCM simulated percolation thresholds are discussed, which are relevant to all of the models at extremely low areal concentrations $\tilde{n}_A < 90$. In this region the fibres are poorly connected, which results in a corresponding drop in the sheet conductance. Figure 6.2 shows the effect of thickness on the percolation probability for various areal concentrations of uniformly distributed nonwoven fabric. As the thickness is increased, the onset of the percolation threshold ($\langle P_x \rangle = 0.5$) is delayed, resulting in higher areal concentrations being required before connection is established. This occurs because of the extra space afforded to the fibres reduces their probability of producing a spanning cluster required for percolation to occur.

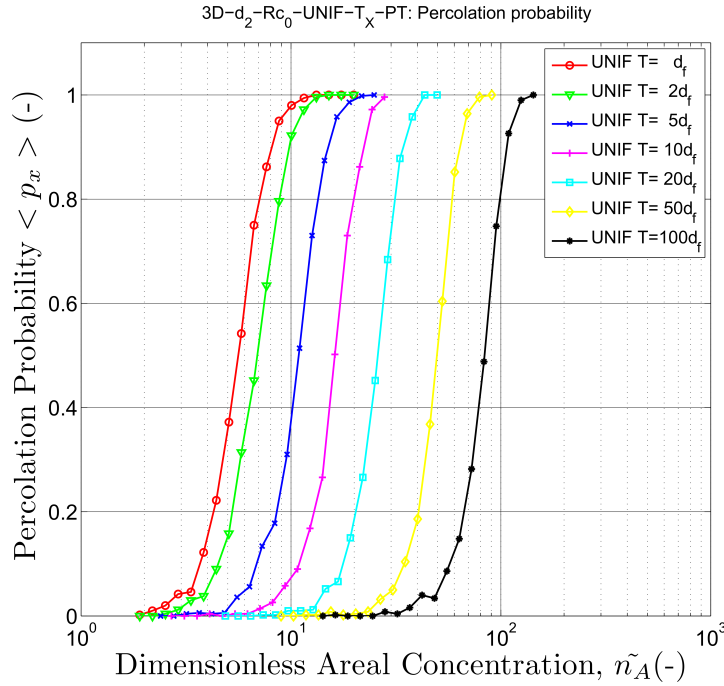


Fig. 6.2 The percolation probability of a 3D MCM with uniform fibre angle distribution at various thickness

Results and Analysis

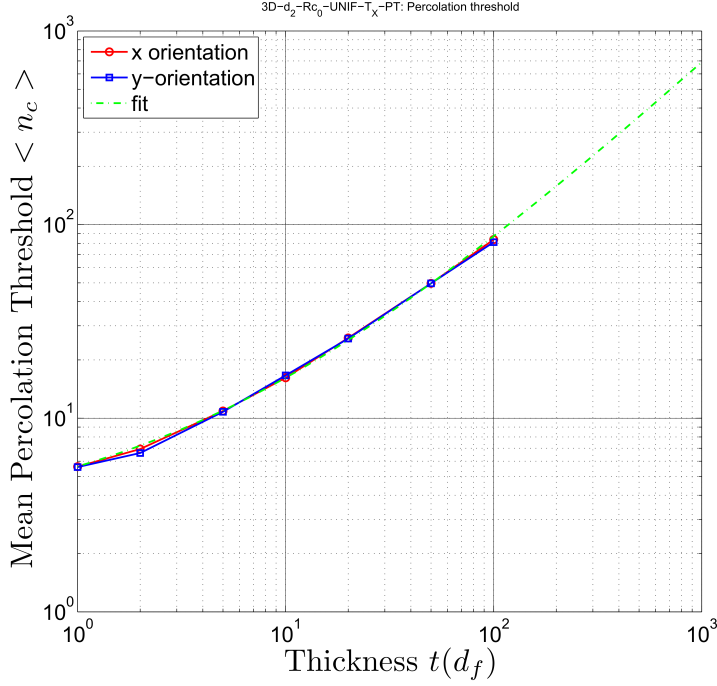


Fig. 6.3 The effect of thickness on the percolation threshold

Figure 6.3 shows the increase in percolation threshold with thickness for a uniform fibre angle distribution, which can be fitted to the following function:

$$n_c = n_{c_0}^{0.4025} \sqrt[0.4025]{\left(\frac{1 + (0.2332t)^{0.4025}}{1 + 0.2332^{0.4025}} \right)} \quad (6.2)$$

Where t is the thickness in fibre diameters (d_f) and $n_{c_0} = 5.63726$ is the percolation threshold for a 2D isotropic sample defined by Heitz [46]

The effects of the percolation threshold occur far below the minimum manufacturable areal concentrations ($\tilde{n}_A = 300$) of nonwoven fabrics and a detailed analysis is not undertaken. The percolation threshold in anisotropic sheets is treated separately by Balberg and Binenbaum [76], with the results showing that the percolation threshold always increases with macroscopic anisotropy. It is also important to point out that the variation in the percolation threshold with sample size affects the sheet conductivity below the percolation threshold [77].

6.3 Sheet Conductance Models

In the following analysis a number of contrasting cases are considered, revealing insight into the possible behaviour of different nonwoven fabric configurations. Configurations include; 2D and 3D models, isotropic and anisotropic fibre angle orientations, superconducting and high resistance inter-fibre contact resistance. The real materials are simulated using a 3D model inclusive of the measured fibre angle orientation and an estimation of the mean contact resistance R_j ¹.

6.3.1 Idealised 2D Case

Figure 6.4 shows the variation in conductance with areal weight of an idealised 2D model of the nonwoven fabric, where the sheet conductance is simulated using a contact resistance $R_j = 0\Omega$ (i.e. superconducting contacts), a fibre resistance $\sigma_f = 72464S/m$ and a uniform fibre angle distribution. The results are compared between MCM (with errorbars of one standard deviation), our developed analytic theory (5.4.1) and an expression given by Zezelj [51]. The MCM closely follows the values predicted by Zezelj over the whole range. The analytic model, which assumes well connected fibres shows good agreement when areal concentrations $\tilde{n}_A > 50$ (i.e. areal densities $> 0.3g/m^2$). At such concentrations, all three models are in good agreement and show a linear increase in the sheet conductance with dimensionless areal weight. Below this value, the fibres are poorly connected and the network connectivity falls dramatically due to the effects of percolation. In this range, the analytic theory becomes inaccurate as it does not account for the effects of percolation.

The variability across the MCM models also increases dramatically below the percolation threshold due to the lower concentrations of fibre, which at higher concentrations are naturally averaged out due to the extra fibres present. It is worth emphasising that dimensionless areal concentrations of $\tilde{n}_A < 50$ cannot be manufactured in practise because the materials do not possess enough tensile strength to be reeled up.

¹The results in this chapter use a vectorised version of the code in order to improve the code's performance by reducing the run time. They were computed on the York Advanced Research Computing Cluster (YARCC), configured with 4 processors, 24 cores, and 64GB of RAM.

Results and Analysis

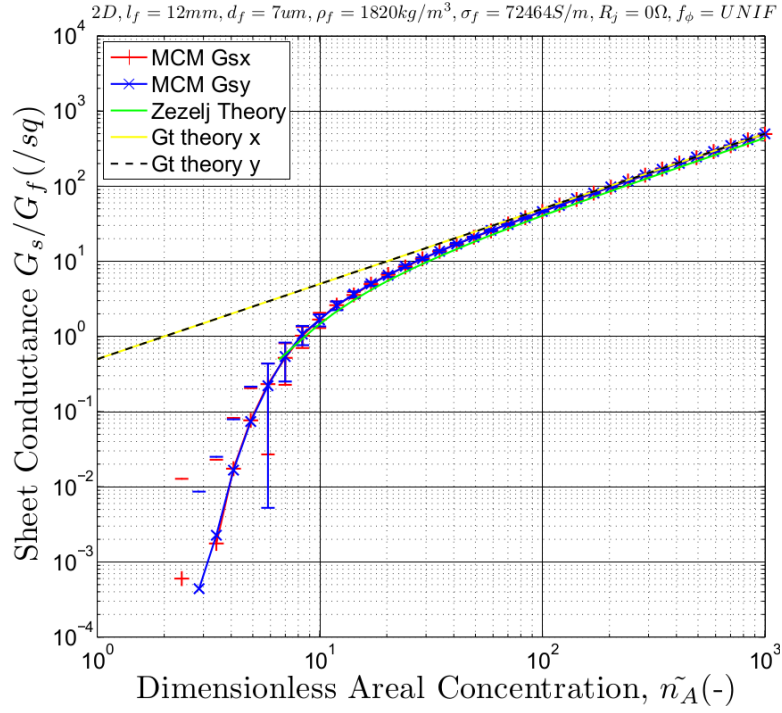


Fig. 6.4 The sheet conductance for a 2D nonwoven fabric with superconducting contacts and a uniform fibre angle distribution.

Figure 6.5 shows the mean number of contacts each fibre makes with its neighbours for the same configuration as 6.4, comparing values from the MCM model, the developed analytic theory and an expression given in the literature by Heitz [46]. All of the models show strong agreement, with a linear increase in the number of contacts with areal concentration. The MCM model is again plotted with error bars at 1 standard deviation. Only the error bar end plates are plotted for the MCM G_{sx} at low areal concentrations.

6.3 Sheet Conductance Models

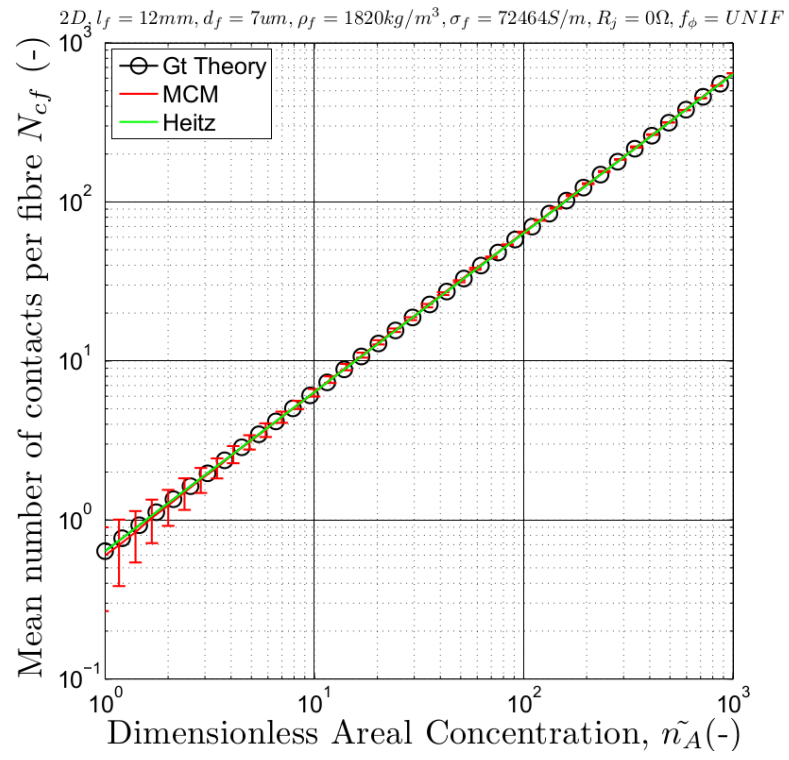


Fig. 6.5 The mean number of contacts per fibre in a 2D model of the nonwoven fabric.

Results and Analysis

Figure 6.6, shows the sheet conductance results for a similar configuration, albeit the contact resistance is modified to $R_j = 1M\Omega$. This impacts the sheet conductance by reducing the sheet conductance values by approximately 4 orders of magnitude. The MCM results closely follow that of Zezelj over the whole range and the analytic model, which assumes well connected fibres follows for areal concentrations $\tilde{n}_A > 50$. Zezelj's expression is not plotted for areal concentrations that are at or below the percolation threshold (i.e $n_{c0} \leq 5.6373$) due to the fact that the function's local conductivity exponent decreases with the decreasing system size.

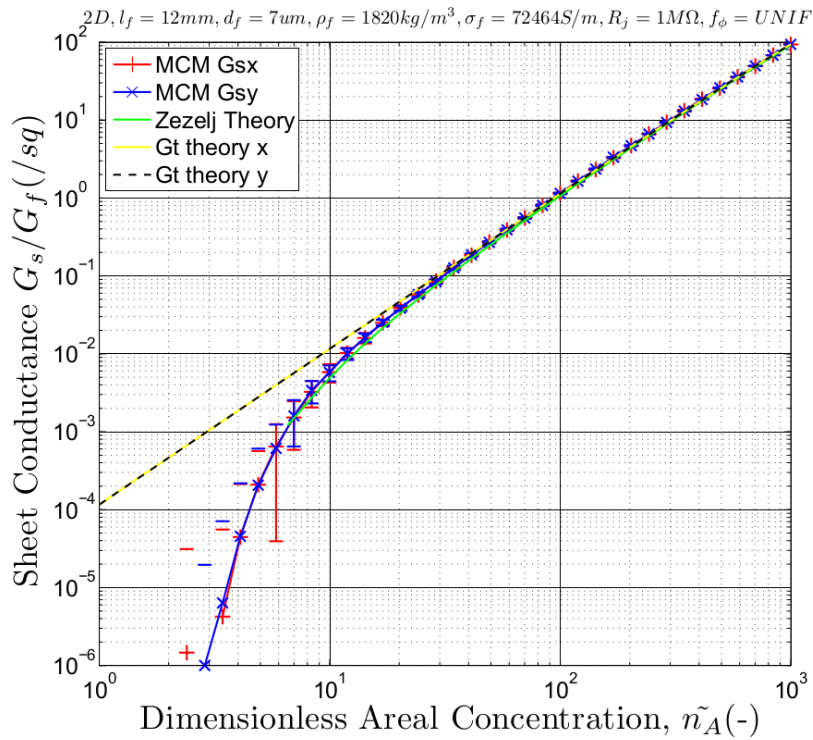


Fig. 6.6 The sheet conductance for a 2D Uniform fibre angle distribution and $1M\Omega$ contacts

Figure 6.7 shows an arbitrarily chosen anisotropic fibre angle distribution, which results in a geometry factor of approximately $\Phi_x = 0.8$, $\Phi_y = 0.2$. The sheet conductance of this configuration, with contact resistance set to $R_j = 0\Omega$ is shown in figure 6.8. The impact of the geometry factor results in different sheet conductances being obtained in the x and y polarisations. The MCM models (plotted with 1 standard deviation) and analytic theory show good agreement for $\tilde{n}_A > 50$, where both models predict the same values of sheet conductance for each orientation. Zezelj's function does not accommodate for the effects of

6.3 Sheet Conductance Models

anisotropic fibre distribution, but is still plotted for comparison and lying between the two anisotropic values.

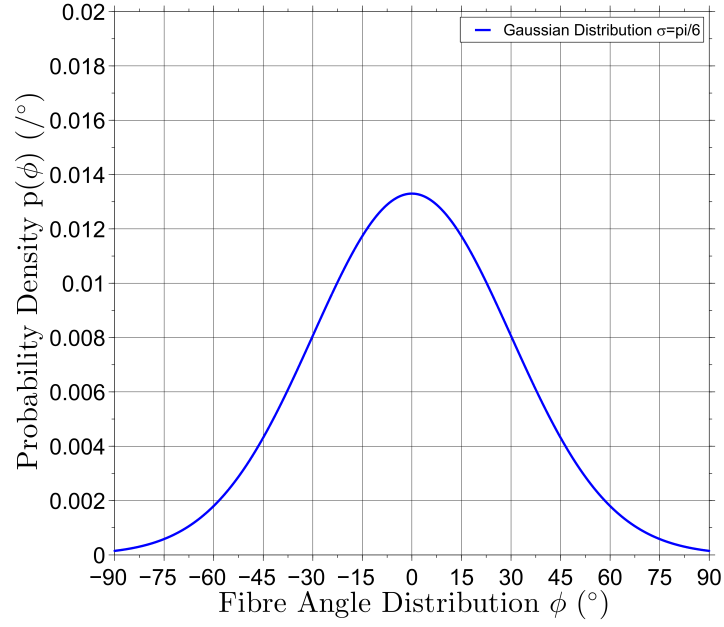


Fig. 6.7 The PDF of a Gaussian fibre angle distribution for $-90 \leq \phi \leq 90$ and $\sigma = 30$

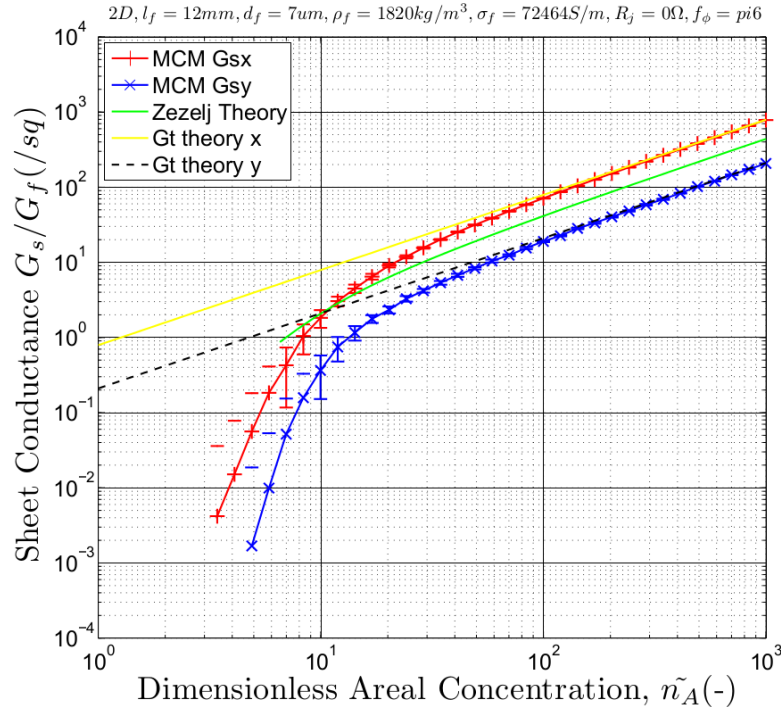


Fig. 6.8 The sheet conductance of a 2D anisotropic sheet ($\Phi_x = 0.8$, $\Phi_y = 0.2$) with superconducting contacts

Results and Analysis

6.3.2 Idealised 3D Case

Number of Contacts per Fibre

In the 3D uniform fibre angle case, the thickness of the material becomes important, directly reducing the mean number of contacts per fibre compared to the 2D model. The analytic model was modified (discussed in section 5.4.4) such that the number of contacts includes a thickness term as defined in equation (5.22). Figure 6.9 shows the levelling off of the mean number of contacts per fibre as the areal concentration surpasses a value of $\tilde{n}_A > 150$, for both the MCM and the developed analytic model, which are in good agreement. Heitz's 2D solution is plotted for reference.

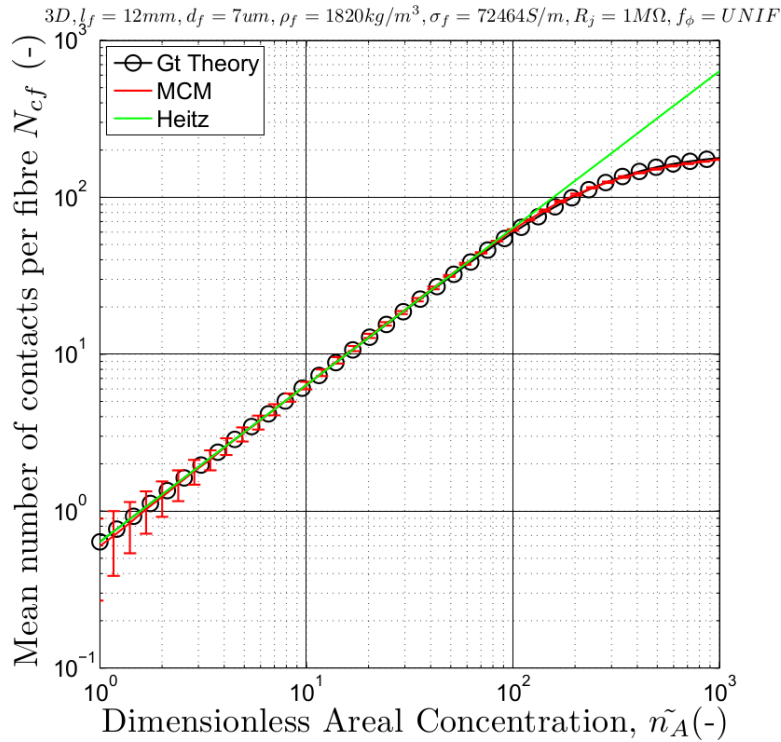


Fig. 6.9 The levelling of the mean number of contact points per fibre from $\tilde{n}_A > 150$ in 3D models compared to the Heitz 2D model which remains linear

In the case of superconducting contacts it is expected and shown that 2D and 3D models still behave identically (provided each fibre is well connected). This is because a change in the number of contacts makes no difference to the total sheet conductance - each contact is electrically invisible.

However in the contrasting case of high contact resistance $R_j = 1\text{M}\Omega$, the reduction in the mean number of contacts per fibre becomes evident from areal

6.3 Sheet Conductance Models

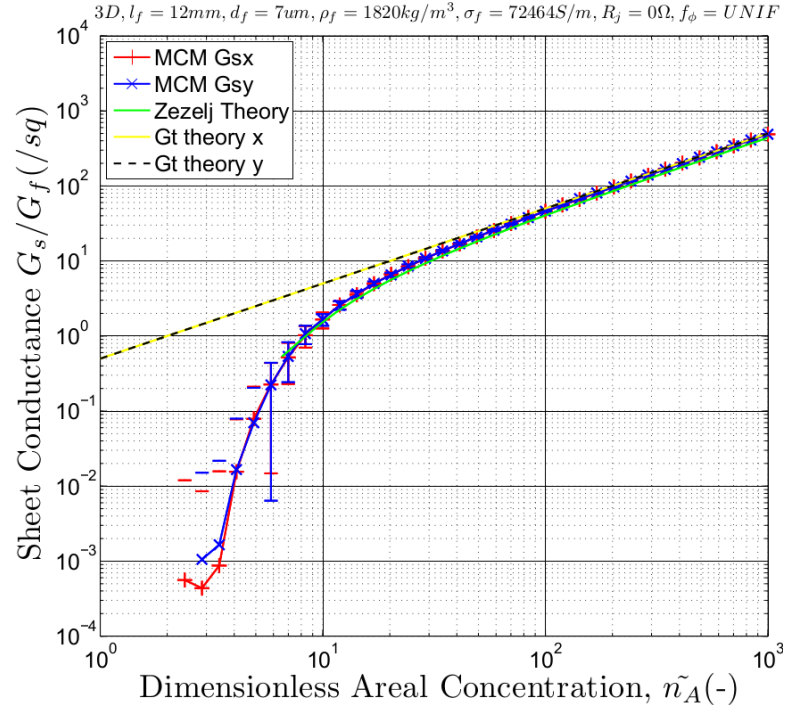


Fig. 6.10 The sheet conductance for a 3D Uniform fibre angle distribution and super-conducting contacts

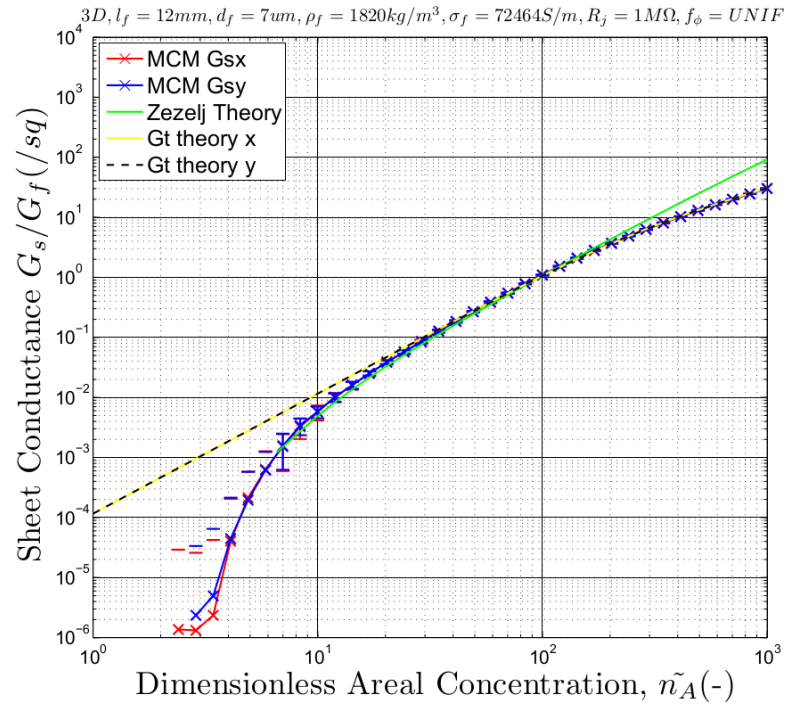


Fig. 6.11 The levelling off of the sheet conductance for the uniform 3D model with a contact resistance of $1M\Omega$

Results and Analysis

concentrations $\tilde{n}_A > 100$ and a corresponding fall in the sheet conductance can be seen in figure 6.11. The developed analytic model agrees well with the MCM results.

Figure 6.12 shows a further 3D case, again with superconducting contacts $R_j = 0\Omega$, and the same anisotropic truncated Gaussian fibre angle distribution of figure 6.8. The effect of the fibre angle distribution on the sheet conductance is again predicted by both the developed analytic and MCM models which correlate with one another above $\tilde{n}_A > 150$.

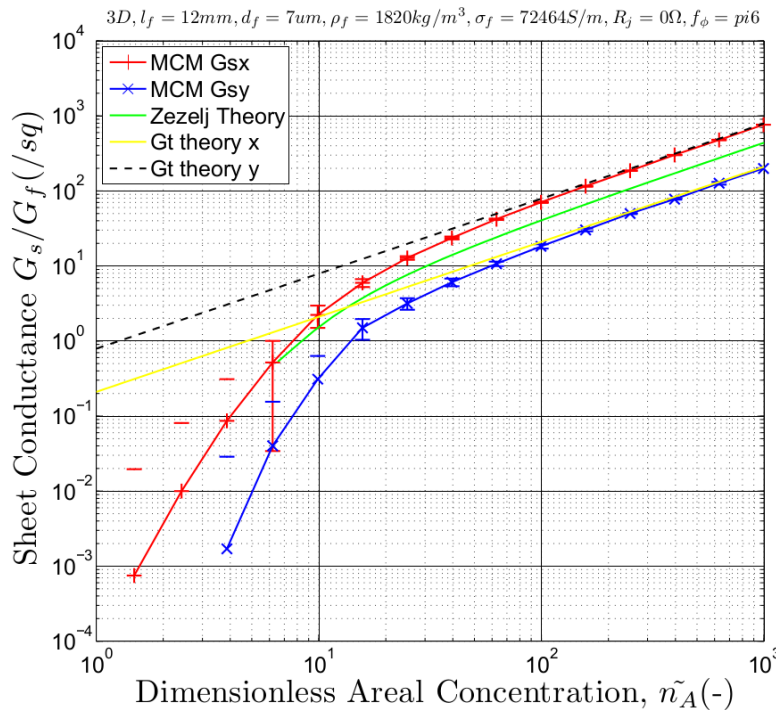


Fig. 6.12 The sheet conductance behaviour of a 3D case with an anisotropic fibre angle distribution and superconducting contacts

Figure 6.13 shows the mean number of contacts simulated from the MCM and analytic models. In the case of the arbitrarily Gaussian fibre angle distribution in figure 6.7, these models display good correlation with each other throughout the areal concentration range, and even with Heitz's 2D model until the thickness effects become evident at $\tilde{n}_A > 100$.

6.3 Sheet Conductance Models

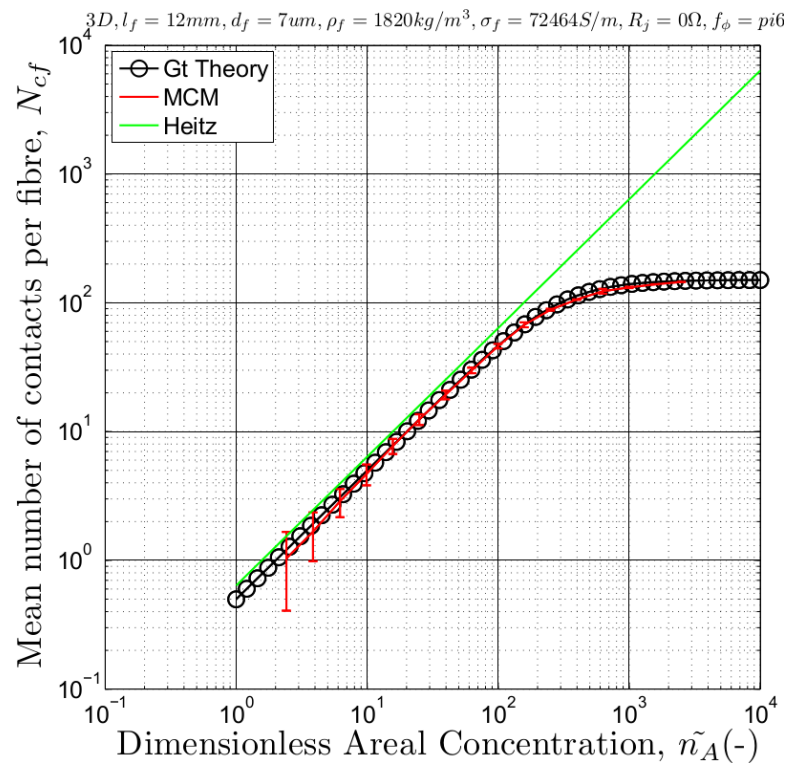


Fig. 6.13 The mean number of contacts per fibre for the 3D case with an anisotropic fibre angle distribution

Results and Analysis

6.3.3 Real Material Models

The fibre angle distribution was determined for 4 and 10 g/m^2 materials by applying the Hough transform (as described in 5.2) to 50 microscope images for each areal weight, shown in figure 6.14. This process yielded the real material's average geometry factors $\Phi_x = 0.727$, $\Phi_y = 0.273$.

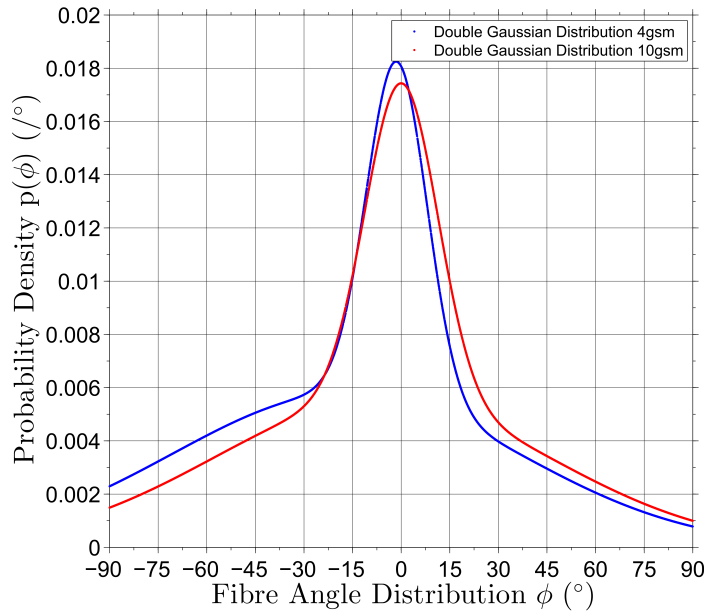


Fig. 6.14 The measured PDF for the fibre angle distribution of 4 and 10 g/m^2 materials

Figure 6.15 shows the MCM and analytic models using the real fibre angle distribution but with an assumed inter-fibre contact resistance $R_j = 0\Omega$.

Good correlation is observed between the analytic and MCM models (with errorbars smaller than the plot markers). The measured sheet conductance is also plotted, possessing a similar orientation divergence between orientations as the modelled data. However the measured data has a lower sheet conductance across the areal concentration range, attributed to the fact that the real material's fibres experience a contact resistance which isn't yet reflected in the model.

Figure 6.16 shows the effect of choosing a mean contact resistance of $R_j = 8.6k\Omega$. The correlation between modelled and measured values, in both orientations is obtained allowing us to conclude that $8.6k\Omega$ is representative of the real fibre's mean contact resistance.

6.3 Sheet Conductance Models

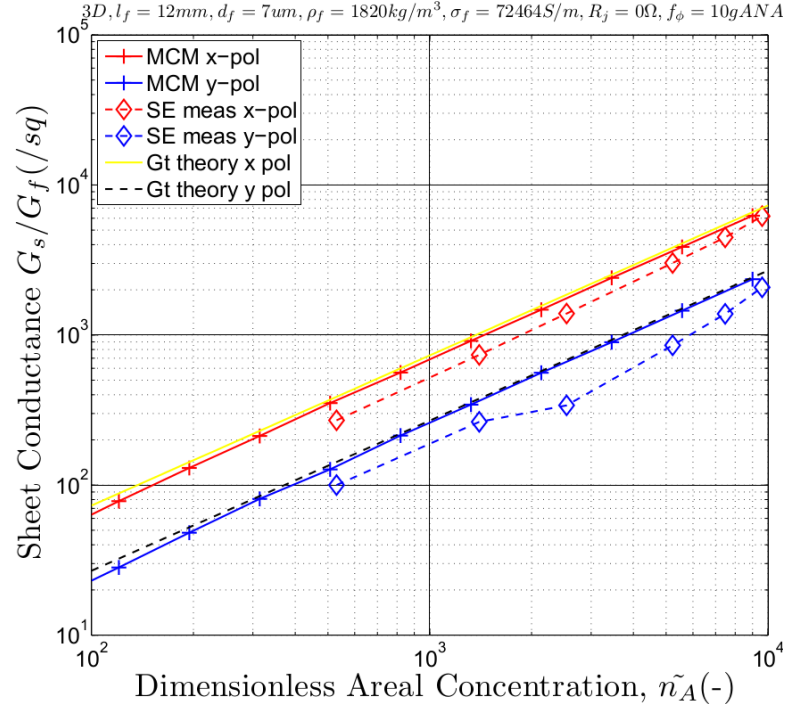


Fig. 6.15 The measured and modelled sheet conductance of real nonwoven fabrics, assuming zero contact resistance

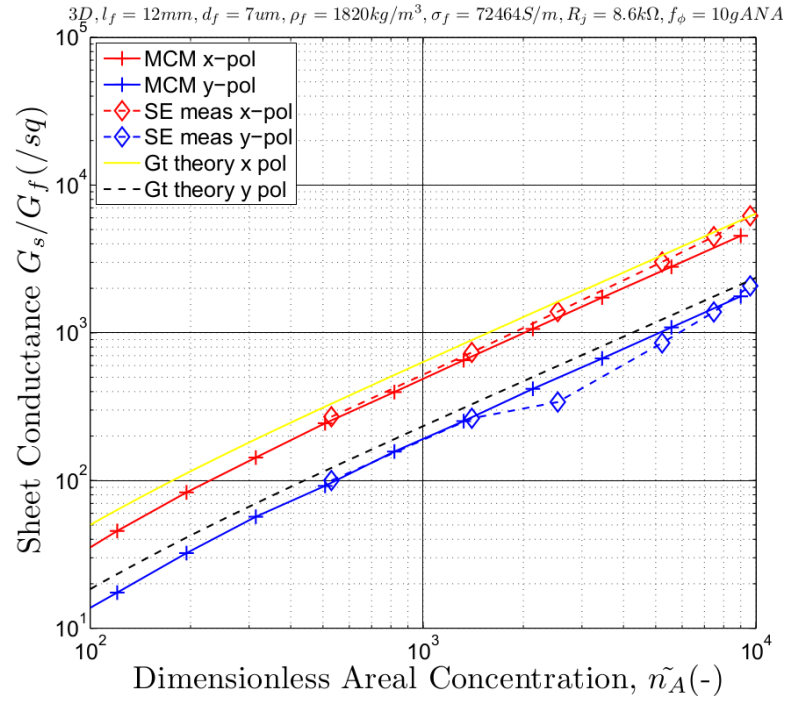


Fig. 6.16 The measured and modelled sheet conductance of real nonwoven fabrics, with an estimated contact resistance of $8.6k\Omega$

Results and Analysis

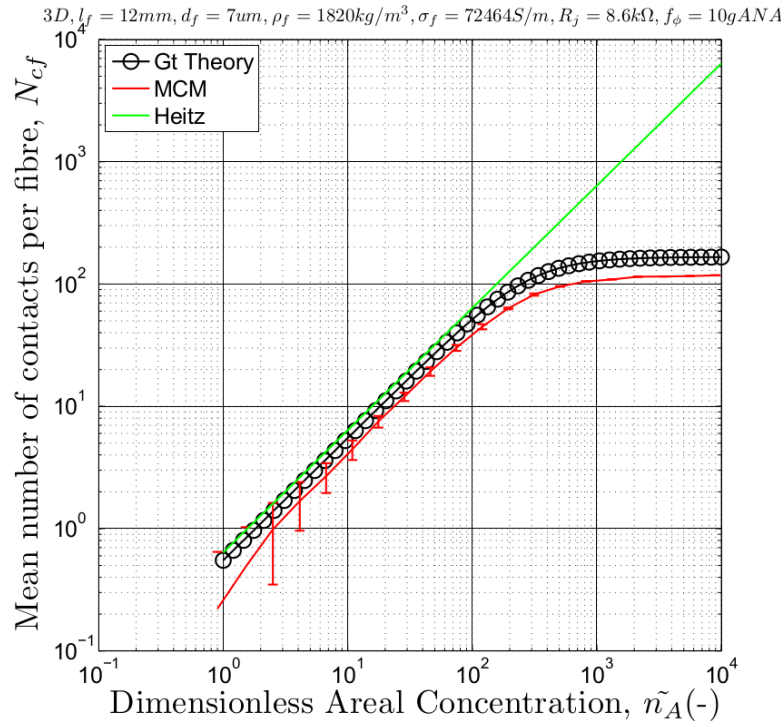


Fig. 6.17 The predicted number of contacts per fibre for a real nonwoven fabric

Figure 6.17 shows the mean number of contacts per fibre for the real fibre angle distribution. A small difference between the MCM and analytic theory can be seen, which may be explained by errors arising in the empirical fits first performed on slightly different fibre angle distributions compared to the final materials. As reported earlier, the Heitz model continues to over predict the number of contacts once the areal concentration $\tilde{n}_A > 100$ for the real material cases, which are of course 3D in nature.

As a qualitative visual comparison figure 6.18 shows an SEM image of a $25g/m^2$ carbon nonwoven fabric ($\tilde{n}_A = 400$) which shows there appears to be (approximately) 7-10 fibre contacts every millimetre of fibre. For the 12mm fibres used in this study, there should therefore be approximately 80-120 contacts, which is predicted by the MCM model's which correspond to the real materials (figure 6.17).

6.3 Sheet Conductance Models

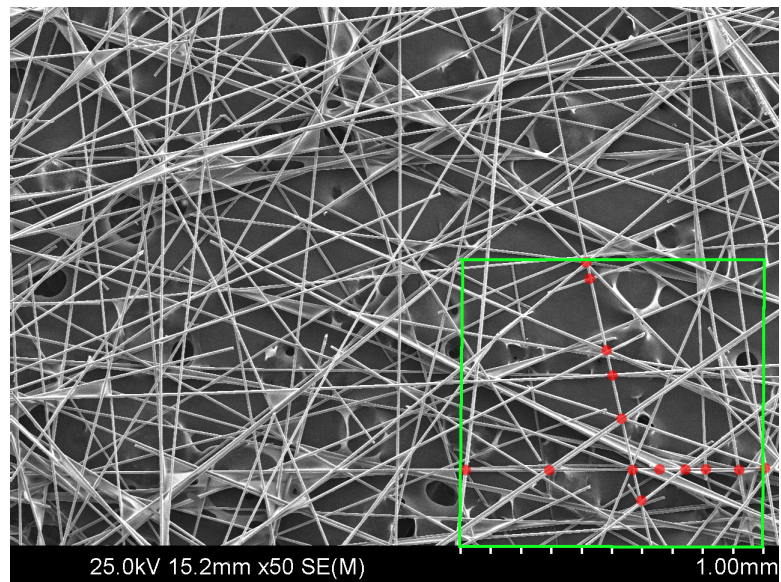


Fig. 6.18 Visual confirmation of the typical number of fibre contacts per fibre in a $25g/m^2$ carbon fabric

6.4 Shielding Effectiveness Models

This section discusses the results of the simulated radio frequency shielding effectiveness of nonwoven fabrics, completed by importing the micro-structural models into a full-wave simulation environment and comparing them to Absorber Box measurements of the shielding effectiveness. Due to the unavoidable compromise between mesh size, total simulation size and run time, these models were forced to use smaller region areas of 3x3 mm compared to the previous sheet resistance simulations. This means that these full-wave models do not take into account the inter-fibre contact resistance as most of the 12mm fibres span the problem space and the effect of inter-fibre contact resistance is negligible. For each areal weight 10 models were simulated and the mean shielding effectiveness values calculated. At the time of TLM simulation, the fibre angle distribution data was not available and so uniform distributions of fibre were used. Polarisation specific behaviour is still possible to simulate through application of the previously determined geometry factor to the shielding effectiveness values, enabling a comparison to measurement.

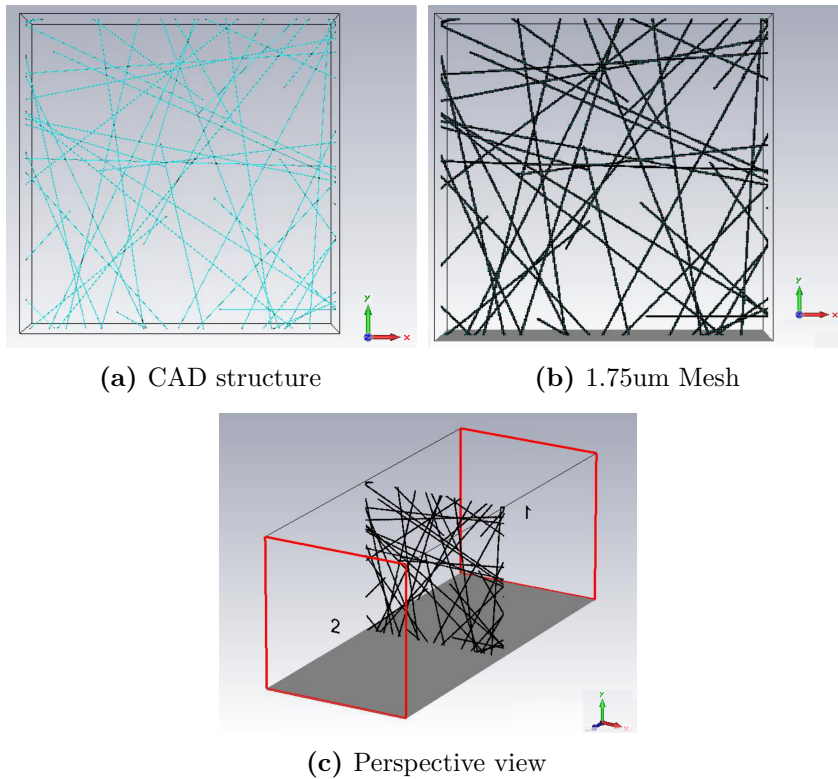


Fig. 6.19 The CAD and mesh geometries of a $4g/m^2$ carbon nonwoven

6.4 Shielding Effectiveness Models

Figure 6.19 shows the CAD and mesh structures representing a $4g/m^2$ carbon nonwoven, sample number 7 of 10. Similarly figure 6.20 shows the CAD and mesh structures representing an $18g/m^2$ carbon nonwoven, sample number 3 of 10.

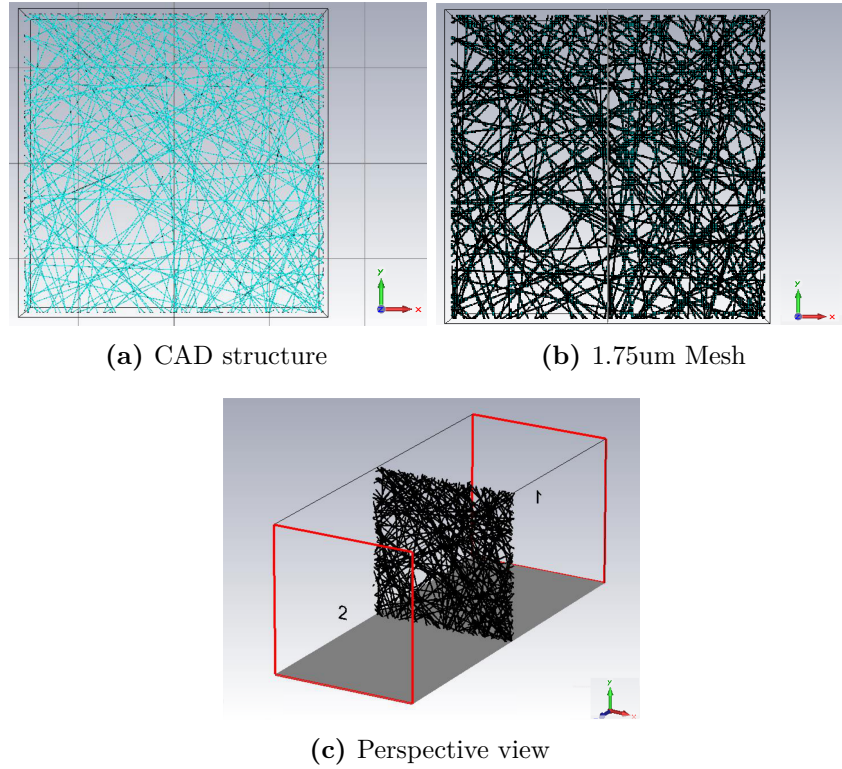


Fig. 6.20 The CAD and mesh geometries of an $18g/m^2$ carbon nonwoven

Results and Analysis

Figure 6.21 shows the time-domain waveform amplitudes obtained at each waveguide port for the $4g/m^2$ carbon nonwoven, sample 7. The incident waveform amplitudes are defined ($i1$, $i2$) as well as the transmitted ($o2,1$, $o1,2$) and reflected ($o1,1$, $o2,2$) output waveform amplitudes. This is typical for all of the simulations completed.

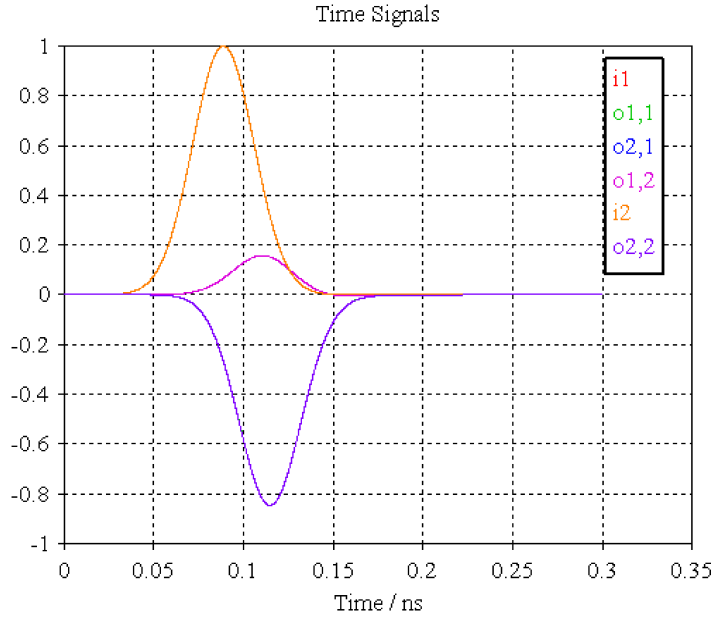


Fig. 6.21 Transmitted and reflected waveforms

For the same structure, figure 6.22 shows the loss of energy in the mesh with respect to time. The stopping criterion for the simulation of -80dB is met.

Figure 6.23 shows the shielding effectiveness of all of the simulated samples. The $4g/m^2$ models show higher variability (greater spread in the y-direction) compared to the $18g/m^2$ nonwoven fabric, due to the lower concentrations of fibre present (as discussed in 6.3.1). It is also interesting to note that the shielding effectiveness of some of the $4g/m^2$ samples is beginning to fall (slowly) from 3 GHz, indicating that the apertures within the structure are beginning to allow energy to be transmitted.

6.4 Shielding Effectiveness Models

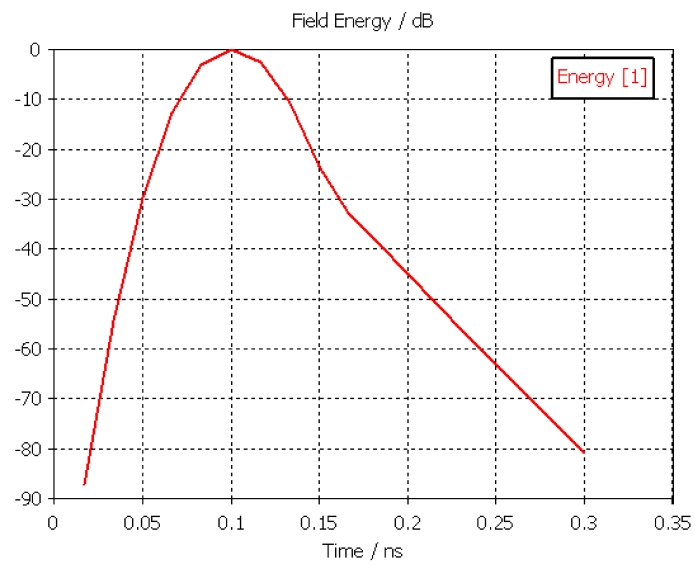
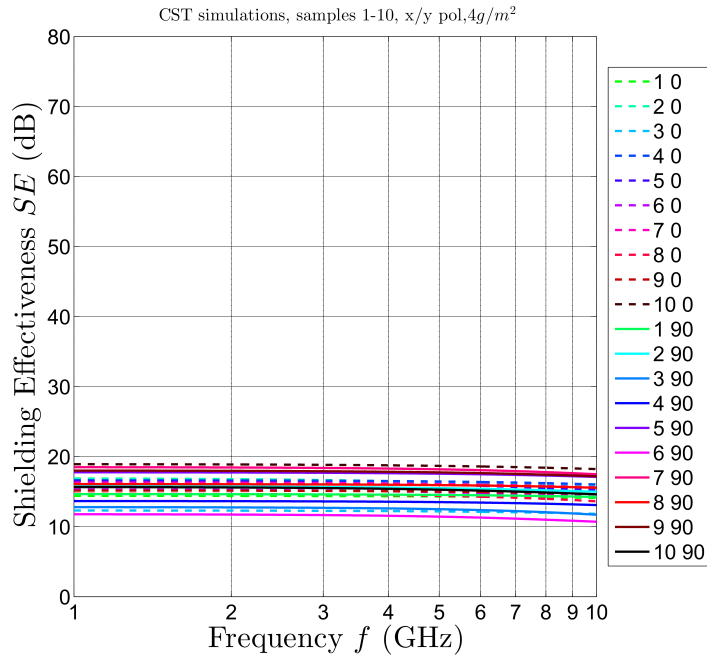
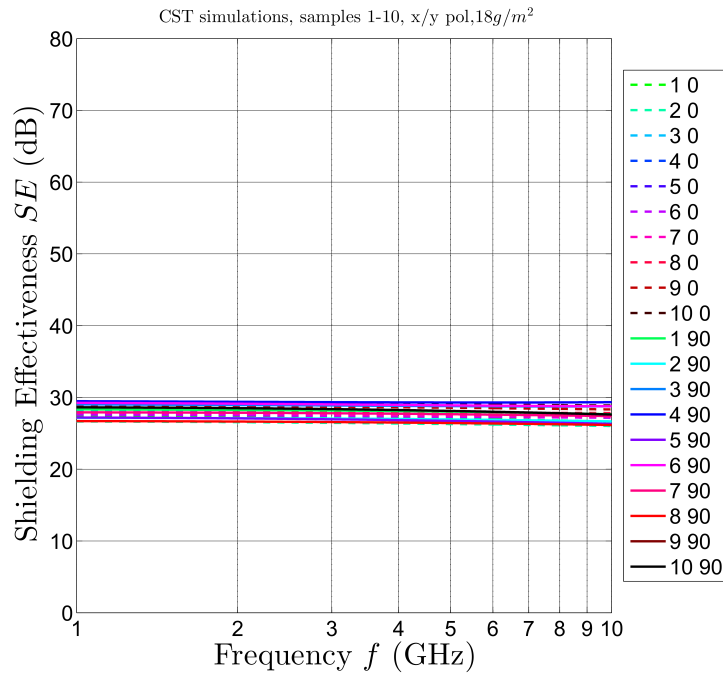


Fig. 6.22 Energy for the stopping criterion, set at -80dB

Results and Analysis



(a) CST simulated $4g/m^2$ samples

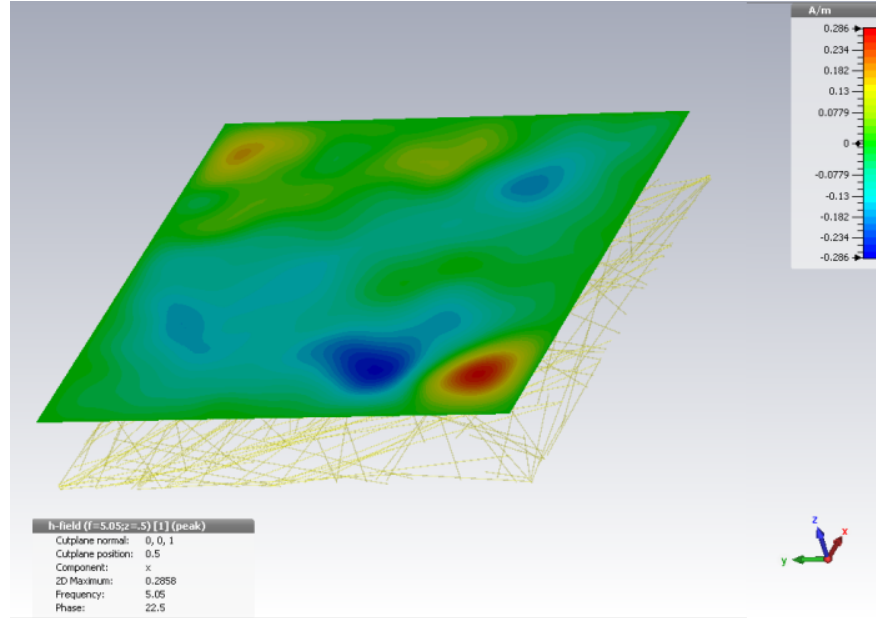


(b) CST simulated $18g/m^2$ samples

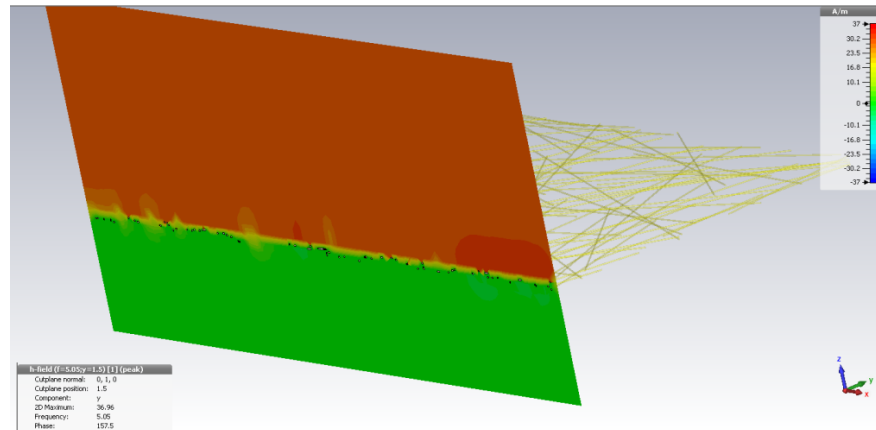
Fig. 6.23 The simulated shielding effectiveness of 10 sampled regions (for each areal weight) of carbon nonwoven fabric

6.4 Shielding Effectiveness Models

By defining field monitors, it is possible to map the spatial field strength variation caused by the materials variable local structure.



(a) The magnetic field strength 5mm above the nonwoven plane,



(b) The z-plane magnetic field, illuminated by a 5 GHz plane wave

Fig. 6.24 The magnetic field strength above and below a $4g/m^2$ nonwoven, illuminated by a 5 GHz plane wave

Results and Analysis

Figure 6.25 shows the results of the full-wave simulated shielding effectiveness versus experimental measurement. In order to make this comparison, the simulated shielding effectiveness for each sample was used to produce an average shielding effectiveness value, which was then multiplied by the corresponding geometry factors. The worst case error between the simulation and the measurement is approximately 3dB (for the x-polarisation) at 7.4 GHz. The remainder of the models are within one standard deviation of the measured values and show good agreement.

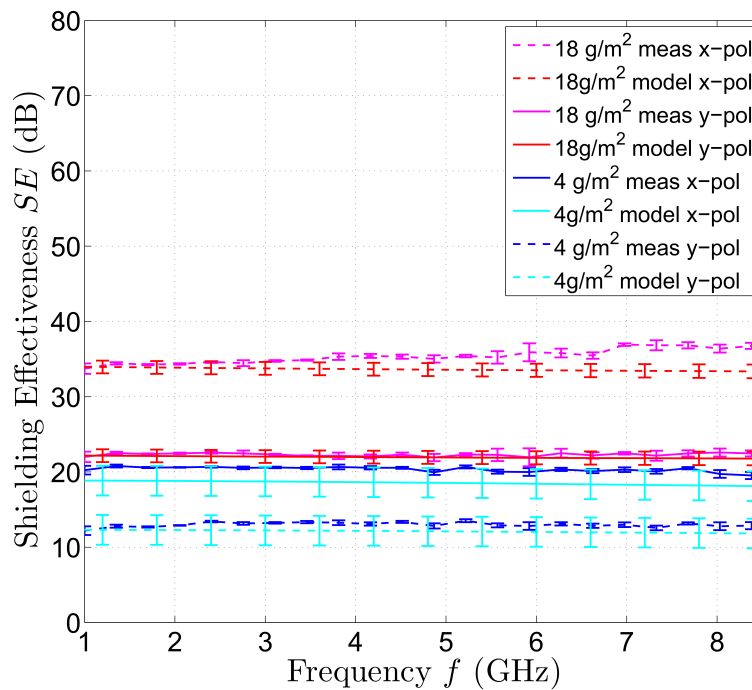


Fig. 6.25 The mean shielding effectiveness of TLM simulations, plotted with one standard deviation and comparison to mean absorber measurements

Simulation of heavier areal weight materials took considerably longer to process due to the extra mesh cells required to capture the relatively thicker micro-structures and are not included in the study due to time constraints. This remains part of a future work objective, discussed in the final chapter.

At frequencies between 1-10 GHz, the apertures within the material do not allow significant energy to couple through them, determined by the predominately flat nature of the shielding effectiveness curves. Figure 6.26 shows the shielding effectiveness of a $10\text{g}/\text{m}^2$ carbon nonwoven, with the frequency simulated up to 200 GHz.

6.4 Shielding Effectiveness Models

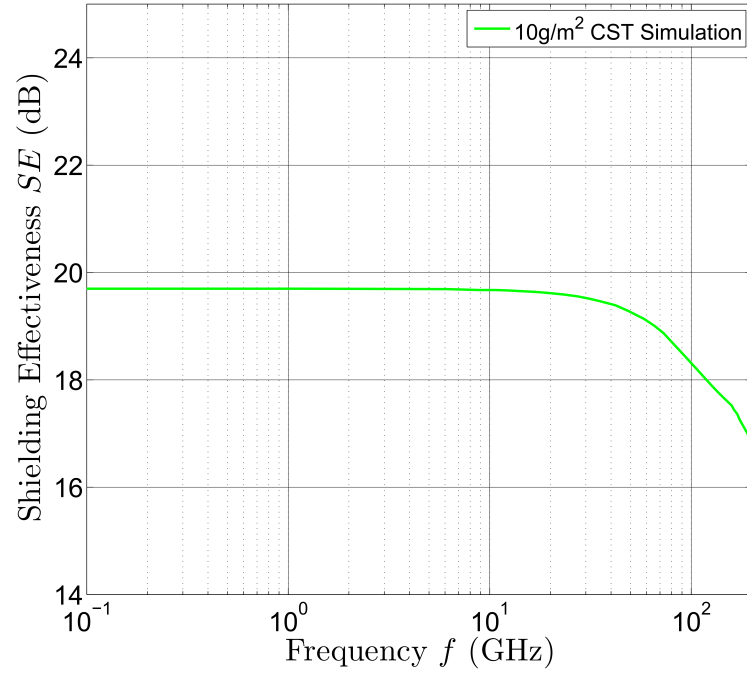


Fig. 6.26 The simulated high frequency shielding effectiveness of a $10\text{g}/\text{m}^2$ carbon nonwoven fabric (up to 200 GHz)

The simulation indicates that for this areal weight, the apertures within the structure start to allow transmission through the structure from frequencies of 20GHz. This results in approximately a 3dB reduction in the Shielding Effectiveness by 200 GHz. The predicted loss of shielding performance was theorised in chapter 2, albeit at lower frequencies and larger apertures. The aperture penetration mechanisms are also thought to be at work here, in a high frequency regime of the same phenomena.

6.5 Summary

This chapter presented and analysed the results of the micro-structure model, specifically how the structure affects the sheet conductance and shielding effectiveness. Initially the predicted percolation probabilities were introduced before a range of idealised 2D and 3D sheet conductance models were presented. The micro-structure models were used to experiment with different arbitrarily chosen fibre angle distributions (isotropic and Gaussian) as well as different fibre contact-resistance values (perfectly conducting $R_j = 0$, resistive $R_j = 1M\Omega$). The impact of these factors on the mean number of contacts per fibre were presented and the differences between the 2D and 3D cases explained. The section concluded with the modelled sheet conductance for real nonwoven fabrics which made use of the measured fibre angle distribution from chapter 5.2. By comparison to experimental measurement, the mean fibre contact-resistance was predicted to be $8.6k\Omega$.

By implementing full wave computational techniques (TLM), the radio-frequency shielding effectiveness was simulated and the results compared to experimental measurement. In order to capture the material's full variability, a number of modelled regions were simulated using a minimum region size of 3x3mm. At the required mesh size, even these small sized regions placed high computational demands and limited the results to low areal concentration materials. Finally by simulating very high frequencies (upto 200 GHz) it was possible to see the aperture penetration effects and the predicted fall in Shielding Effectiveness, arising from frequencies of 20 GHz and above.

Chapter 7

Conclusions

Conclusions

7.1 Summary

The aim of this research was to develop micro-structure models of conductive nonwoven fabrics such that their electromagnetic performance can be better predicted, optimised and understood across a range of quasi-static and radio frequency problems.

Initially, through experimental measurement the electromagnetic shielding and sheet conductance were deduced, quantifying the material's performance and providing a holistic understanding of the behaviour. It was found that at low frequencies (approximately < 2.5 GHz), Schelkunoff's theoretical expression for the SE of homogeneous conductive thin sheet materials can be reliably used to predict the material's shielding performance. This means the material can be approximated as a bulk material and the sheet conductance can be used as an indication of the low frequency shielding performance using $SE_{dB} = 45.51 - 20 \log_{10} \left(\frac{1}{R_s} \right)$. Through use of the Levenberg-Marquardt least square fitting algorithm it was possible to prove this experimentally via the correlation of quasi-static and radio frequency measurements (shown in figure 4.5).

However, the high frequency behaviour of the material is also important. To represent the high frequency electromagnetic field interaction with the nonwoven fabric, the material's micro-structure had to first be modelled. This was a challenging problem, as the material's inherent complexity, variability and stochastic nature are not trivial characteristics to recreate. Direct micro-structure meshing attempts, such as microscope imaging or x-ray tomography were briefly attempted, but weren't viable methods in this study, largely because of difficulties associated with image noise, cost and data extraction time.

Instead, an efficient Monte Carlo modelling approach was deployed. This consisted of a series of algorithms which pseudo-randomly recreate the fibre positions using particular parameters and constraints. Some parameters - such as the material's fibre angle distribution were completely unknown until a new measurement method was developed allowing the material's anisotropy to be included within the model.

The resulting micro-structural model was validated by simulating the quasi-static sheet conductance behaviour. The micro-structure was used to create an equivalent resistor network from which the solution could be compared to earlier sheet resistance measurements. Using this approach, it was possible to

7.1 Summary

predict the mean contact resistance of the fibre network $R_j = 8.6k\Omega$, as well as how the mean number of contacts per fibre varies with areal concentration and orientation. Additionally radio frequency simulations were completed in a full wave simulation package and validated against earlier shielding effectiveness measurements. In order to represent the fine fibres at sufficient resolution, a high number of mesh cells were required, limiting the area over which the material could be represented (due to computational constraints). To minimise processing times, many smaller models were simulated and the results averaged using the lower areal concentrations, corresponding to 4 and $18g/m^2$. In addition, a $10g/m^2$ carbon nonwoven fabric was also simulated up to frequencies of 200 GHz, where the effects of the apertures appear to cause the shielding effectiveness to fall, as predicted by the polarizability theory introduced in the second chapter.

Finally, 2D and 3D analytic formulations of nonwoven fabrics were created such that the sheet conductance could be predicted and compared to numerical Monte Carlo and experimental values that were previously determined. The analytic model provided insight into how specific parameters influence the sheet conductance, which can be used in future design and optimisation routines for conductive nonwoven fabrics.

To summarise, this research has delivered the following achievements relating to wet-laid nonwoven fabrics:

- Validated micro-structural models
- Experimental measurements of the sheet conductance
- Experimental measurements of the shielding effectiveness
- Test method development enabling the measurement of fibre angle distribution
- Calculation of the Geometry Factor
- Simulation of the Sheet Conductance through analytic and numerical models
- Simulation of the shielding effectiveness through semi-empiric and numeric models
- Prediction of the percolation threshold
- Prediction of the mean number of contacts per fibre

Conclusions

- Prediction of the mean contact resistance between fibres

7.2 Further Work

The experiments and models presented in this thesis have produced some useful insight into the electromagnetic properties of conductive nonwoven fabrics. Using the presented micro-structural model it is possible to explore new multi-physics paths which include; thermal, mechanical, chemical, and fluid domains. However, prior to this it is worthwhile refining certain aspects of the work and also consider some of the new questions it has raised. The following section discusses how some of these questions might be progressed as future work.

Development of Monte Carlo Models

The existing Monte Carlo model uses an assumed uniform z-plane fibre angle distribution $P(\theta)$, limited by the material's thickness. As all of the materials are relatively thin in this study compared to the fibre length, the z-plane angle is forced to be quite small: $\theta \leq 0.2^\circ$ for $4.4g/m^2$ and $\theta \leq 3^\circ$ in the case of an $84.1g/m^2$ material, which is an acceptable approximation. However for shorter fibres (or conversely thicker materials) this approximation may lead to errors. For example if 2mm fibres are considered, the range of possible fibre angles increases to $\theta \leq 1.28^\circ$ for $4.4g/m^2$ and $\theta \leq 18.75^\circ$ in the case of an $84.1g/m^2$ material of similar thickness. Similar to the in-plane fibre angle distribution $P(\phi)$ measurement, a suitable z-plane $P(\theta)$ measurement technique would need to be developed such that the real distribution could be included within the model. The technique itself is likely to be different, as fibre angles are difficult to detect in the cross-section plane.

The Monte Carlo models have enabled the mean contact resistance (G_c) to be fitted to a measured value and the mean number of contacts per fibre (N_{cf}) to be predicted. It is of interest to consider, not only the mean contact resistance, but also the form of the contact resistance distribution and its dependence on the fibre intersection angle within the network. The location of contacts is known (7.1) and this information coupled with knowledge of the associated fibres angles could be used to estimate the contact area size (one of the determinants of the contact resistance distribution). This distribution could be included within a

future model, enabling a deeper understanding of the material's response to other physical parameters.

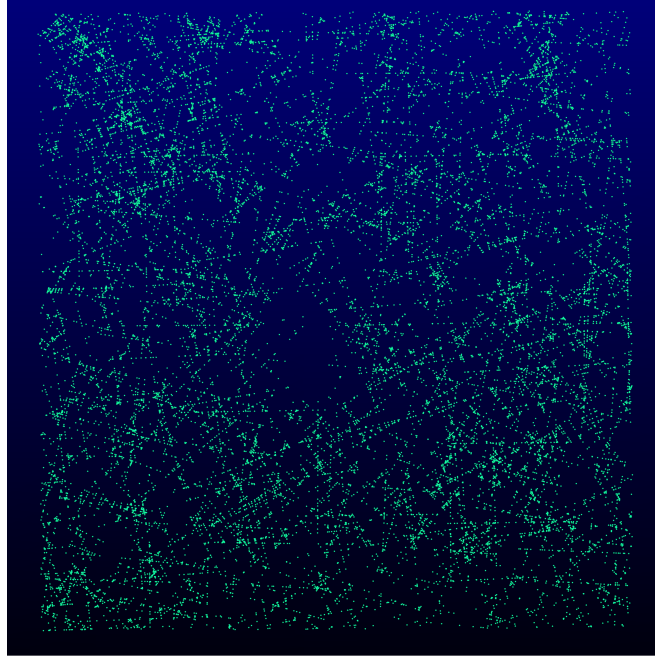


Fig. 7.1 Mapping of the contact points locations from the MCM model for an areal dimensionless concentration $\tilde{n}_A = 59$

Using the model to simulate different fibre diameters and conductivities (such as nano-fibres and metal coated fibres) is also possible and provides valuable insight when designing nonwoven fabrics of the future.

Radio Frequency Simulation

The full-wave radio frequency simulations completed thus far are not large enough to consider the effects of contact resistance, which require models to be larger than at least one fibre length. In order to achieve this, a means to improving the computational performance of the code is required. Improving computational efficiency would also enable the simulation of the higher areal weight nonwoven fabrics, as well as the response to various 3D geometries and configurations. These are all important future steps in allowing a better understanding of the material's behaviour. Figure 7.2 shows the CAD architecture of a $50g/m^2$ carbon nonwoven, which is possible to simulate, although the large number of mesh cells and long run times precluded them from this study.

Conclusions

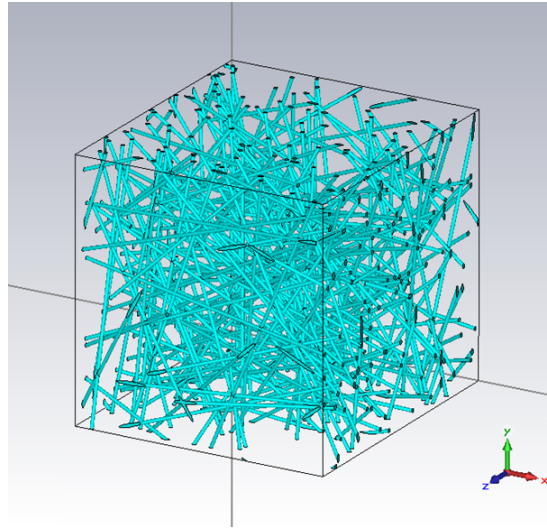


Fig. 7.2 CAD geometry of a $50\text{g}/\text{m}^2$ carbon nonwoven fabric (truncated X-Y plane)

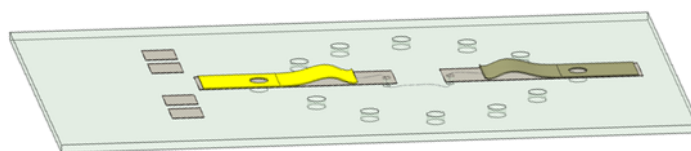
Full-wave simulation of a range of electromagnetic applications which use the nonwoven fabric's micro-structure are now also possible including; enclosure design, frequency selective surfaces (FSS), radar cross section (RCS) reduction and radar absorbent material (RAM) design.

Fibre Conductance Measurements

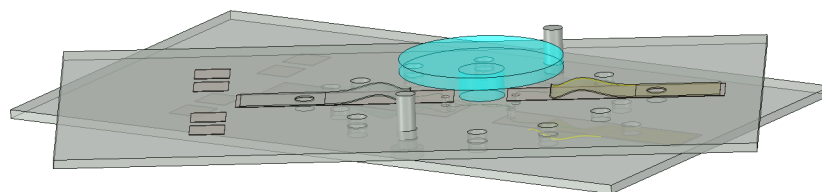
A range of experimental measurements are envisaged which would enable the direct measurement of the fibre filament conductance and inter-fibre contact resistance. A means of securing each fibre filament would be required as they are difficult to isolate and solder directly to. A contact resistance measurement jig concept is shown in figure 7.3 which could be used to determine the contact resistance between fibres at various angles and pressures.

Absorber Box (8.5 - 20 GHz)

The Absorber Box has been a crucial electromagnetic measurement technique within this study. It is of interest to extend the frequency range of the measurement system to 20 GHz and perhaps beyond, although this will be dependant on ensuring the absorber reflectivity coefficient is maintained and which may require a different specification of Eccosorb absorber.



(a) Top half of the jig with securing electrodes (gold) and 30° hole increments



(b) Both halves of jig with securing pressure plate (blue)

Fig. 7.3 A conceptual drawing showing a jig allowing for the measurement of fibre contact resistance versus angle and pressure

Appendix A

A.1 Maxwell's equations

Maxwell's equations bring together the theories of electricity and magnetism to allow for the accurate prediction of classical electromagnetic events. Fundamentally these equations show that an electric field is induced by a time varying magnetic field (A.1) and alternatively a magnetic field is induced by a time varying electric field (A.2). The electric field can also be generated by charge density ρ_c , and the magnetic field by a current source J .

$$\nabla \times \mathbf{E} = -\frac{\partial \mathbf{B}}{\partial t} \quad (\text{A.1})$$

$$\nabla \times \mathbf{H} = J + \frac{\partial \mathbf{D}}{\partial t} \quad (\text{A.2})$$

$$\nabla \cdot \mathbf{D} = \rho_c \quad (\text{A.3})$$

$$\nabla \cdot \mathbf{B} = 0 \quad (\text{A.4})$$

Where the symbols and units are defined as:

\mathbf{E} = the electric field (V/m)

\mathbf{H} = the magnetic field (A/m)

\mathbf{D} = the electric flux density (C/m^2)

\mathbf{B} = the magnetic flux density (Wb/m^2)

J = the electric current density (A/m^2)

ρ_c = the electric charge density (C/m^3)

The constitutive relationships below define how the electric and magnetic flux densities are related to the electric and magnetic fields through the electric permittivity and magnetic permeability:

$$\mathbf{D} = \epsilon \mathbf{E} \quad (\text{A.5})$$

A.1 Maxwell's equations

$$\mathbf{B} = \mu \mathbf{H} \quad (\text{A.6})$$

$$\mathbf{J}_c = \sigma \mathbf{E} \quad (\text{A.7})$$

$$\epsilon = \epsilon_0 \epsilon_r \quad (\text{A.8})$$

$$\mu = \mu_0 \mu_r \quad (\text{A.9})$$

Where the symbols and units are defined as:

ϵ = Electric permittivity (F/m)

ϵ_o = Electric permittivity of free space $8.854 \times 10^{-12}(F/m)$

ϵ_r = Relative electric permittivity (*dimensionless*)

μ = Magnetic permeability (H/m)

μ_0 = Magnetic permeability of free space $4\pi \times 10^{-7}(H/m)$

μ_r = Relative magnetic permeability (*dimensionless*)

σ = Conductivity (\mathcal{U}/m)

The electric field and its time derivative can be described in exponential form as

$$\mathbf{E}(t) = \mathbf{E}_0 e^{j\omega t} \quad (\text{A.10})$$

$$\frac{\partial}{\partial t} \mathbf{E}(t) = j\omega \mathbf{E}_0 e^{j\omega t} = j\omega \mathbf{E}(t) \quad (\text{A.11})$$

The wave equation allows for the solution of the electric or magnetic fields. To derive the wave equation (a second order differential equation) Maxwell's equations are expressed using the constitutive relations.

$$\nabla \times \mathbf{E} = -j\omega \mu \mathbf{H} \quad (\text{A.12})$$

$$\nabla \times \mathbf{H} = (\sigma + j\omega \epsilon) \mathbf{E} \quad (\text{A.13})$$

$$\nabla \cdot \mathbf{B} = 0 \quad (\text{A.14})$$

$$\nabla \cdot \mathbf{D} = 0 \quad (\text{A.15})$$

The curl of (A.12) is then taken:

$$\nabla \times \nabla \times \mathbf{E} = -j\omega\mu\nabla \times \mathbf{H} \quad (\text{A.16})$$

and equation (A.13) substituted giving:

$$\nabla \times \nabla \times \mathbf{E} = -j\omega\mu(\sigma + j\omega\epsilon)\mathbf{E} \quad (\text{A.17})$$

The identity $\nabla \times \nabla \times \mathbf{E} = -\nabla^2\mathbf{E} + \nabla(\nabla \cdot \mathbf{E})$ can then be substituted into the LHS of equation (A.17). In a charge free region $\nabla \cdot \mathbf{E} = 0$ thus;

$$\nabla^2\mathbf{E} = j\omega\mu(\sigma + j\omega\epsilon)\mathbf{E} \quad (\text{A.18})$$

The squareroot of the term $j\omega\mu(\sigma + j\omega\epsilon)$ is known as the propagation constant γ which substituted into (A.18) produces the wave equation:

$$\nabla^2\mathbf{E} = \gamma^2\mathbf{E} \quad (\text{A.19})$$

The same analysis can be repeated for the magnetic field yielding an analogous term:

$$\nabla^2\mathbf{H} = \gamma^2\mathbf{H} \quad (\text{A.20})$$

A.2 Resistance Model: Nonwoven Fabric Codes

```

1 %% Physical Fibre Properties
2 r = 3.5e-6;                % Fibre radius m
3 A = pi.*(r^2);            % Cross sectional area m2
4 L = 1.2e-2;               % Fibre length m
5 fvol = A.*L;              % Fibre volume m3
6 fdensity = 1820;          % Fibre Density kg/m3
7 fmass = fvol*fdensity;    % Fibre Mass
8
9 %% Electrical Properties
10 p =1.38e-5;              %4e-5          % Fibre resistivity ohms-m
11 sigma = 1/p;             % Fibre conductivity s/m
12 R = (p.*L)./(A);         % Resistance per fibre ohms
13
14 %% Physical Sheet Properties
15
16 % Sheet Volume (m3) of 4.47e-5 x 10cm x 10cm
17 sheet_vol = (4.47e-5)*(1e-1)*(1e-1);
18
19 % Binder reduced mass 4.47e-5 x 10cm x 10cm (kg)
20 sheet_mass = 4.18e-5;
21
22 % Areal weight- Binder reduced mass(kg/m2)
23 areal_weight = 4.18e-3;
24
25 fnum = sheet_mass/fmass;  % No of fibres
26 fvf = (fnum*fvol)./(sheet_vol.*100); % Fibre Volume Fraction
27 vvf = 100-fvf;           % Void Volume Fraction
28
29
30 %% Define Fibre Distribution Function and Solve for Sheet
31 conductance G.
32 %% Electrical Sheet Properties - ANALYTIC uniform fibre distribution
33 G_analytic_Uniform_analytic = (1/2)*sigma*areal_weight/(fdensity);
34 % Material Sheet Conductivity (uniform angular spread)
35 Rs_analytic_Uniform_analytic = 1/G_analytic_Uniform_analytic
36 % Material Sheet Resistance
37
38 %% Electrical Sheet Properties -NUMERIC uniform fibre distribution
39 %MD

```

```

39 y1_MDuni=@(x) (1./pi).* (cos(x).^2);
    % Matlab numerical func.
40 Q1_MDuni=quadgk(y1_MDuni,-90*(pi/180),90*(pi/180));
    %Integration quad function
41 G_numeric_Uniform_MD =sigma*areal_weight/(fdensity).*Q1_MDuni ;
42 Rs_numeric_Uniform_MD = 1/G_numeric_Uniform_MD
43
44 %CD should be same as MD unifrom fibre distribution
45 y1_CDuni=@(x) (1./pi).* (sin(x).^2);
46 Q1_CDuni=quadgk(y1_CDuni,0*(pi/180),180*(pi/180));
    %Integration quad function
47 G_numeric_Uniform_CD =sigma*areal_weight/(fdensity).*Q1_CDuni ;
48 Rs_numeric_Uniform_CD = 1/G_numeric_Uniform_CD
49
50
51 %% Electrical Sheet Properties -
52 %NUMERIC & measured Fitted Double Gaussian distribution)
53 a1=40.33*pi/180;
54 b1=-0.003283*pi/180;
55 c1=12.98*pi/180;
56 a2=12.86*pi/180;
57 b2=-38.71*pi/180;
58 c2=184.6*pi/180;
59
60 % MD integral G calc
61 y2_MD=@(x) (a1.*exp(-(x-b1)./c1).^2)+
62 a2.*exp(-(x-b2)./c2).^2).* (cos(x).^2);
63 Q2_MD=quadgk(y2_MD,-90*(pi/180),90*(pi/180));
64 G_numeric_dgaussian_MD=sigma*areal_weight/(fdensity).*Q2_MD;
65 Rs_numeric_dgaussian_MD=1/G_numeric_dgaussian_MD
66
67
68 % CD integral G calc - RS should be different due to alignment
69 y2_CD=@(x) (a1.*exp(-(x-b1)./c1).^2)
70 +a2.*exp(-(x-b2)./c2).^2).* (sin(x).^2);
71 Q2_CD=quadgk(y2_CD,0*(pi/180),180*(pi/180));
72 G_numeric_dgaussian_CD=sigma*areal_weight/(fdensity).*Q2_CD;
73 Rs_numeric_dgaussian_CD=1/G_numeric_dgaussian_CD

```

A.3 Planar Metal Shielding (Schelkunoff) Codes

```

1  % Schelkunoff Model
2
3  % EM constants
4  mu0=1.2566e-06;
5  eps0=8.854e-12;
6  Z0=sqrt(mu0/eps0);
7  c0=1/sqrt(mu0*eps0);
8  GHz=1e9
9  %x=linspace(1e3,1e10,1e5);      %frequency range
10  x=logspace(1,10,30);
11  % Material Parameters
12  epsr=1;
13  mur=1;
14  sigma=[6.21e7 5.8e7 3.54e7 2.5e6 7.2464e4];
15  t=[1e-5];
16
17  % Schelkunoff functions - nested loop for sigma and t
18  for i=1:numel(sigma)
19      U(:,i)=sqrt((j*2*pi*x*epsr*eps0+sigma(1,i)).*(j*2*pi*x*mur*mu0));
20      Zm(:,i)=sqrt((j*2*pi*x*mur*mu0)./(j*2*pi*x*epsr*eps0+sigma(:,i)));
21      P(:,i)=(Zm(:,i)-Z0)./(Zm(:,i)+Z0);
22
23  for k=1:numel(t);
24      S21(:,i,k)=((1-P(:,i).^2).*exp(-U(:,i).*t(1,k))
25      ./ (1-(P(:,i).*exp(-U(:,i).*t(1,k))).^2));
26      se(:,i,k)=1./S21(:,i,k);
27      SE(:,i,k)=20.*log10(abs(se(:,i,k)));
28  end
29 end
30
31 %Plot functions
32 semilogx (x,SE(:,1),'-c','linewidth',2,'markersize',14);
33 hold on;
34 semilogx (x,SE(:,2),'-r','linewidth',2,'markersize',14);
35 semilogx (x,SE(:,3),'-go','linewidth',2,'markersize',14);
36 semilogx (x,SE(:,4),'-bd','linewidth',2,'markersize',14);
37 semilogx (x,SE(:,5),'-m>','linewidth',2,'markersize',14);
38 % Plot format
39 c={'Silver','Copper','Aluminium','Titanium','Carbon'};
40 %set(gca,'XTick',[1:1e10:1e10],'color','k')

```

```
41 set(gca,'fontsize',22)
42 set(gca,'TickDir','out');
43 set(gca,'LooseInset',get(gca,'TightInset'));
44 set(gca,'GridLineStyle','-')
45 grid on;
46 axis([1e5,1e10,0,300]);
```

A.4 Absorber Box Data Codes

```

1 % Load data files
2 load('variables_a1_a13.mat')
3 % Load data files
4
5 % Reference frequency data and units
6 f=a1(:,1);
7
8 % Define frequency units
9 GHz=1e9;
10
11 % Specify real+imaginary S21 data & put in matrix 1x13
12 for i = 1:13
13     real = eval(['a', int2str(i), '(:,4)']);
14     imag = j * eval(['a', int2str(i), '(:, 5)']);
15     S21Matrix(:,i)= real + imag;
16 end
17
18 %Convert from dB S21=20*log10(abs(a13(:,4)));
19 LogAbsS21Matrix=20*log10(abs(S21Matrix));
20
21 %DownSample every 20 points
22 LogAbsS21MatrixDS=LogAbsS21Matrix(1:20:end,1:13);
23 fDS=f(1:20:end,1);
24
25 % Loop plot instruction and reference plot styles for each line
26 figure(1);
27 for i=1:1:13
28     plot(fDS/GHz,LogAbsS21MatrixDS(:,i),plotstyle{i,:})
29     hold on
30 end
31
32 %Define SEref from Analytic
33 SEref=((115.5-20*log10(f/1e6))); % in dB
34
35 %Define calibration factor k
36 k=10.^(SEref./20).*S21Matrix(:,13);
37
38
39 % Compute SE for S21 matrix
40 for x=1:13

```



```

41     SeMatrix(:,x)=k./S21Matrix(:,x);
42 end
43
44 LogAbsSeMatrix = 20.*log10(abs(SeMatrix));
45
46 %DownSample every 20 points
47 LogAbsSeMatrixDS=LogAbsSeMatrix(1:50:end,1:12);
48 fDS=f(1:50:end,1);
49
50 % Loop plot instruction
51 figure (2);
52 %figure('units','normalized','outerposition',[0 0 1 1]);
53
54 for i=1:1:12
55     semilogx(fDS/GHz,LogAbsSeMatrixDS(:,13-i),plotstyle{13-i,:})
56     hold on
57 end

```

A.5 Fibre Angle Distribution Codes

```

1 % Calculate line weighted PDF and Geometry factor
2
3 N = 1
4 images = cell(1,N);
5 %N = dir('*.png');
6 N=dir(fullfile([pwd '\BW_images\*.png']));
7
8 IMAGES = cell(1,numel(N));
9 for i = 1:numel(N)
10 IMAGES{i} = imread(N(i).name); %make sure BW_images is added to path
11 end
12
13
14 % Name Cell
15 bw = cell(1,numel(N));
16
17 % Loop for image processing
18 for i=1:numel(N)
19     % Binary image
20     bw{i}=IMAGES{i}; % bw{i} = im2bw(IMAGES{i},0.4);
21     % Invert BW image
22     BW{i} = imcomplement(bw{i});
23
24     % Hough Transfrom
25     theta=-89.5:2:89.5; % theta resolution to search over
26     [H,T,R] = hough(BW{i}, 'RhoResolution',1, 'Theta',theta);
27     P = houghpeaks(H,100, 'threshold',ceil(0.9*max(H(:))));
28     x = T(P(:,2)); y = R(P(:,1));
29     lines{i} = houghlines(BW{i},T,R,P, 'FillGap',20, 'MinLength',500);
30     % Define lines
31     figure(i);
32     clf ; %
33     imshow(BW{i});
34     hold on
35     max_len = 0;
36
37 %format plots
38 plotcols=['b';'g';'r';'c';'m';'y'];
39 set (0, 'DefaultFigureWindowStyle','Docked');
40 set(gca, 'LooseInset',get(gca, 'TightInset'));

```

```

40
41
42 for k = 1:length(lines{i});
43     xy{i} = [lines{i}(k).point1; lines{i}(k).point2];
44     plotcol=plotcols(1+mod(k,size(plotcols,1))); %
45     plot(xy{i}(:,1),xy{i}(:,2),plotcol,'LineWidth',2); %
46     len(k,i)=norm(lines{i}(k).point1 - lines{i}(k).point2);
47 end
48
49 saveas(figure(i),[pwd 'fibres_identified' num2str(i)], 'fig');
50
51 end
52 S=cell2mat(lines);
53 a=cell2mat({S(:).theta})';
54
55 lenrow = reshape(len,1,[]).';
56 lenrow(lenrow == 0) = [];
57
58 angleleng(:,1)=lenrow;
59 angleleng(:,2)=a;
60
61 %delete rows with image edges found
62 angleleng(angleleng == 2591,:)=[];
63 angleleng(angleleng == 1943,:)=[];
64
65 lenrow2=angleleng(:,1);
66 a2=angleleng(:,2);
67
68 auniq=unique(a2);
69 %bins=numel(auniq);
70
71 % Choose number of bins in Histogram
72 HoughThresholdvalue=0.9;
73 bins=90;
74 binwidth=180/bins;
75 theta2=[0.5+(-89.5:180/bins:90)]; % generate theta range
76
77 % calculate weighted PDF
78 PDF=lenrow2./(sum(lenrow2)*binwidth);
79 wPDF=histwc(a2,PDF,bins);
80
81 %% Plotting of wPDF - cftool used
82
83 figure(201)

```

A.5 Fibre Angle Distribution Codes

```
84 bar(theta2,wPDF)
85 set(gca,'XTick',[-90:15:90])
86 %title ('Fiber Orientation analysis, number of bins is %d', bins);
87 str=sprintf('Fiber Orientation analysis, number of bins = %g,...
88 hough threshold = %g', bins, HoughThresholdvalue);
89 title(str)
90
91 xlabel ('Fibre Orientation \theta (degrees)')
92 ylabel ('p(\theta) (weighted by line length)')
93 grid on
94 saveas(figure(201),'wPDF','fig')
95
96 save ('angleleng');
97 save ('wPDF');
98 save ('theta2');
```

A.6 Geometry Factor Codes

```

1 % Solve phi using quadgk integral
2
3
4     a1=      0.01284 ;% (0.01183, 0.01385)
5     b1 =     -1.347 ;% (-2.079, -0.6155)
6     c1 =      12.99 ;% (11.71, 14.28)
7     a2 =     0.005853 ;% (0.005191, 0.006514)
8     b2 =     -17.1 ;% (-22.13, -12.07)
9     c2 =      75.45 ;% (66.32, 84.58)
10
11
12 %wPDF
13 f = @(x) a1*exp(-(x-b1)/c1).^2) + a2*exp(-(x-b2)/c2).^2);
14
15 y1 =@(x) f(x).*(cos(x*pi/180).^2);
16 y2 =@(x) f(x).*(cos((x-90)*pi/180).^2);
17
18 % Geometry Factors
19 Q1_dgaussian=quadgk(y2,-90,90)      % 0 degree value
20 Q2_dgaussian=quadgk(y1,-90,90)      % 90 degree value
21
22 Q1_dgaussian+Q2_dgaussian

1 %Calculate Phi directly using normalised length at each angle
2
3 for j=1:length(angleleng);
4 phi0(:,j)=(1./sum(lenrow2(:,1))).*sum(lenrow2(j)...
5 .* (cos(a2(j)*(pi/180)).^2));
6 end
7
8 for j=1:length(angleleng);
9 phi90(:,j)=(1./sum(lenrow2(:,1))).*sum(lenrow2(j)...
10 .* (cos(a2(j)*(pi/180)+(pi/2)).^2));
11 end
12
13 Phi0_direct =sum (phi0)
14 Phi90_direct =sum (phi90)
15
16 Phi0_direct+Phi90_direct

```

Nomenclature

Greek Symbols

α Attenuation Constant

β Phase Constant

δ Skin Depth

ϵ Electric Permittivity

η Impedance

Γ Reflection Coefficient

γ Propagation Constant

λ Wavelength

μ Magnetic Permeability

ω Angular Frequency

Φ Geometry Factor

ρ_a Areal Weight

ρ_f Fibre Density

σ Electric Conductivity

Nomenclature

\tilde{n}_A	Dimensionless Areal Concentration
\tilde{t}	Thickness in fibre Diameters
A_f	Fibre Cross Sectional Area
c	Speed of Light in a Vacuum
d_f	Fibre Diameter
E	Electric Field
f	Frequency
G_c	Mean Inter-fibre Contact Conductance
G_f	Fibre Conductance
G_s	Sheet Conductance
H	Magnetic Field
k_e	Effectiveness of a Fibre-Fibre Contact
l_f	Fibre Length
M	Magnetic Polarizability
m_f	Fibre Mass
n_A	Areal Concentration
N_{cf}	Number of Contacts
n_c	Percolation Threshold
N_f	Number of Fibres
P	Electric Polarizability
$P(\phi)$	X-Y Plane Probability Density Function

Nomenclature

$P(\theta)$ Z Plane Probability Density Function

P_{Cont} Mean Fibre Contact Probability

P_x Percolation Probability

R_j Mean Inter-fibre Contact Resistance

R_s Sheet Resistance

T Transmission Coefficient

Y_t Transfer Admittance

Z_s Sheet Impedance

Z_t Transfer Impedance

Acronyms / Abbreviations

AC Alternating Current

CAD Computer Aided Design

CEM Computational Electromagnetic Modelling

CST Computer Simulation Technology

DC Direct Current

EMC Electromagnetic Compatibility

EMI Electromagnetic Interference

FSS Frequency Selective Materials

LO Low Observability

LOI Loss On Ignition

MCM Monte Carlo Model

Nomenclature

NRC Nested Reverberation Chamber

PAN polyacrylonitrile

PDF Probability Density Function

PET polyethylene terephthalate

RAM Radar Absorbent Materials

S – Parameters Scattering Parameters

SCN Symmetrical Condensed Node

SE Shielding Effectiveness

SEM Scanning Electron Microscope

SMA Sub-miniature version A

SPICE Simulation Program with Integrated Circuit Emphasis

TLM Transmission Line Matrix

References

- [1] M. Cropper, "<http://www.cropper.com/>," 2015.
- [2] M. Schlechter, "EMI/RFI: Materials and technologies," tech. rep., BCC Research, 2014.
- [3] M. Ashby, "Technology of the 1990s: Advanced materials and predictive design," *Philosophical Transactions of the Royal Society of London*, vol. A322, pp. 393–407, 1987.
- [4] G. Denny, "Radar resolution in masonry," www.web.onetel.net.uk/gd/thesis/NDT/basics.htm, vol. 1, 2001.
- [5] J. F. Dawson and A. C. Marvin, *Advanced EMC Measurements Course Notes*, vol. 1. York EMC Services, 2011.
- [6] C. A. Balanis, *Antenna Theory*. John Wiley & Sons, 1997.
- [7] D. Morgan, *A Handbook for EMC Testing and Measurement*. The Institution of Engineering and Technology, 2007.
- [8] S. A. Schelkunoff, *Electromagnetic waves*. D. Van Nostrand Company, 1943.
- [9] R. Schulz and V. C. Plantz, "Shielding theory and practice," *IEEE Transactions on EMC*, vol. 30: No 3, p. 187, 1988.
- [10] J. Kraus, *Electromagnetics*. Mcgraw-Hill College, 1992.
- [11] M. Damore, D. Lampasi, M. Sarto, A. Tamburrano, V. D. Santis, and M. Feliziani, "Optimal design of multifunctional transparent shields against radio frequency electromagnetic fields," *Electromagnetic Compatibility Symposium Adelaide*, vol. 1, pp. 81–86, 2009.
- [12] C. R. Paul, *Introduction to Electromagnetic Compatability*. John Wiley & Sons, 2006.
- [13] H. Ott, *Noise reduction techniques in electronics systems*. Wiley, 2nd edition, 1988.
- [14] H. Kaden, *Wirbelstromme und Schirmung in der Nachrichtentechnik*. Springer-Verlag Berlin, 1959.
- [15] J. C. G. Field, "An introduction to electromagnetic screening theory," *IEEE Colloquium on shielding and screening*, vol. 2, pp. 1/1–1/15, November 1983.

References

- [16] M. P. Robinson, T. M. Benson, C. Christopoulos, J. F. Dawson, M. D. Ganley, A. C. Marvin, S. J. Porter, and D. W. P. Thomas, "Analytical formulation for the shielding effectiveness of enclosures with apertures," *IEEE Transaction on Electromagnetic Compatibility*, vol. 40: No 3, pp. 240 – 248, 1998.
- [17] H. A. Bethe, "Theory of diffraction by small holes," *The Physical Review*, vol. 66, pp. 163 – 182, 1944.
- [18] C. J. Bouwkamp, "Diffraction theory," *Reports on Progress in Physics*, vol. 17, p. 34, 1954.
- [19] S. B. Cohn, "Determination of aperture parameters by electrolytic-tank measurements," *Proceeding of the I.R.E.*, vol. 1, pp. 1416–1451, 1951.
- [20] F. Meulenaere and J. V. Bladel, "Polarizability of some small apertures," *IEEE Transactions on Antennas and Propagation*, vol. AP-25, pp. 198 – 205, 1977.
- [21] E. Okon and R. F. Harrington, "The polarizabilities of electrically small apertures of arbitrary shape," *IEEE Transactions on Electromagnetic Compatibility*, vol. 23: No 4, pp. 359 – 366, 1981.
- [22] V. I. Fabrikant, "Electrical polarizability of small appertures: analytical approach," *International Journal of Electronics*, vol. 62, pp. 533–545, 1987.
- [23] G. Abajo, "Light transmission through a single cylindrical hole in a metallic film," *Optics Express*, vol. 10, p. 1475, 2002.
- [24] B. Hou, Z. H. Hang, W. Weijia, C. T. Chan, and P. Sheng, "Microwave transmission through metallic hole arrays: Surface electric field measurements," *Applied Physics Letters*, vol. 89, pp. 131917 – 131917–3, Sept. 2006.
- [25] I. Chremmos, "Tutorial view of electromagnetic wave diffraction through small apertures based on energy considerations," *Electromagnetics*, vol. 31, pp. 385 – 403, 2011.
- [26] E. F. Vance and K. F. Casey, "Electomagnetic pulse coupling through cable shields," *IEEE Transactions on Antennas and Propagation*, vol. AP-26: No 1, pp. 100 – 106, 1978.
- [27] K. Casey, "Electromagnetic shielding behavior of wire-mesh screens," *IEEE Transations on Electromagnetic compatibility*, vol. 30, no. 3, pp. 298–306, 1988.
- [28] F. M. Tesche, M. V. Ianoz, and T. Karlsson, *EMC Analysis Methods and Computational Models*. John Wiley & Sons, 1997.
- [29] I. D. Flintoft, "Notes of aperture macro-models," tech. rep., University of York, 2013.
- [30] J. Paul, C. Christopoulos, and D. W. P. Thomas, "Time-domain modeling of electromagnetic wave interaction with thin-wires using tlm," *IEEE Transaction on Electromagnetic Compatibility*, vol. 47: No 3, pp. 447 – 455, 2005.

References

- [31] P. Johns, “Numerical solution of 2-dimensional scattering problems using a transmission line matrix,” *Proceedings of IEE*, vol. 118: No 9, pp. 1203 – 1208, 1971.
- [32] G. Kron, “Equivalent circuit of the field equations of Maxwell,” *Proceedings of the IRE*, vol. 32 issue 5, pp. 289 – 299, 1944.
- [33] P. Johns, “A symmetrical condensed node for the TLM method,” *IEEE Transactions on Microwave Theory and Techniques*, vol. 35, No 4, pp. 370 – 377, 1987.
- [34] J. F. Dawson, “Time domain computational electromagnetics,” tech. rep., University of York, 2003.
- [35] C. Christopoulos, *The Transmission-Line Modeling Method In Electromagnetics*. Morgan and Claypool Publishers, 2006.
- [36] C. Holloway, “Using nested reverberation chambers to determine the shielding effectiveness of a material,” tech. rep., University of Colorado, 2007.
- [37] A. Einstein, *Investigations on the theory of the Brownian movement*. Dover Publications, 1926.
- [38] Toho Tenax, “Tenax chopped carbon fibers,” tech. rep., Toho Tenax America, Inc, 2011.
- [39] Hexion, “WD-30 technical datasheet,” tech. rep., Hexion Inc, 2015.
- [40] E. Fitzer, *Carbon Fibers Filaments and Composites*. Springer, 1990.
- [41] X. Huang, “Fabrication and properties of carbon fibers,” *Materials*, vol. 2, pp. 2369–2403, 2009.
- [42] H. Giesche, “Mercury porosimetry: A general practical overview,” *Particle and Particle Systems Characterisation*, vol. 23, pp. 9–19, 2006.
- [43] P. A. Webb, “Data collection, reduction and presentation,” *Micromeritics*, vol. 1, pp. 1–17, 1993.
- [44] J. Bowen, “Density and porosity measurement techniques,” tech. rep., University of Birmingham, 2012.
- [45] G. C. Rutledge, J. L. Lowery, and C.-L. Pai, “Characterization by mercury porosimetry of nonwoven fiber media with deformation,” *Journal of Engineered Fibers and Fabrics*, vol. 4, pp. 1–13, 2009.
- [46] J. Heitz, Y. Leroy, L. Hebrard, and C. Lallement, “Theoretical characterization of the topology of connected carbon nanotubes in random networks,” *Nanotechnology*, vol. 22, pp. 1–7, 2011.
- [47] V. E. Gul, *Structure and properties of conducting polymer composites*. CRC Press, 1996.

References

- [48] Y. Kim, K. J. An, K. S. Suh, H. Choi, J. Kwon, Y. Chung, W. N. Kim, A. Lee, J. Choi, and H. G. Yoon, "Hybridization of oxidized mwnt and silver powder in polyurethane matrix for electromagnetic interference shielding application," *IEEE Transactions on Electromagnetic Compatibility*, vol. 47: No 4, pp. 872 – 879, 2005.
- [49] R. H. Norman, *Conductive rubbers and plastics: Their production, application and test methods*. New York Elsevier, 1970.
- [50] A. Malliaris and D. T. Turner, "Influence of particle size on the electrical resistivity of compacted mixtures of polymeric and metallic powders," *Journal of Applied Physics*, vol. 42,2, pp. 614–618, 1971.
- [51] M. Zezelj and I. Stankovic, "From percolating to dense random stick networks: Conductivity model investigation," *Physical Review B*, vol. 86, pp. 134202,1–6, 2012.
- [52] G. E. Pike and C. H. Seager, "Percolation and conductivity: A computer study," *Physical Review B*, vol. 10,4, pp. 1410–1434, 1974.
- [53] I. Balberg, N. Binenbaum, and C. H. Anderson, "Critical behaviour of the two-dimensional sticks system," *Physical Review Letters*, vol. 51, pp. 1605–1468, 1983.
- [54] S. Kirkpatrick, "Percolation and conduction," *Review of Modern Physics*, vol. 45, 4, pp. 574–588, 1973.
- [55] R. Mutiso, M. C. Sherrott, A. Rathmell, B. J. Wiley, and K. I. Winey, "Integrating simulations and experiments to predict sheet resistance and optical transmittance in nanowire films for transparent conductors," *ACS Nano*, vol. 7-9, pp. 7654–7663, 2013.
- [56] F. Du, J. E. Fischer, and K. I. Winey, "Effect of nanotube alignment on percolation conductivity in carbon nanotube/polymer composites," *Physical Review B*, vol. 72, pp. 121404,1–4, 2005.
- [57] L. Hu, D. S. Hecht, and G. Gruner, "Percolation in transparent and conducting carbon nanotube networks," *Nano Letters*, vol. 4, No 12, pp. 2513–2517, 2004.
- [58] P. Koblinski and F. Cleri, "Contact resistance in percolating networks," *Physical Review B*, vol. 69, pp. 184201,1–4, 2004.
- [59] J. Li and S. Zhang, "Conductivity exponents in stick percolation," *Physical Review*, vol. E81, pp. 021120–1 – 021120–5, 2010.
- [60] I. Balberg, "Percolation thresholds in the three-dimensional sticks system," *Physical Review Letters*, vol. 52, pp. 1465–1468, 1984.
- [61] S. Cohen, "Contact resistance and methods for its determination," *Thin Solid Films*, vol. 104, pp. 361–379, 1983.
- [62] L. J. van der Pauw, "A method of measuring specific resistivity and Hall effect of discs of arbitrary shape," *Philips Research Reports*, vol. 13, pp. 1–9, 1958.

References

- [63] Delcom, “<http://www.delcominst.com/technology.html>,” 2016.
- [64] A. C. Marvin, L. Dawson, I. D. Flintoft, and J. F. Dawson, “A method for the measurement of shielding effectiveness of planar samples requiring no sample edge preparation or contact,” *IEEE Transactions on Electromagnetic Compatibility*, vol. 51, pp. 255 – 262, 2009.
- [65] M. Lourakis, “A brief description of the Levenberg-Marquardt algorithm,” *Institute of Computer Science, Foundation for Research and Technology, Hellas*, vol. 1, pp. 1–6, 2005.
- [66] “ASTM D4935 standard test method for measuring the electromagnetic shielding effectiveness of planar materials,” *ASTM International*, vol. 1, pp. 1–11, 2010.
- [67] I. D. Flintoft, “A review of Absorber Box calibration standard,” tech. rep., University of York, 2013.
- [68] R. O. Duda and P. E. Hart, “Use of the Hough transformation to detect lines and curves in pictures,” *Communications the Association of Computing Machinery*, vol. 15, pp. 11–15, 1972.
- [69] M. Lai, “<http://stackoverflow.com/questions/4709725/explain-hough-transformation>,” 2013.
- [70] A. N. Austin, J. F. Dawson, I. D. Flintoft, and A. C. Marvin, “Modelling the micro-structure of non-uniform conductive non-woven fabrics,” *EMC Europe Dresden*, 2015.
- [71] MATLAB, “Matlab - the language of technical computing,” The MathWorks, Inc., Natick, Massachusetts, January 2016.
- [72] C. Geuzaine and J. Remacle, “Gmsh: a three-dimensional finite element mesh generator with built-in pre- and post-processing facilities,” *International Journal for Numerical Methods in Engineering*, vol. 79, pp. 1309–1331, 2009.
- [73] L. W. Nagel, “Spice (simulation program with integrated circuit emphasis),” tech. rep., Univeristy of California, Berkeley, 1973.
- [74] J. F. Dawson, “Conductance of 2-d fibre mesh,” tech. rep., University of York, 2015.
- [75] J. F. Dawson, A. N. Austin, I. D. Flintoft, and A. C. Marvin, “Shielding effectiveness and sheet conductance of nonwoven carbon-fibre sheets,” *IEEE Transactions on Electromagnetic Compatibility*, vol. PP, no.99, pp. 1–9, 2016.
- [76] I. Balberg and N. Binenbaum, “Computer study of the percolation threshold in a two-dimensional anisotropic system of conducting sticks,” *Physical Review B*, vol. 28:7, pp. 3799–3812, 1983.
- [77] J. F. Dawson, “Effect of thickness and anisotropy on percolation threshold,” tech. rep., Univeristy of York, 2015.

